Ultrashort pulse generation in 2-μm laser oscillators based on Tm-doped sesquioxides

Anna Suzuki

Department of Engineering Science

Graduate School of Informatics and Engineering

The University of Electro-Communications

Doctor of Engineering

March 2023

Ultrashort pulse generation in 2-μm laser oscillators based on Tm-doped sesquioxides

Anna Suzuki

APPROVED BY SUPERVISORY COMMITTEE:

CHAIRPERSON: Assoc. Prof. Masaki Tokurakawa

MEMBER: Prof. Hitoki Yoneda

MEMBER: Prof. Akira Shirakawa

MEMBER: Prof. Masayuki Katsuragawa

MEMBER: Prof. Shigeki Tokita

和文概要

Tm添加sesquioxideを用いた波長2 μm帯レーザーの超短パルス化

　　本論文は、広帯域な利得を実現する新規手法により波長2 μm帯Tmレーザーの超短パルス化を目指す研究に関するものである。Tmレーザーは高効率・高出力動作可能な波長2 μm帯コヒーレント光源として知られ、高出力半導体レーザー(LD)励起、そして通信帯で用いられるガラスファイバーの利用が可能であり、高出力化を目指した連続波(CW)やQスイッチレーザー等の研究が中心になされてきた。その後、光周波数コムや非線形波長変換の基本波としての応用が期待され、モード同期による超短パルス発振が注目され始めた。ファイバーレーザーでは2000年代から、そして2010年代からは固体バルク材料を用いたモード同期レーザーの研究が盛んになった。しかしTmは希土類イオンでありCrなどの遷移金属レーザーに比べ利得帯域幅が狭いため超短パルス発振はあまり得意としていない。さらにレーザー光源の歴史が古い近赤外域に比べ、波長2 μm帯では可飽和吸収体などモード同期技術が成熟しておらず、当初はps程度のパルス幅しか実現することができなかった。　そこで、より広帯域な利得を得るためのホスト材料の開発やモード同期技術の改良の研究が行われ、現在では100 fs以下の超短パルス発生が可能になった。

　　しかしながら、有限の利得幅の中で超短パルス化を試みる場合、低い透過率の取り出し鏡を用いて線形損失を小さくした共振器を構成することが多く、結果として短パルス性と高出力性を両立することは難しい。

　　本研究では、高出力性を兼ね備えた超短パルス発生のため、より広い利得帯域を得る2つの新規手法を提案した。1つは、複数の異なる利得材料を用いた複合利得媒質である。異なる利得媒質を同一共振器内で使用することで、両者の利得スペクトルを同時に利用することができる。本研究で用いた$Tm:Lu_2O_3$、$Tm:Sc_2O_3$は1950 nmと2070 nm、および1980 nmと2100 nm付近に利得のピークを持つため、これらのスペクトルを線形に結合することで実効的に広く平坦な形状の利得スペクトルを得ることができる。この2つの利得媒質を同時に用いて、CWおよびカーレンズモード同期レーザー発振実験を行った。CWの波長可変実験では、両媒質の利得帯域全体に及ぶ1962-2252 nmの波長可変幅が得られた。カーレンズモード同期実験では、透過率1%の出力鏡を用いて平均出力81 mWにおいて52 fsのパルス幅が得られた。そして、更なる短パルスを得るため、出力鏡を透過率0.5%のものに変更し、低損失の共振器を構築した。その結果、中心波長2094 nmにおいて半値幅100 nm以上の広帯域なモード同期スペクトルが得られ、Tm添加固体モード同期レーザーにおいて最短パルス幅となる41 fsを実現することができた。これは両媒質の利得帯域を同時に用いることで利得帯域が拡大されたことによって実現された。

　　利得帯域の拡大のためのもう一つの手法は、新規母料、混晶sesquioxideの開発である。混晶sesquioxideは、3種類の立方晶のsesquioxideの混合組成$(Lu_xSc_yY_z)_2O_3$（x+y+z=1）からなっ

ている。希土類を添加した混晶sesquioxideは、混合組成中の様々な結晶場強度に起因する不均一広がりにより、広帯域で平坦な形状の利得スペクトルを示すことから超短パルス発生に適している。さらに、従来のsesquioxideは2350°C以上の極めて高い融点を示すのに対し、混晶では融点が2150°Cを下回る組成が存在する。これにより、従来のチョクラルスキー(Cz)法による高品質な大型レーザー結晶の育成が可能となる。本研究では、イリジウムるつぼからCz法により新規Tm:YScO$_3$単結晶を育成し、結晶光学および分光特性を明らかにした。CWレーザー実験では1611 nmのEr:YbファイバーMOPA励起により透過率5%の出力鏡を用いて最大51%のスロープ効率を達成し、カーレンズモード同期実験では平均出力100 mWにおいてパルス幅58 fsのモード同期パルスが得られた。これらの結果より、混晶sesquioxideの超短パルスレーザーの利得媒質としての有用性が示された。

　以上より、複合利得媒質では利得帯域の線形結合により実効的な利得帯域幅を広げることに成功し、カーレンズモード同期によりこれまでのTm添加固体レーザーの最短パルス幅を大幅に更新した41 fsの最短パルス幅を実現した。混晶sesquioxideの開発では、Tm添加YScO$_3$結晶の育成及び分光・レーザー特性評価を行い広帯域かつ平坦な利得のプロファイルを確認した。双方の手法において従来の単一利得媒質の限界を超えた利得の広帯域化に成功し、高出力性と超短パルス性を兼ね備えたTmレーザーの実現に向け有効な手法であることを示した。

Abstract

This thesis describes ultrashort pulse generation from Tm-based 2 μm solid-state lasers using the novel gain media which exhibit broad gain bandwidth overcoming conventional limitations. Tm-doped materials are interesting gain media for highly efficient high-power 2 μm lasers due to the availability of high-power laser diodes (LD) as their pump source and so-called two-for-one pumping scheme which enables quantum efficiency close to 2. However, the relatively narrow gain bandwidth makes ultrashort pulse generation in the mode-locked Tm lasers challenging. In the last decade, aiming to further shorter pulse generation, a lot of research focusing on the development of novel host materials and the improvement of mode-locking techniques have been done and that enabled sub-100-fs pulse generation. However, due to the finite gain bandwidth, ultrashort pulse lasers tend to consist of low-loss cavities with lower transmittance output couplers, resulting in limited output powers.

In this study, two novel methods were proposed to realize broader gain bandwidth for the generation of high-power ultrashort pulses. The one is the combined gain media which is consisted of different gain materials. Using different gain media in the same cavity, the laser can benefit from the gain spectra of both materials. Kerr-lens mode-locked (KLM) laser experiments were performed using a $Tm:Lu_2O_3$ and a $Tm:Sc_2O_3$ simultaneously. Owing to broad effective gain bandwidth, the shortest pulse duration of 41 fs was achieved also supported by the intracavity nonlinear process. The other method is the development of mixed sesquioxide. Rare-earth doped mixed sesquioxides exhibit broad and smooth gain profiles owing to inhomogeneous spectral broadening caused by various crystal field strengths in the mixed crystal composition. That is suitable for broadband mode-locked lasers. Moreover, the reduction of melting temperature of mixed sesquioxide enables us to use the Czochralski(Cz) growth method for the fabrication of high-quality large-size crystals while it was impossible for the conventional non-mixed sesquioxides due to their extremely high melting temperatures. In this study, the novel mixed sesquioxide $Tm:YScO_3$ crystals were grown by the Cz-method using iridium crucibles for the first time. Spectroscopic investigations and laser experiments with the as-grown crystals revealed their suitability for ultrashort pulse generation in the mode-locked lasers.

TABLE OF CONTENTS

List of Figures

List of Tables

Abbreviations and acronyms

CR cross-relaxation

CW continuous wave

Cz Czochralski

ESA excited state absorption

ETU energy transfer upconversion

FL fiber laser

FWHM full width at half maximum

GD group delay

GDD group delay dispersion

GSA ground state absorption

GVD group velocity dispersion

HEM heat exchanger method

HHG high harmonic generation

HIP hot isostatic pressing

HOD high order dispersion

ICP-OES inductively coupled plasma optical emission spectrometry

Ir iridium

KLM Kerr-lens mode-locking

LD laser diode

LHPG laser heated pedestal growth

MIR mid-infrared

ML mode-locking

MOPA master-oscillator power amplifier

NIR near-infrared

OC output coupler

OPA optical parametric amplifier

OPO optical parametric oscillator

PLD pulsed laser deposition

Re rhenium

RF radio frequency

SA saturable absorber

SC super continuum

SESAM semiconductor saturable absorber mirror

SHG second harmonic generation

SPM self phase modulation

SPS spark plasma sintering

SRS stimulated Raman scattering

SSR solid state reaction

SWCNT single-walled carbon nanotube

SWIR short wavelength infrared

TOD third order dispersion

UV ultra violet

VGF vertical gradient freeze

XRD X-ray diffraction

YAG Yttrium Aluminium Garnet

Chapter 1

Introduction

Tm lasers are interesting light sources operating at 2 µm wavelength range. Tm ions can be pumped by commercially available high-power AlGaAs laser diode (LD), which can emit up to several hundreds watt at 0.8 µm. An ion excited at 0.8 µm can excite a neighboring Tm ion via cross relaxation process, which enables quantum efficiencies close to 2. This so-called "two-for-one" pumping scheme can realize the slope efficiency up to ∼80% while the Stokes efficiency is as low as ∼40% [1]. Therefore, Tm lasers are promising especially for high-power and highly efficient laser operation. In the CW laser regime, Tm-doped fiber laser (FL) with an average output power of 1 kW at a wavelength of 2050 nm with a slope efficiency of 53% was achieved under 793 nm fiber-coupled LDs pumping [2], which is actually the second highest average power among rare-earth doped FLs next to Yb-doped FL [3]. For solid-state laser, an output power of 245 W at a wavelength of 1990 nm with a slope efficiency of 46% was achieved by a Tm:YAP InnoSlab laser pumped by 795 nm four-bar LD stacks [4]. In the pulsed laser regime, due to the comparably long fluorescence lifetime of Tm-based gain materials, Q-switched lasers are successful. A peak power of 18.6 kW with a pulse duration of 41 ns and a pulse energy of 800 µJ at 2044 nm was demonstrated by Q-switched Tm-doped FL [5]. Moreover, a pulse energy of 128 mJ at 10 Hz repetition rate with a pulse duration of 160 ns was achieved from a 785 nm LD-pumped Tm:YAG Q-switched laser [6]. The power scalability of 2 µm Tm lasers is interesting for the nonlinear wavelength conversion. Freqency upconversion via high harmonic generation (HHG) is interesting to reach soft X-ray region to explore the dymanics of atoms and electrons. In this process, the cut-off frequency is proportional to the wavelength of the driver laser, thus the 2 µm lasers enable to reach higher energy region compared with the conventional near infrared lasers. On the contrary, the mid-infrared spectral region (4.0 - 20 µm)[1] is called molecular fingerprint region because there are a lot of molecular vibrational absorption lines. That enables ultrafast spectroscopy applications with high sensitivity, e.g., bioimaging [7, 8, 9], gas sensor [10, 11], breath analysis [12, 13] as well as polymer processing [14, 15]. Optical parametric oscillator (OPO) or optical parametric amplifier (OPA) is the common technique of frequency down-conversion. To reach the mid-infrared (4.0 - 20 µm), only non-oxide nonlinear materials such as GaAs, GaSe, $AgGaS_2$, and $ZnGeP_2$ are available since oxide materials are typically not transparent above 4 µm [16]. However, non-oxide materials exhibit an absorption edge around 1 µm due

---

[1]There are many opinions regarding wavelength range to define MIR and molecular fingerprint region.

---

to the small bandgap. Therefore, the near-infrared lasers (Ti:Al$_2$O$_3$, Nd, Yb lasers) are not suited for direct conversion to mid-infrared (MIR) owing to the one-/ two-photon absorption process in the nonlinear materials. Actually, conventional mid-infrared OPO/OPA has been basically achieved by multiple wavelength conversion schemes from near-infrared lasers [17, 18, 19]. While these are matured sources and commercially available, the configuration is complicated and overall conversion efficiency is strongly limited. However, 2 μm lasers enable direct conversion to mid-infrared [20]. The use of 2 μm lasers for the system can benefit for improving conversion efficiency, simplifying configuration, downsizing, and cost reduction.
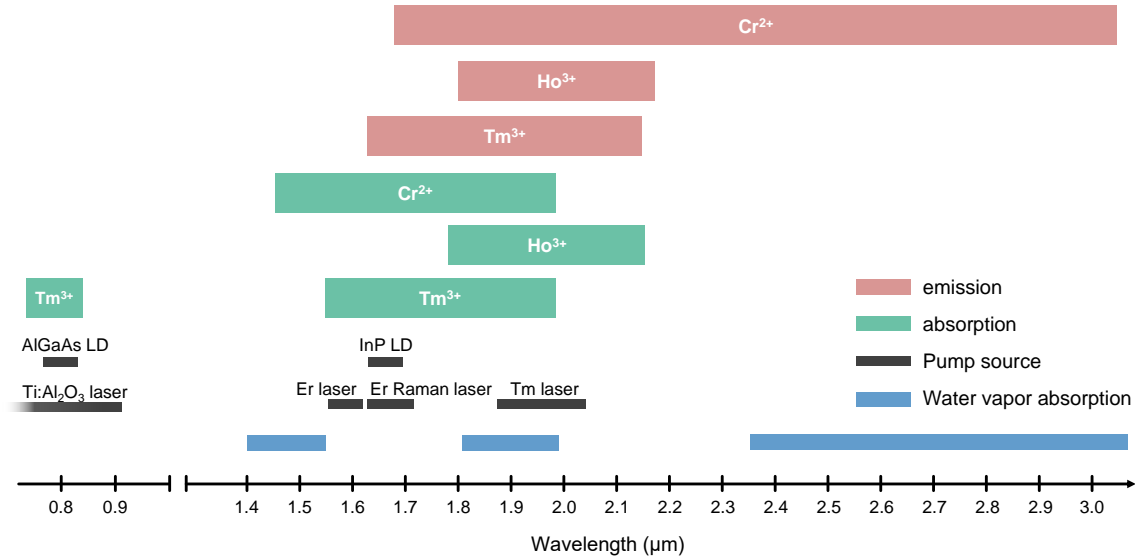
Figure 1.1: Absorption and emission band of 2 μm laser ions and their available pump sources.

Besides Tm lasers, Ho- and Cr-based lasers are also eligible candidates as the driving laser for nonlinear wavelength conversion. These lasers typically operate at roughly 2.1 and 2.4 μm, respectively. Figure 1.1 shows the typical gain band and pump band of the 2 μm lasers. Since above wavelength conversions are based on the nonlinear optical effect, high optical intensity is desirable for highly efficient conversion and higher yield. Thus, the ultrafast lasers with high peak power are desirable for this application and peak power scaling can be achieved by higher pulse energy and/or shorter pulse durations. Cr^{2+}-doped chalcogenide lasers have a huge advantage in terms of ultrashort pulse generation. This is due to their broad gain bandwidth thanks to the vibronic transition. In the Cr^{2+} lasers, sub-50-fs pulse generation is possible and the shortest pulse duration of 23 fs was recorded by KLM Cr:ZnS laser [21]. Cr^{2+} lasers are typically pumped by rare-earth doped solid-state lasers, i.g. Er, Tm, Ho fiber/bulk lasers. Despite these solid-state lasers being well-developed and commercially available, these are expensive compared with LDs, and Er, Tm, and Ho lasers tend to affect instabilities owing to unwanted transition between their complex energy levels, resulting in limited maximum output powers. Ho lasers are excellent, especially for high-power laser operation [22] owing to comparably high gain cross sections and long lifetime of upper laser level among rare-earth ions. However, Ho lasers are pumped by Tm lasers, Thus, it is restricted in terms

of available pump power and cost as same as Cr lasers. Moreover, Ho emission band is narrow and highly structured, consequently, available pulse duration mostly remains picosecond regime. The shortest pulse duration of 190 fs was achieved by dispersion managed mode-locked Ho laser [23], however, sub-100-fs pulse generation is considerably difficult. Compared with Cr^{2+} and Ho lasers, Tm lasers are advantageous owing to the availability of high-power LD pumping and highly efficient laser operation owing to *two-for-one* pumping scheme. Regarding the pulse duration, the relatively narrow gain bandwidth of Tm lasers makes sub-100-fs pulse generation challenging, although several hundred fs pulses have been routinely achieved.
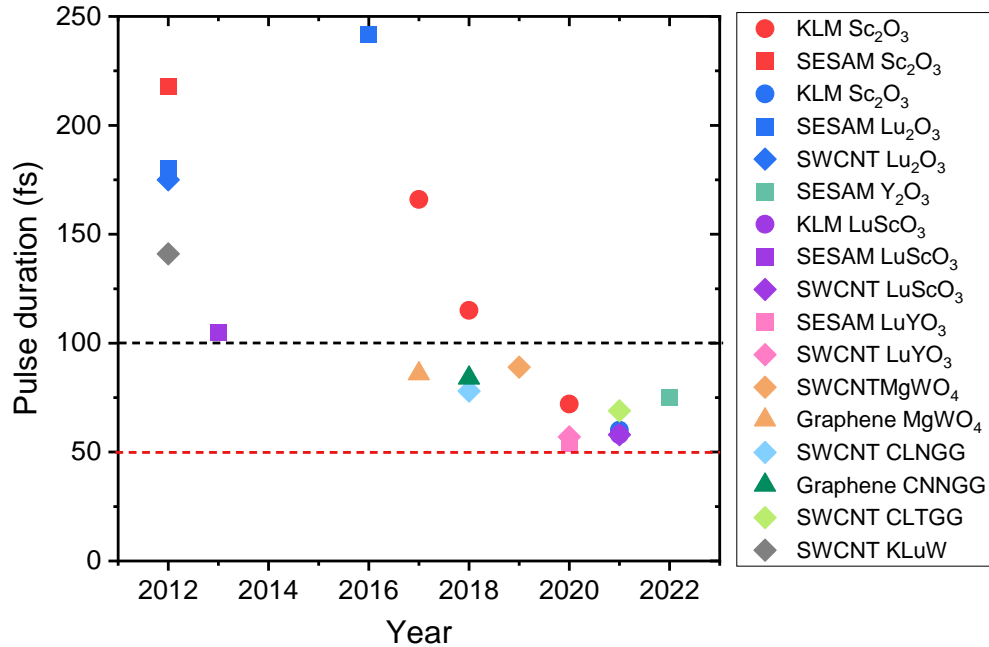
Figure 1.2: Ever reported pulse durations of mode-locked Tm-based solid-state lasers.

In the last decade, to overcome the limitation of pulse duration, a lot of efforts have been made for pulse shortening in Tm lasers. The main challenges are the development of novel laser host materials which show broad gain bandwidth. Figure 1.2 shows the evolution of pulse durations of Tm-based solid-state bulk lasers. The first sub-100-fs pulse generation was achieved by the Tm-doped $MgWO_4$ crystal laser based on the graphene mode-locking in 2017 [24]. Afterward, further shorter pulse durations were demonstrated successively using disordered host materials, e.g., multi-component garnet [25, 26, 27] and mixed sesquioxides [28, 29, 30, 31]. However, the shortest pulse duration still remains above 50 fs. In addition, most of the mode-locked lasers for sub-100-fs pulse durations adopt low-loss cavities at the expense of average output power to overcome the finite gain bandwidth. Those indicate the limitation of the gain bandwidth of the conventional Tm-doped crystalline materials.

Here, this study aims to generate high-power ultrashort pulses from Tm-based lasers using novel techniques to achieve broader gain bandwidth. This thesis proposes two different approaches. One is the combined gain media laser. The other is the development of novel disordered gain materials.

This thesis is organized as follows. Chapter 2 describes the basis of laser gain medium to understand the role of active ions and host materials. The origin of characteristics of laser materials and their fabrication techniques, especially for Tm-doped sesquioxides which are used in this study were described. Chapter 3 describes the basis of mode-locking. Fundamental theory, practical methods, and its limitations due to various instabilities are described. Chapter 4 dedicates the concept and experiments of combined gain media laser. Simulation of effective gain and experimental setup, properties of CW and ML laser operation are described. Chapter 5 devotes the growth, spectroscopy, and laser experiments of Tm-doped mixed sesquioxide crystals. Chapter 6 describes the conclusion and outlook. The comparison of combined gain media and mixed sesquioxide gain materials is detailed discussed in this chapter.

Chapter 2

Laser gain medium

Gain medium is an essential element for the lasers. Basically, it defines laser parameters, e.g., laser wavelength, amount of optical gain, available pulse duration, and so on. Thus, the proper choice of a gain medium is essential to achieve the desired specification.

This chapter gives the fundamentals regarding laser gain medium to understand the role of the active ions and host materials particularly focusing on Tm^{3+} and sesquioxides. Section 2.1 deals with the energy diagram of Tm^{3+} ion and important processes of ions in the host materials. Section 2.2 explains the role of host materials and characteristics of cubic sesquioxides, comparing with other host materials. Section 2.3 gives an introduction of fabrication methods for sesquioxides.
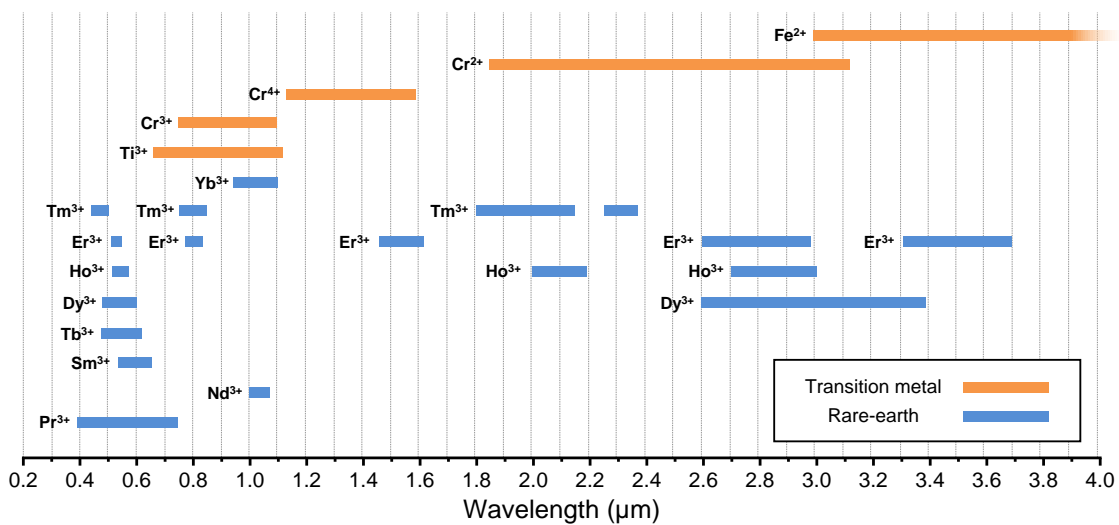
Figure 2.1: Operation wavelengths of typical solid-state lasers.

2.1 Dopant ion

2.1.1 Laser active ions

Transitions of electrons involving absorption and emission occur in between two different energy levels of dopant ions. The absorption/emission wavelength is determined by the energy gap between the two corresponding energy levels. These cross sections represent the transition probabilities of corresponding levels [32]. Figure 2.1 shows typical active ions of solid-state lasers and their operation wavelengths from visible to MIR spectral region [33, 34, 35, 36]. Laser ions are mainly divided into two groups, i.e. transition metal and rare-earth ions. The difference between them is the orbital which is utilized for laser transitions. Figures 2.2 and 2.3 show the electron configurations of transition metal and rare-earth ions. In transition metal ions, transitions will occur within the 3d orbital that is directly exposed to the surrounding environment, thus the electron is strongly affected by the crystal field (strong electron-ion coupling). On the contrary, in the trivalent rare-earth ions, transitions mainly take place within the 4f orbital which is shielded by the fulfilled 5s and 5d shells. Therefore, the 4f electrons of the rare-earth ions are less influenced by surrounded crystal field (weak electron-phonon coupling) than transition metal ions. This makes major differences in the optical spectra in terms of line width, structure, and cross sections between the two kinds of ions. While transition metals show broad spectra ($\Delta\lambda \sim$100s nm) and larger cross sections ($\sigma \sim 10^{-18}$-10^{-20} cm^{-1}), the rare earth ions exhibit narrow multiple peaks ($\Delta\lambda \sim$nm to 10s nm at full width at half maximum (FWHM)) and smaller cross sections($\sigma \sim 10^{-19}$-10^{-21} cm^{-1}).

Atom	Atomic number	1s	2s	2p	3s	3p	3d	4s	4p	4d	4f	5s	5p	5d	6s
Xe	54	2	2	6	2	6	10	2	6	10		2	6		
La	57				Xe core							Xe core		1 (0)	2 (0)
Ce	58				Xe core						1	Xe core		1 (0)	2 (0)
Pr	59				Xe core						3 (2)	Xe core			2 (0)
Nd	60				Xe core						4 (3)	Xe core			2 (0)
Pm	61				Xe core						5 (4)	Xe core			2 (0)
Sm	62				Xe core						6 (5)	Xe core			2 (0)
Eu	63				Xe core						7 (6)	Xe core			2 (0)
Gd	64				Xe core						7	Xe core		1 (0)	2 (0)
Tb	65				Xe core						9 (8)	Xe core			2 (0)
Dy	66				Xe core						10 (9)	Xe core			2 (0)
Ho	67				Xe core						11 (10)	Xe core			2 (0)
Er	68				Xe core						12 (11)	Xe core			2 (0)
Tm	69				Xe core						13 (12)	Xe core			2 (0)
Yb	70				Xe core						14 (13)	Xe core			2 (0)
Lu	71				Xe core						14	Xe core		1 (0)	2 (0)

Figure 2.2: Electron configurations of rare-earth atoms/ions. Red-colored numbers in brackets are for trivalent ions.

Atom	Atomic number	1s	2s	2p	3s	3p	3d	4s
Ar	18	2	2	6	2	6	10	
Ti	22			Ar core			2 (1, 2)	2 (0)
V	23			Ar core			3 (2, 3)	2 (0)
Cr	24			Ar core			5 (3, 4)	1 (0)
Mn	25			Ar core			5 (4, 5)	2 (0)
Fe	26			Ar core			6 (5, 6)	2 (0)
Co	27			Ar core			7 (6, 7)	2 (0)
Ni	28			Ar core			8 (7, 8)	2 (0)
Cu	29			Ar core			10 (8, 9)	1 (0)
Zn	30			Ar core			10 (9, 10)	2 (0)

Figure 2.3: Electron configurations of transition metal ions. Blue- and red-colored numbers in brackets are for trivalent and divalent ions, respectively.

2.1.2 Tm^{3+} ion

Thulium is the chemical element belonging to the lanthanide family with the atomic number of 69. It is the lowest abundance in Earth's crust among rare-earth (RE) ions (RE = lanthanide and Yttrium (Y) and Scandium (Sc)) [37]. The electron configuration is $[Xe]4f^{13}\ 6s^2$ where $[Xe]$ $=1s^2 2s^2 2p^6 3s^2 3p^6 3d^{10} 4s^2 4p^6 4d^{10} 5s^2 5p^6$. When Tm is doped in a host material, two 6s electrons and one 4f electron are lost to be a trivalent ion with the configuration of $[Xe]4f^{12}$. The energy level scheme of Tm in Y_2O_3 is shown in Fig. 2.4 [38, 39, 40].
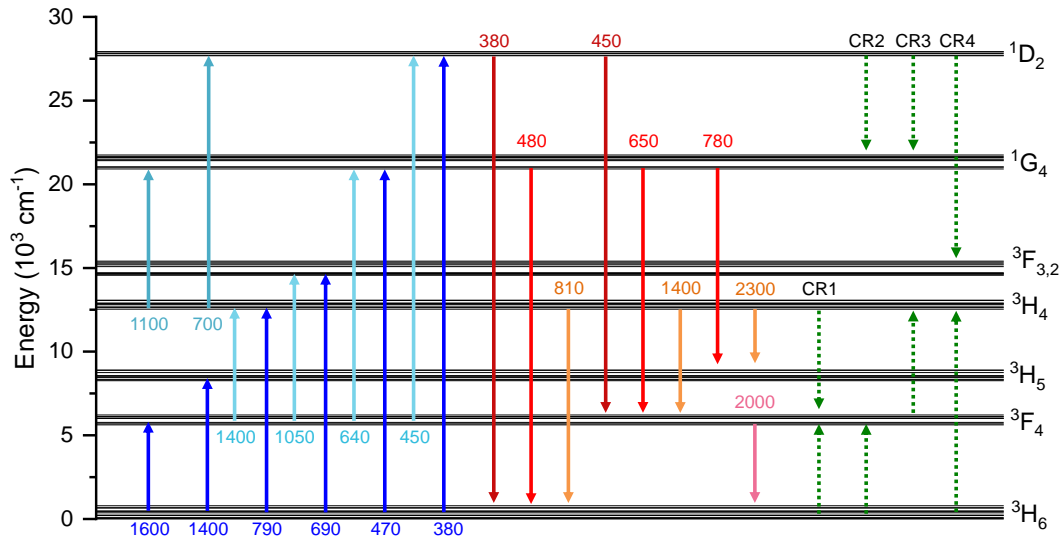
Figure 2.4: Energy diagram of Tm:Y_2O_3. (The unit is nm. CR: Cross relaxation.)

Tm ion has a lot of energy levels split by the spin-orbit interaction. 2 μm laser transitions involve the $^3F_4$ manifold to the $^3H_6$ ground state manifold. To obtain optical gain, we need to excite sufficient numbers of ions to the $^3F_4$ manifold. Practically, many interionic processes influence the population on the $^3F_4$ manifold; consequently, they affect laser performance and/or spectroscopic measurements. Figure 2.5 shows the important interionic processes including radiative and non-radiative processes as follows:

Reabsorption an emitted photon by an ion is absorbed by another ion on the ground state manifold. This process can be crucial, particularly for (quasi-) three-level laser systems such as Tm and Yb lasers because their absorption and emission bands are partly overlapping. It also causes experimental artifacts in fluorescence spectroscopy (detailed in Chapter 5.3).

Energy migration the whole exciting energy of an ion is resonantly transferred to another ion. This non-radiative process basically does not degrade the laser performance, as long as energy is transferred to the same active ions. However, it can be losses if impurities become the acceptors.

Energy transfer upconversion (ETU) ETU takes place between two ions in the excited states. An ion transfers excitation energy to another ion. If the final state of the acceptor ion is energetically higher than the initial state of the donor, it is referred to as energy transfer upconversion. In the Tm ions, this process will occur between ions in the upper laser level $^3F_4$, depending on the average distance of excited ions, i.e. lattice constant, doping concentration, and excitation density. It leads to the depopulation of the upper laser level, i.e. quenching, thus quantum efficiency will decrease.

Cross-relaxation (CR) CR is the inverse process to energy transfer upconversion. The difference in the definition is the final state of the acceptor ion, which is lower than the initial state of the donor ion. For the Tm ions, there are several combinations of energy levels with the same order of separation in Tm^{3+}, thus there are a lot of upconversion and cross relaxation transitions.
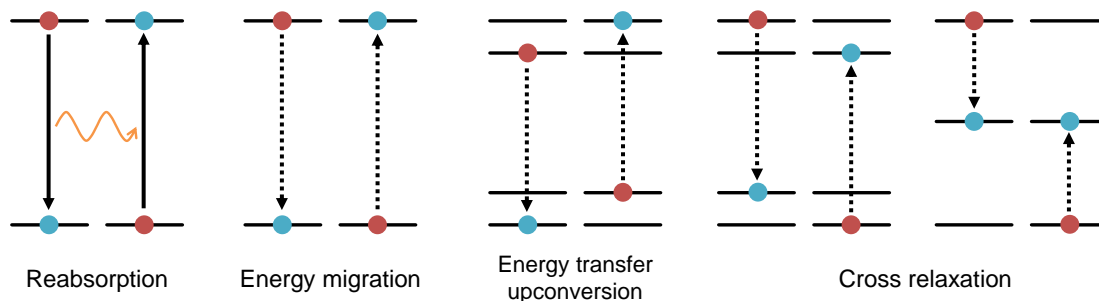
Figure 2.5: Interionic process in Tm^{3+} ions.
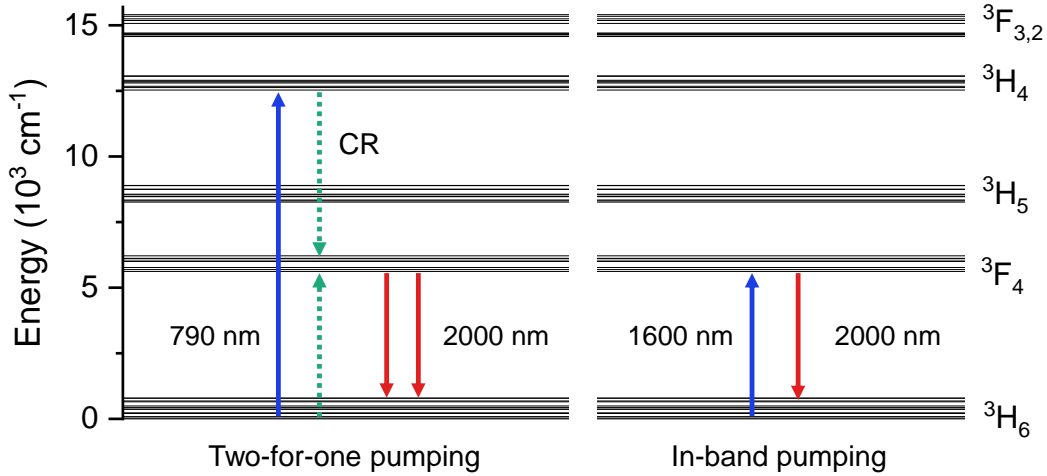
Figure 2.6: Pumping scheme of Tm^{3+}.

To excite Tm ions to the upper laser level, two pumping schemes are available. The pumping schemes are shown in Fig. 2.6. One is *two-for-one* pumping using the cross relaxation $^3H_4 \rightarrow {}^3F_4$ / $^3H_6 \rightarrow {}^3F_4$, which enables effcient population to the $^3F_4$ manifold. Once an ion is excited to the $^3H_4$, sufficiently close distance between Tm ions enables to achieve two excited ions by only one excited photon, which leads to quantum efficiency close to two overcoming conventional limitation at sufficiently high doping levels. Moreover, the energy gap between $^3H_6$ and $^3H_4$ is ≈ 12600 cm^{-1}, corresponding to 0.8 μm, where commercial available high power AlGaAs LDs are suitable. These are cheap and compact, and can emit up to several hundred watts with multimode-fiber coupled modules. In addition, well-developed Ti:Al$_2$O$_3$ lasers are also available. Their excellent beam quality eases Kerr-lens mode-locked lasers. The disadvantage of this pumping scheme is relatively large quantum defect. Although two-for-one pumping scheme is available under 0.8 μm pumping, the efficiency of cross relaxation does not reach 100% in most cases. Ions which not contribute to cross relaxation will lead to multi-phonon relaxation and there are several channels of phonon decay, resulting in high thermal load. Especially for high-power laser operation under 0.8 μm LDs pumping, special treatment for cooling of gain materials is required, e.g. gain fiber is cooled by immersing in a water-filled basin [41].

Another scheme is in-band pumping, corresponding to the transition $^3H_6 \rightarrow {}^3F_4$, which wavelength is around 1.6 μm. In this pumping scheme, the quantum efficiency never exceeds unity. However, the absorption cross section is generally higher than that of the 0.8 μm absorption band, resulting in higher absorption efficiency. In addition, the quantum defect is smaller than "two-for-one" pumping. Compared with "two-for-one" pumping, in-band pumping does not need high doping concentration. Therefore, in-band pumping with lower doping gain material could achieve highly efficient laser operation by mitigating the quenching effect at a higher inversion level. For 1.6 μm wavelength range, longer wavelength Er fiber lasers [42] and Raman-shifted Er fiber lasers [43, 44] are available. In recent years, InP-based LDs became available owing to their improved output powers up to several watts.

2.2 Host material

2.2.1 Role of host material

One of the important roles of the host material is to resolve a degeneracy of the Stark levels of a dopant ion by the crystal field. Figure 2.7 shows the schematic of the energy level distribution of Tm [45, 46]. When the ions enter a solid, owing to the electrostatic field of the ligands, the degenerated energy levels of the dopant ion split, resulting in broad absorption/emission spectra. This effect is called *Stark effect* or *Stark splitting*. For ions with an even number of electrons, the manifold splits into (2J+1) sublevels, while for ions with an odd number of electrons a 2-fold degeneracy remains according to the Kramers theorem, thus the manifold splits into (2J+1)/2 sublevels. Here, J is the total angular momentum quantum number. Since 4f electrons are shielded by the outer fulfilled orbital, the Stark effect is about one order of magnitude smaller than the spin-orbit interaction. Different host materials variously modify the spectroscopic properties of dopant ions, e.g. cross sections, spectral bandwidth, radiative/fluorescence lifetime, anisotropy, and so on.
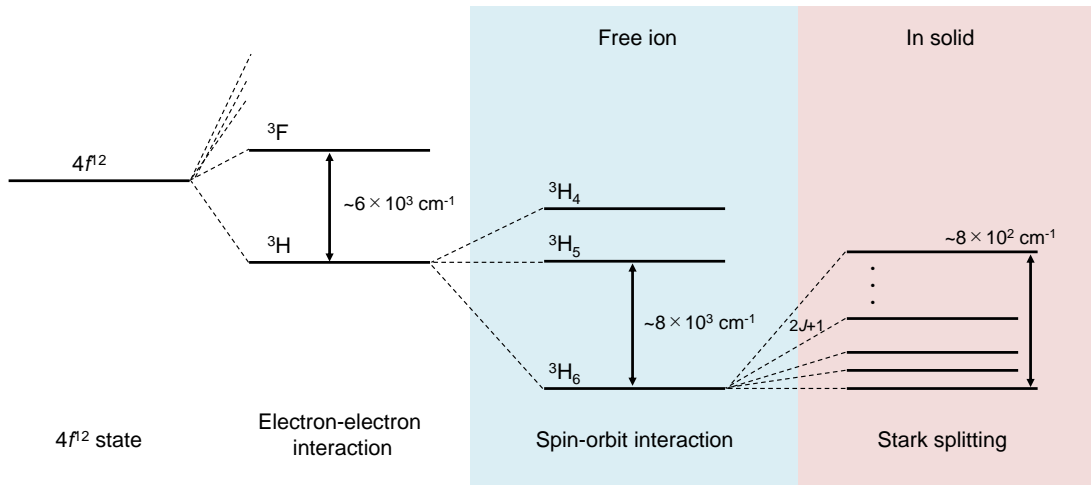
Figure 2.7: Schematic of representation of energy diagram and splitting in solid.

The important parameters of the host materials other than the interaction with the dopant ions are thermo-mechanical and thermo-optic properties. These parameters dominate the laser performance particularly at higher output power levels. Thermal conductivity determines the cooling efficiency of the materials. Thermal expansion coefficient influences the mechanical stability of the gain material. Thermo-optic coefficient, denoted by dn/dT, signifies the impact of temperature on the refractive index. When the gain material is heated up by gaussian shaped beam, the temperature profile will change following the beam profile, thus the refractive index will also change. As a result, the changed refractive index will form a lens, which is called *thermal lensing*. It influences beam propagation, which leads to unstable cavity conditions and degradation of laser performance. Therefore, efficient laser operation even at high output power levels requires efficient cooling of the gain material as well as the choice of host materials that have high thermal conductivity, small thermal expansion coefficient, and small thermo-optic coefficient.

For high-intensity light, host materials exhibit nonlinear effects. One of the third-order nonlinear effects is the optical Kerr effect. It enables mode-locking, i.e., Kerr-lens mode-locking, which is detailed in Chapter 3.3. Owing to the lattice vibration, the host material can act as Raman gain media. High intense lasers undergo stimulated Raman scattering (SRS), originating from the interaction of laser photons with lattice phonons, and laser photons are spectrally red-shifted, which is one of the main limitations for power scaling of fiber lasers [47]. On the other hand, it could be useful for wavelength conversion, i.e., self-Raman lasers [48, 49]. Besides, using other nonlinear effects, 2-, 3-, 4-th harmonic generation and super continuum (SC) generation by the random quasi-phase matching in the polycrystalline media are also observed [50].

2.2.2 Cubic sesquioxide

Crystallographic properties

Laser host materials are classified into single crystalline, polycrystalline (ceramics), and glass. For cubic sesquioxides, single crystalline and polycrystalline are available, thus this section deals with crystalline materials. Cubic sesquioxides, Lu_2O_3, Sc_2O_3, and Y_2O_3 possess cubic C-type structure (bixbyite structure), which belong to the rare-earth sesquioxide family. Their lattice constants are around 10 Å and the cation densities are around 3×10^{22} cm^3, which is higher than that of other common laser crystals, e.g., twice as high as that of Yttrium Aluminium Garnet (YAG) [51]. Therefore, rare-earth ion doped sesquioxides show conspicuous interionic processes described above with comparably low doping levels because of the closer average distance between doped ions. Figure 2.8 shows the unit cell and two crystal sites of the cubic sesquioxides. The unit cell is composed of 16 formula units, thus contains 32 cations. 24 cation sites have C_2 symmetry and the rest 8 have C_{3i} symmetry. As the C_{3i} symmetry shows inversion symmetry, electric dipole transitions remain forbidden. Therefore, the optical transitions of doped ions on this site are significantly weaker than that on the sites with C_2 symmetry. In other words, spectroscopic characteristics are mainly determined by the dopant ions on C_2 symmetry sites.
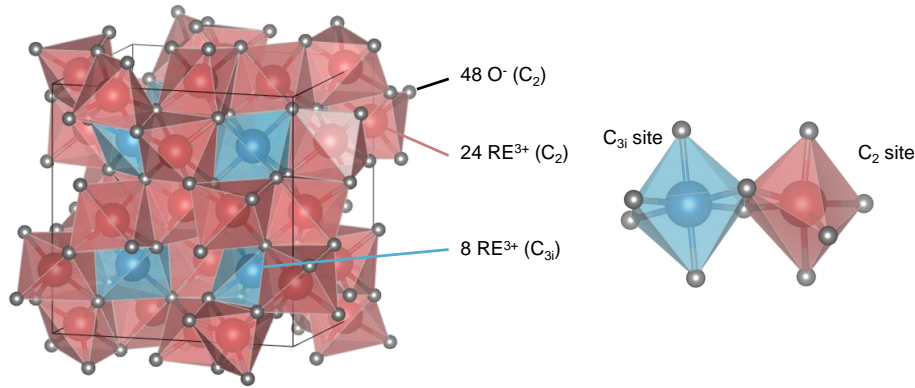
Figure 2.8: Schematic of the bixbyite structure of the cubic sesquioxides. The left is the unit cell and the right is C_2 and C_{3i} symmetry sites.

Optical properties

Cubic sesquioxides exhibit a transparency range from $\sim$220 nm in the UV to $\sim$8 μm in the mid-infrared. The Sellmeier equations to determine the refractive index for different wavelengths have been reported as follows, where the unit of λ is μm [46]:

$$\text{Lu}_2\text{O}_3 : \text{n}(\lambda) = (3.62004 + \frac{0.0412526}{\lambda^2 - 0.0239454} - 0.0086344 \cdot \lambda^2)^{1/2}, \tag{2.1}$$

$$\text{Sc}_2\text{O}_3 : \text{n}(\lambda) = (3.83252 + \frac{0.0492688}{\lambda^2 - 0.0237987} - 0.014094 \cdot \lambda^2)^{1/2}, \tag{2.2}$$

$$\text{Y}_2\text{O}_3 : \text{n}(\lambda) = (3.5387 + \frac{0.0421725}{\lambda^2 - 0.0243226} - 0.00914896 \cdot \lambda^2)^{1/2}. \tag{2.3}$$

The temperature-dependent Sellmeier equations are also proposed in Ref. [52]. Figure 2.9 shows refractive indices of cubic sesquioxides at room temperature calculated using the Sellmeier equation (2.1, 2.2, 2.3). The refractive indices at 2 μm are 1.9, 1.95, 1.87 for Lu_2O_3, Sc_2O_3, and Y_2O_3, respectively.
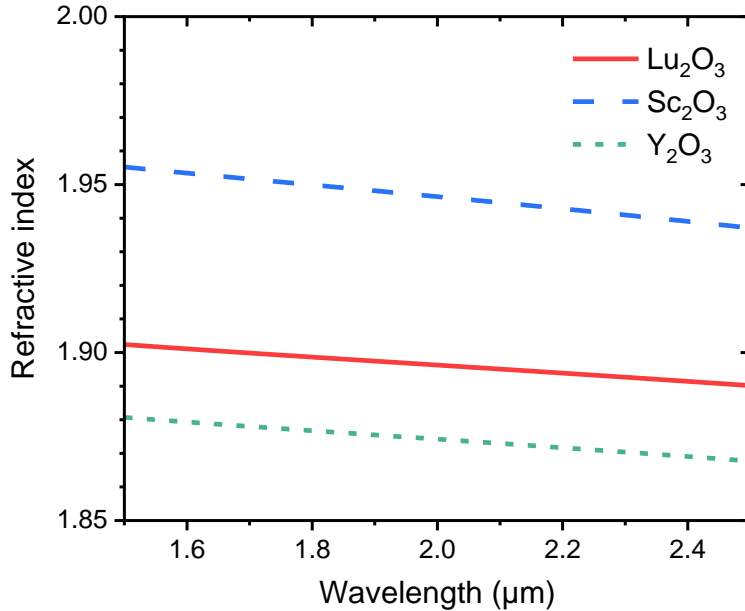
Figure 2.9: Refractive indices of cubic sesquioxides from 1.5 to 2.5 μm wavelength range.

The nonlinear refractive index, responsible for the Kerr-lensing and self-phase modulation (the time-dependent phase shift caused by the optical Kerr-effect), is a key parameter for mode-locked laser operations, which is described in Chapter 3. The nonlinear refractive indices can be measured using the induced birefringence [53], the critical power of self-focusing [54], the nearly degenerate three-wave mixing [55], and the Z-scan method [56]. The reports of the nonlinear refractive indices of cubic sesquioxide are summarized in Table 2.1.

Material dispersion is one of the origins of phase shift and deformation of an optical pulse shape. Optical pulses generated by mode-locking are formed by the coherent superpositions of numerous

Table 2.1: Nonlinear refractive indices of cubic sesquioxides

sample	n_2 10^{-16} cm^2/W	ref.
Lu$_2$O$_3$ ceramic	8.5 @ 0.5 μm	[57]
	3.3 @ 2.0 μm	[58]
Sc$_2$O$_3$ ceramic	11.1 @ 0.5 μm	[57]
Y$_2$O$_3$ ceramic	12.6 @ 0.5 μm	[57]
Y$_2$O$_3$ crystal	11.6 @ 1.0 μm	[55]
(Lu$_{2/3}$Sc$_{1/3}$)$_2$O$_3$ ceramic	4.66 @ 2.0 μm	[44]

frequency modes (longitudinal modes), and waves of different frequency modes propagate at a different speed owing to the material dispersion. Group delay (GD) is the time delay experienced by the whole optical pulse, thus the carrier frequency and pulse shape do not change with propagation. group velocity dispersion (GVD) is the wavelength dependence of the group velocity and the total amount of GVD for the propagation length is called GDD. Higher order effect of dispersion is called high order dispersion (HOD). Material dispersion can be calculated from the refractive index $n(\lambda)$ and GVD and third order dispersion (TOD) are described as follows:

$$GD = \frac{1}{c}[n_0 + \omega\frac{dn(\omega)}{d\omega}] = \frac{1}{v_g} = \frac{n(\omega)}{c}, \tag{2.4}$$

$$GVD = \frac{d(GV)}{d\lambda} = \frac{\lambda^3}{2\pi c^2}\frac{d^2n(\lambda)}{d\lambda^2}, \tag{2.5}$$

$$TOD = \frac{d(GVD)}{d\lambda} = -\frac{\lambda^2}{4\pi^2c^3}[3\lambda^2\frac{d^2n(\lambda)}{d\lambda^2} + \lambda^3\frac{d^3n(\lambda)}{d\lambda^3}]. \tag{2.6}$$

Figure 2.10 shows the material dispersion of cubic sesquioxides calculated using Eqs. (2.1)-(2.6). GVD and TOD at 2 μm are -7, -36, and -10 fs^2/mm and 275, 413, and 292 fs^3/mm for Lu$_2$O$_3$, Sc$_2$O$_3$ and Y$_2$O$_3$, respectively.
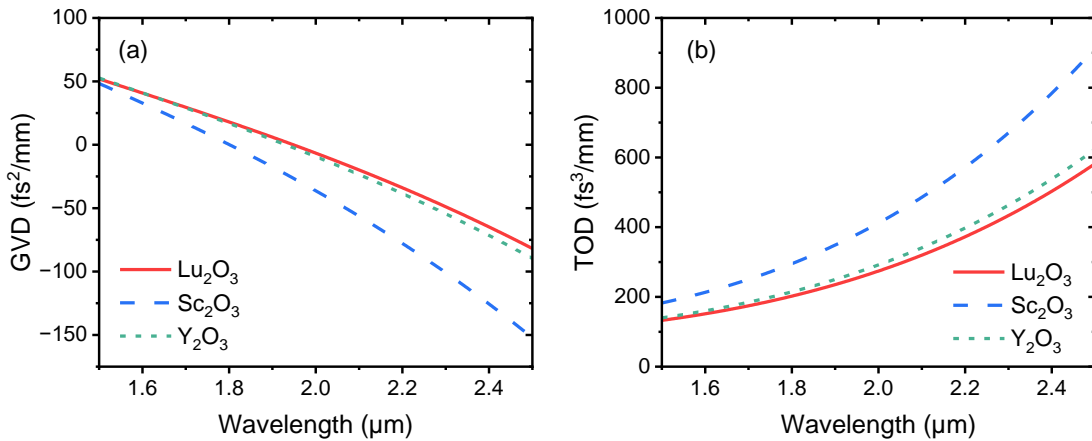
Figure 2.10: (a) GVD and (b) TOD of cubic sesquioxides.

Thermal properties

Sesquioxides are well-known for their high thermal conductivities. Thermal conductivity indicates the ability of heat transfer, thus host materials with high thermal conductivities enable faster heat ejection resulting in higher cooling efficiency. That is crucial especially for high-power laser operation. Thermal conductivities are mainly limited by the phonon scattering via umklapp process and at point defects [59]. The former is caused by phonon collision which is depending on the excited phonon numbers at high temperatures (above the Debye temperature); thus, thermal conductivity is inversely proportional to temperature. The latter is the phonon scattering due to the crystal's imperfections such as grain boundary, point defect, dislocations, and impurities including laser active ions. Therefore, the thermal conductivity of the laser material changes depending on the doping concentration of the active ion as well as the quality of the crystal. Thermal conductivity of non-doped Lu_2O_3, Sc_2O_3, and Y_2O_3 are reported to be 12.8, 18, 13.4 W/m·K, respectively [51]. These are compatible with the value of YAG (14 W/m·K) [60]. However, the thermal conductivity reduces with doping ion concentration as mentioned above, which is caused by the difference of ionic radii and mass between donor and acceptor ions. Actually, active ions doped sesquioxides exhibit higher thermal conductivity than that of YAG. In addition, in this respect, Lu_2O_3 is promising material because the difference of mass of Tm^{3+} and Lu^{3+} are quite small resulting in a small reduction of thermal conductivity with increased doping concentration [61]. On the other hand, the mixed sesquioxides, which is composed of a mixture of pure sesquioxides $(Lu_xSc_yY_z)_2O_3$ $(x + y + z = 1)$, exhibit significantly reduced thermal conductivity due to the disordered crystal structure led to increased phonon scattering. The values of non-doped materials were reported 1/2 to 1/3 of that of non-mixed sesquioxides, but do not significantly drop with doping ion concentration [62, 63]. These values are even higher than that of other host materials such as glasses [64] and double-tungstates [65].

The thermo-optic coefficient is often referred to as *thermal lensing coefficient*. When the material is heated by the gaussian shape beam, the refractive index profile will follow the beam profile. This results in the formation of the positive thermal lens if $dn/dT > 0$. The thermal lens directly affects the beam profile of the laser and induces instability on the cavity stable condition and/or worth mode-matching between the pump and laser beam. The heat shock parameter is the fracture limit in power scaling of the solid-state lasers [66].

Consequently, the suppression of the thermally induced effects is crucial for high-power laser operation, thus, host materials with higher thermal conductivity are desirable. Table 2.2 shows the crystallographic, spectroscopic, and thermo-mechanical properties of the cubic sesquioxides.

2.3   Fabrication of sesquioxide

Although the sesquioxides are promising candidates as a laser host material, crystal growth of the sesquioxides is challenging owing to their high melting temperatures of more than 2350°C. Their huge potential for laser applications was already proposed in the 1990s, however, laser-quality crystal growth became possible in the only last decade. Sesquioxide crystals are mainly grown from a melt, thus special treatments or devices are required to perform crystal growth at high temperatures.

On the other hand, the sesquioxides ceramics can be fabricated at sintering temperature $\approx 1700°$C which is significantly lower than the melting temperature. However, they have a particular problem to exclude the scattering centers for the fabrication of high-quality ceramics. In this section, the fabrication techniques for sesquioxides and these advantages/disadvantages are described below [67, 61, 62].

2.3.1 Single crystal growth

Crucible-free crystal growth methods

The main problem of the growth of high-melting-temperature crystals is the lack of choice of crucible material. Iridium, which is the most common material for the growth of high-melting-temperature oxide crystals, is not suitable for the growth temperature of sesquioxides. Therefore, crucible-free growth techniques have been developed.

The Verneuil method is the earliest melt technique, also known as the flame-fusion technique. Crystal growth is performed with finely powdered raw material and H_2/O_2 flame. The raw material is continuously supplied into the H_2/O_2 flame and it melts into fine droplets, which fall onto a seed crystal. This technique enables the growth of high-melting-point crystals with cm^3-scale in a short time. However, as-grown crystals tend to exhibit inclusions and strong internal stress due to the high thermal gradients during growth ($\sim$400 K/cm to $\sim$800 K/cm). Despite the sesquioxide crystals growth by the Verneuil method having been demonstrated in 1958 [68], their size and optical quality were strongly limited.

The floating zone technique is performed using a sintered rod of starting material. A small region of the rod is molten and recrystallized. During growth, the molten zone moves along the rod and crystallized as it cooled down. As a heating source, electron beams, halogen lamps, arc plasmas, gas burners, or lasers are utilized. Particularly, the laser-based technique is so-called laser heated pedestal growth (LHPG). This technique is suitable for high-purity crystal growth by using a crystalline rod instead of a sintering rod, and the crystal growth is relatively fast. The quality of crystals grown by the LHPG method is sufficient for spectroscopy [69, 70, 71], but insufficient for lasers because of strong stress induced by large thermal gradient during growth, resulting in cracking of the crystal. In addition, the dimension is also limited.

The pulsed laser deposition (PLD) is a technique to fabricate thin films. A high-power pulsed laser is focused on the surface of a solid target inside a vacuum chamber and the vaporized materials form a thin film up to a few μm thick on a substrate. It can be utilized for sesquioxide crystal growth [72], however, the dimension is strongly limited, thus it cannot be used for lasers.

In conclusion, crystals grown by crucible-free techniques are strongly limited in terms of dimensions, purity, and/or quality. Therefore, these methods are sufficient to grow crystals for spectroscopic measurements, however, it is basically impossible to grow laser-quality crystals using crucible-free methods.

Crucible-based crystal growth method

The most established growth technique to obtain high-quality cm^3-scale laser crystals is crucible-based method. For sesquioxide crystal growth, rhenium (Re) is the only crucible material. Re

sustains the high growth temperatures ($\sim$2400°C) and is chemically inert to the melt at the required growth atmospheres.

So far, cm^3-scale laser quality sesquioxide crystal growth was succeeded only by the heat exchanger method (HEM) from Re crucibles [73, 74, 75, 76].
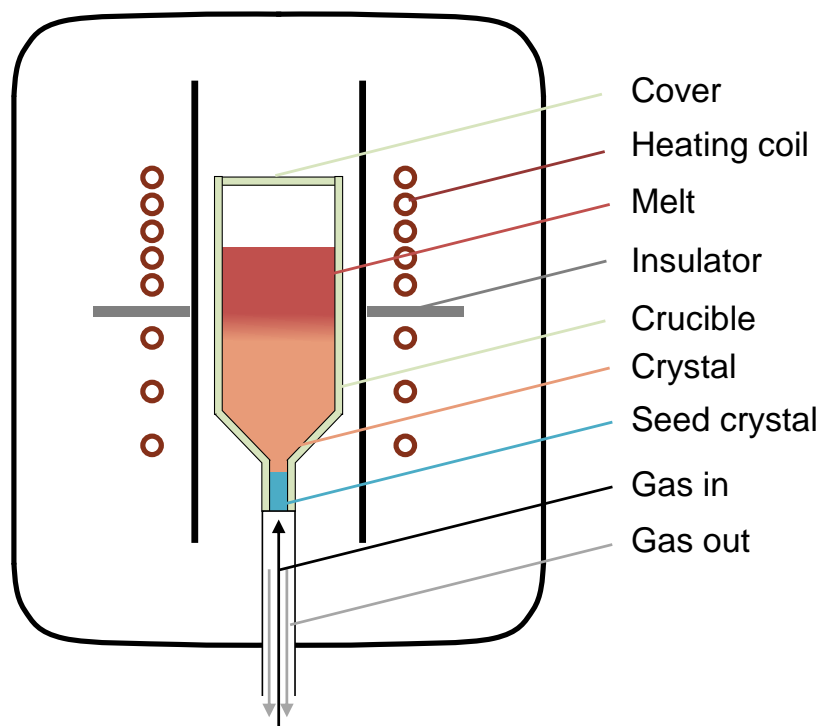
Figure 2.11: Typical setup for the HEM growth.

HEM is a variation of the Bridgman method. In the basic Bridgman method, the crucible is filled with raw materials and heated up to melt the materials. Subsequently, the crucible is moved from a hot zone to a cold zone, and the melt in the crucible is cooled down and directionally crystallized from one side where the seed crystal may be placed. There are two geometry types: vertical Bridgman and horizontal Bridgman. In this method, crystallization is occur inside the crucible, thus crystals suffer from stress from the walls. If there is a big difference of the thermal expansion coefficient between crystal and crucible material, crystals tend to strain strongly. HEM is a development of the vertical gradient freeze (VGF) method. VGF method is also a modification of the conventional Bridgman without moving the crucible. Crystallization is performed by changing the heat supply in the electromagnetic gradient multi-zone furnace, which enables to reduce internal stress. The HEM growth setup is shown in Fig. 2.11. In this method, the temperature gradient is mainly made by actively cooling the bottom of the crucible using gas flow. In this method, it is possible to delay the contact between the crystal and the wall of the crucible by maintaining constant heating of the crucible. That enables less stress crystals compared with the basic Bridgman method. Consequently, laser-quality Tm:Lu$_2$O$_3$, Tm:Sc$_2$O$_3$, and Tm:LuScO$_3$ crystals have been successfully grown by HEM from Re crucibles [73, 74, 75, 76]. However, the fabrication of Re crucible is troublesome and thus they are expensive. In addition, their sensitivity to oxygen in the growth atmosphere [74] makes

high-quality crystal growth difficult.

The Czochralski (Cz) method is also crucible-based growth technique. This is the most commonly used technique for the growth of the high-quality semiconductor and oxide crystals [77]. Figure 2.12 shows the typical growth setup of the Cz method. In this method, the raw materials are filled in the crucible. The pulling rod, commonly with a seed crystal at the tip, is dipped to the surface of the melt. Crystallization starts by the difference of temperature between the melt and the rod, subsequently, the growing crystal is slowly pulled out from the melt under rotation. In this method, the diameter of the crystal boule can be controlled by the melt temperature and the pulling and rotation speed. However, at the same time, growth instability such as a spiral can occur, under inappropriate growth parameters. Well-investigated growth parameters and matured technique are necessary to obtain high-quality crystals.

- Seed holder
- Seed crystal
- Crystal boule
- Heating coil
- Insulator
- Crucible
- Insulating ceramics
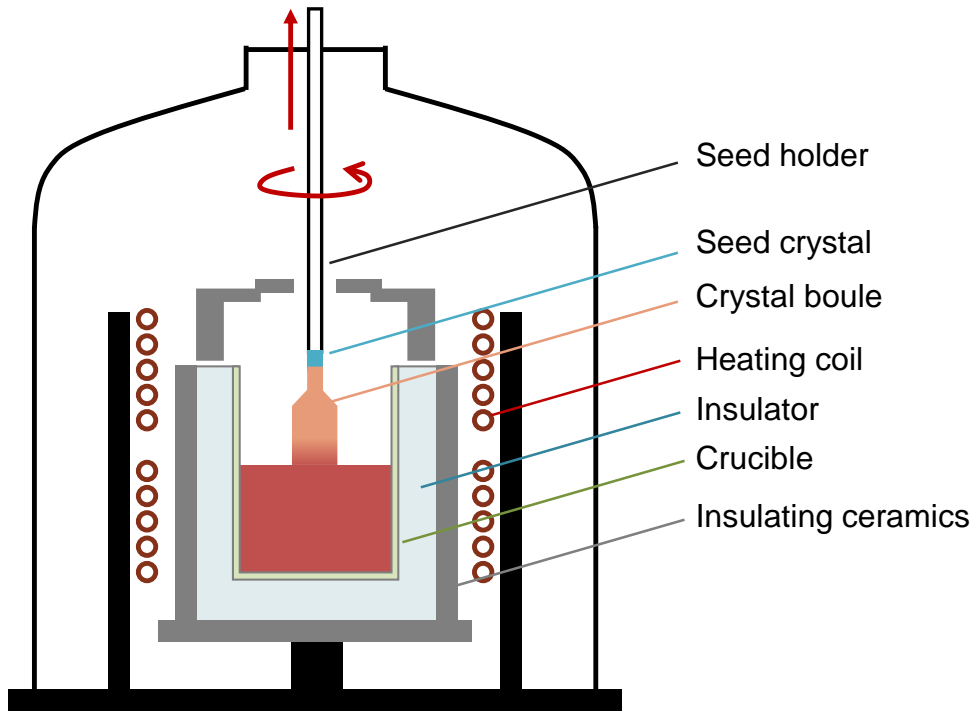
Figure 2.12: Typical setup for the Cz growth.

Mix and Fornasiero had been investigated the Cz growth of pure sesquioxide (Lu_2O_3, Y_2O_3, and Sc_2O_3) [78, 79], however, they obtained only ∼mm-long small crystals. At extremely high growth temperatures, the average photon energy of the emitted heat radiation is increased. At the same time the band gap energy of the growing crystal is reduced due to the increased atomic vibration [80]. Therefore, the growing crystals partially absorb the thermal radiation, but heat transportation is hindered due to reduced thermal conductivity at high temperatures. Consequently, significant growth instabilities occur. This strongly limits the size and quality of crystals. However, in very recent years, the phase diagram of the mixed sesquioxide was reinvestigated and the significantly reduced melting temperatures below 2150°C were found at certain compositions [62]. This melting temperature is acceptable for the Cz growth from conventional iridium crucibles. The details

regarding the Cz-growth of mixed sesquioxide is described in Chapter 5.2.

As another crucible-based method, flux growth is available. This is only available if the raw materials can be solved in a suitable flux. The suitable flux enables to reduce melting temperature, thus it has been investigated in the past years [81, 82]. Crystallization occurs as the solution cools down. Owing to the low growth temperature and low growth speed, a significantly small thermal strain is introduced into the crystal. However, the yield is quite small ($\approx$ mm^3-scale) despite the long growth time of several weeks to months. In addition, the as-crystals tend to exhibit inclusions of the solution, limiting the quality of the crystal.

2.3.2 Fabrication of laser ceramics

Laser ceramics have been developed as host materials alternative to single crystals and glasses. As the development of lasers toward higher average power levels and highly efficient operations, laser ceramics demanded better thermo-mechanical properties, higher optical homogeneity, larger size as well as the opportunity for composite configurations. They can be fabricated at a sintering temperature that is significantly lower than the melting point. That can be a huge advantage especially for high-melting-point materials such as sesquioxides. The general fabrication procedures of laser ceramics are shown in Fig. 2.13 [83, 84].
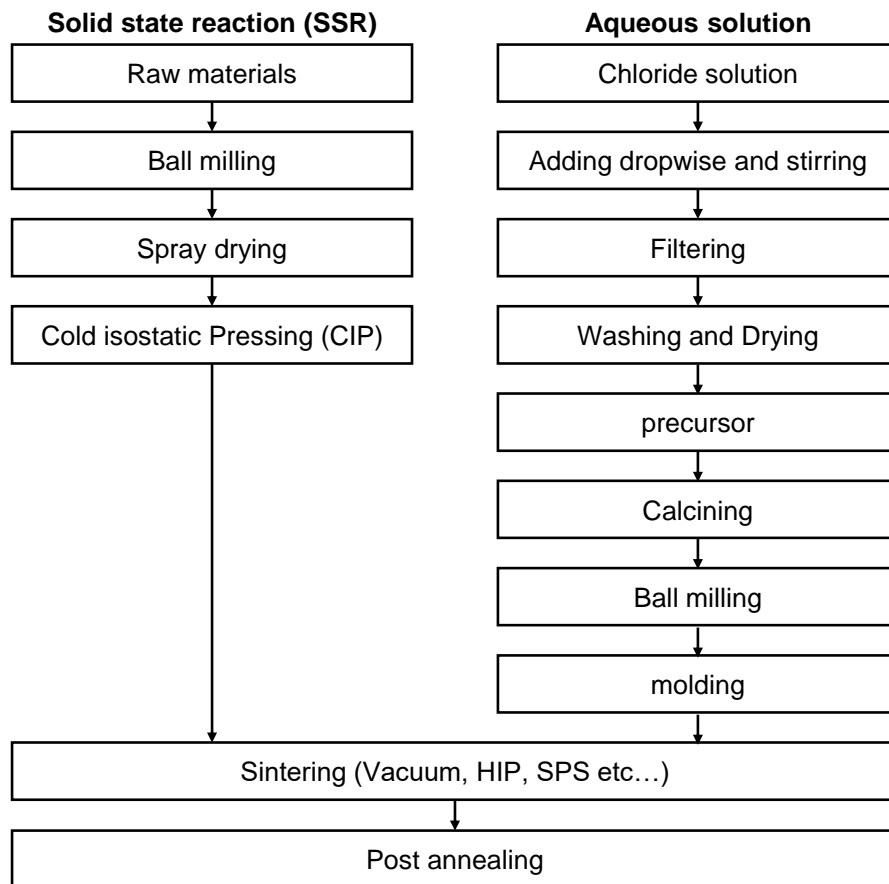
Figure 2.13: Ceramics fabrication procedure.

There are two kinds of powder preparation methods to be applied before sintering. The powder preparation process influences the grain size in ceramics. In general, solid state reaction (SSR) leads to larger grain size 20∼50 μm, while aqueous solution enables ∼μm size grain, as well as a highly homogeneous mixture and uniform size [85]. There are several sintering methods and their minor modifications, e.g., vacuum sintering [86, 87, 88], hot isostatic pressing (HIP) sintering [89, 90] and spark plasma sintering (SPS) [91, 92] have been applied for sesquioxide ceramic fabrication. Sintering promotes the growth of each single crystal by diffusion at grain boundaries, resulting in dense polycrystals. A challenge in ceramics fabrication is to achieve high transparency. Due to their polycrystalline nature, ceramics shows light scattering as shown in Fig. 2.14.

Scattering centers in ceramics are attributed to refractive index changes by (1) pores or impurities, (2) grain boundary, (3) secondary phase introduced by sintering aids such as ZrO_2, LiF, and La_2O_3 [93, 94], and (4) surface scattering by roughness. Since the generation of scattering centers strongly depends on the fabrication process, the proper choice of a preparation/sintering method with well-optimized parameters is necessary. In addition, anisotropic materials show large scattering losses at the grain boundary due to the random orientation of each grain.
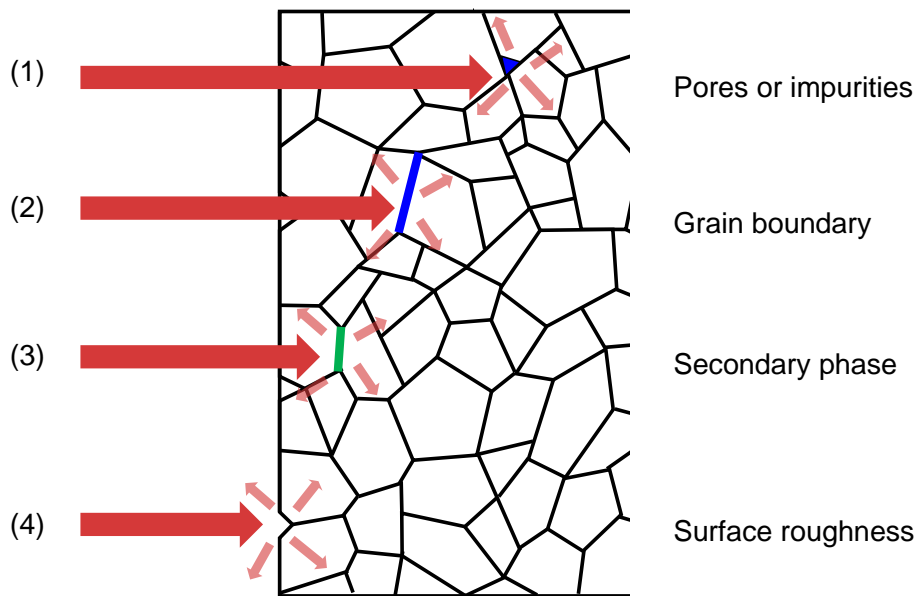
Figure 2.14: Scattering centers in ceramics.

So far, cubic structure materials such as garnets and cubic sesquioxides have been mainly fabricated. However, in recent years, there are several works to achieve highly transparent anisotropic ceramics using strong magnetic field alignment [95, 96] or finer grains [97, 98].

Sesquioxide ceramics have been highly developed as an alternative to single crystals. There are many reports of the successful fabrication of rare-earth doped sesquioxide ceramics, their spectroscopy [99], as well as CW [86, 100, 87, 83, 90] and ML laser operations [101, 102, 103, 104, 31, 105].

Table 2.2: List of crystallographic, spectroscopic, and thermo-mechanical properties of sesquioxides in comparison to YAG.

	Lu_2O_3	Sc_2O_3	Y_2O_3	$LuScO_3$	$LuYO_3$	$YScO_3$	$Y_3Al_5O_{12}$
Acronym	LuO	ScO	YO	LuScO	LuYO	YScO	YAG
Lattice structure	cubic	cubic	cubic	cubic	cubic	cubic	cubic
Space group	$Ia\bar{3}$	$Ia\bar{3}$	$Ia\bar{3}$	$Ia\bar{3}$	$Ia\bar{3}$	$Ia\bar{3}$	$Iad3$
Site symmetry	C_2/C_{3i}	C_2/C_{3i}	C_2/C_{3i}	C_2/C_{3i}	C_2/C_{3i}	C_2/C_{3i}	D_2
Cation radius (Å)	0.86	0.75	0.90	(0.81)	(0.88)	(0.83)	1.02
Lattice constant (Å)	10.391	9.857	10.602	10.124	10.497	10.230	12.00
Cation density (10^{22} cm^{-3})	2.852	3.355	2.687	(3.104)	(2.767)	(2.989)	1.39
Density (g cm^{-3})	9.42	3.85	5.03	(6.64)	(7.23)	(4.44)	4.56
Melting point (°C)	2450	2430	2430	2360	≈2350	≈2100	1940
Refractive index at 2 μm	1.9	1.95	1.87				1.80
Transparency range (μm)	0.225-8	0.21-8	0.22-8	0.23-			0.12-8
Thermal conductivity (W m^{-1}K^{-1})	12.8	18	13.4	3.6		6.24*	8.8-12.9
Thermo-optic coeff. $\frac{dn}{dT}$ (10^{-6}K)	7.1	10.8	8.3				9
Thermal expansion coeff. $\frac{1}{L}\frac{dL}{dT}$ (10^{-6}K)	8.6	9.6	6.3			≈9**	7
Max. phonon energy (cm^{-1})	612	669	592		≈603	≈633	857

* $(Y_{0.645}Sc_{0.355})_2O_3$ ** $(Y_{0.54}Sc_{0.46})_2O_3$
The values for mixed sesquioxides in brackets are averages of non-mixed sesquioxides.
The lattice constant of mixed sesquioxides were derived from Vegard's law.
The references for the values can be found in appendix A.

Chapter 3

Mode-locked laser

This chapter gives an introduction of mode-locked lasers; the mechanisms of optical pulse generation and practical mode-locking techniques. Before going to the mode-locking, the basics of quasi-three level lasers are described in Section 3.1. Subsequently, Section 3.2 explains the fundamentals of mode-locking, particularly for soliton mode-locking, which is achieved in the anomalous dispersion regime. Section 3.3 explains the mechanism of Kerr-lens mode-locking, which is adopted in this study, and its potential for the shortest pulse generation. Section 3.4 explains about the limitations of mode-locked operation regarding the shortest pulse duration, power scalability, and mode-locking instabilities. In addition, particularities of Tm^{3+} laser are described in Section 3.4.3.

3.1 Quasi-three level lasers

Before starting mode-locking experiments, we generally construct a CW laser to evaluate an efficiency of the laser, estimate a cavity loss, confirm a free running laser wavelength, and so on. In the 2 μm Tm laser system, laser transition takes place between the ground state $^3H_6$ and the first excited state $^3F_4$ manifolds. Since each manifold has the splitted sublevels, resulting in finite width, Tm lasers are generally classified as quasi-three (quasi-four) level lasers. This section gives the basics of quasi-three level continuous wave lasers. Figure 3.1 shows a schematic of the quasi-three level laser. When ions are excited to the upper manifold, they are distributed to the Stark sublevels according to Boltzmann distribution. Subsequently, the excited ions will be relaxed to the lower manifold via radiative/nonradiative processes. The sum of ion density in the upper and lower manifolds are equal to the density of dopant ions N_{dop} as follows:

$$N_1 + N_2 = N_{\mathrm{dop}}. \tag{3.1}$$

The change of the ion density in the upper manifold can be described as follows:

$$\frac{dN_2}{dt} = W_p N_1 - \frac{qc}{A_{\mathrm{eff}} l_c}(\sigma_{\mathrm{em}} N_2 - \sigma_{\mathrm{abs}} N_1) - \frac{N_2}{\tau_f}, \tag{3.2}$$
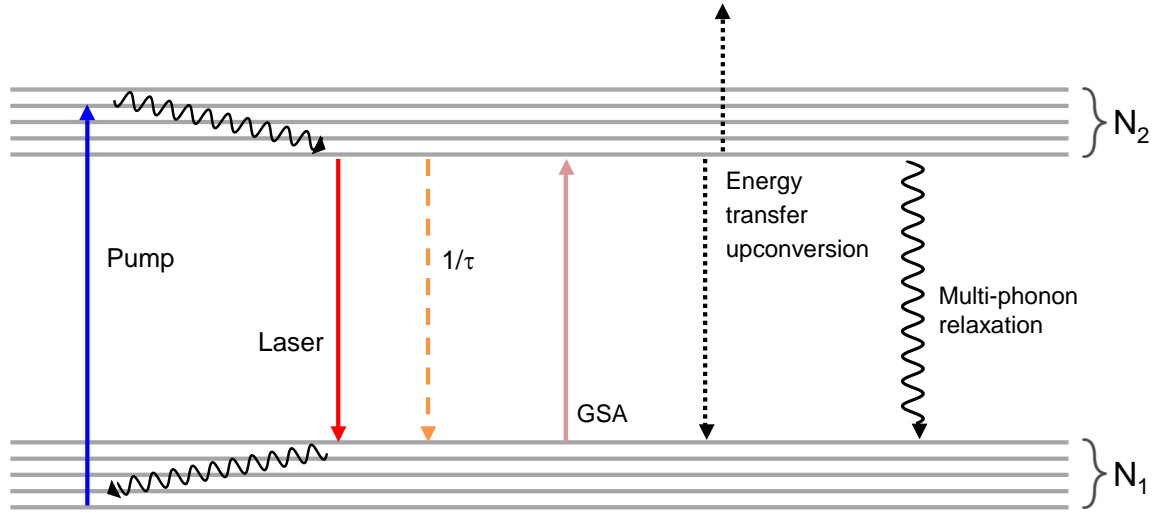
Figure 3.1: Schematic of the quasi-three level laser.

where W_p is the pumping rate, q is the photon number in the laser mode, A_{eff} is the effective laser mode area, l_c is the optical path length of the cavity, σ_{em} and σ_{abs} are the emission and absorption cross sections, and τ_f is the fluorescence lifetime of the upper manifold. Under lasing, ion numbers became steady state, thus Eq. (3.2) equals to 0. The threshold pump power of the quasi-three level laser with the intracavity loss L_i and the output coupling loss T_{OC} can be described as follows [106]:

$$P_{\text{th}} = \frac{h\nu_p(V_{\text{eff}}/l_c)}{2\eta_q\eta_a(f_1 + f_2)\sigma\tau_f}(L_i + T_{\text{OC}} + 2N_1^0\sigma l), \tag{3.3}$$

where $h\nu_p$ is the pump photon energy, η_q is the quantum efficiency that indicates the ratio of ions in the upper laser level created by an absorbed photon, η_a is the pump absorption efficiency, f_1 and f_2 are the fractional population in the lower and upper laser level, respectively. N_1^0 is the ion density in the lower laser level at unpumping condition (doped ion density) and V_{eff} is the effective mode volume of the laser mode. Since Tm^{3+} lasers' behavior is affected by interionic processes such as ETU and CR, the accurate analysis for laser performance needs to take these processes into account. Ref. [107] gives a modeling of Tm lasers accounting for upconversion and ground-ground state depletion. Once lasing starts, the laser output power linearly increases with the pump power as

$$P_{\text{out}} = \eta_{\text{sl}}(P_{\text{pump}} - P_{\text{th}}). \tag{3.4}$$

Here, η_{sl} is called slope efficiency, which includes any efficiencies which affect laser performance. It can be described as follows:

$$\eta_{\text{sl}} = \eta_{\text{st}} \cdot \eta_q \cdot \eta_a \cdot \frac{T_{\text{OC}}}{T_{\text{OC}} + L_i} \cdot \eta_{\text{overlap}} \cdot \dots, \tag{3.5}$$

where η_{st} is Stokes efficiency determined by the ratio of pump and laser photon energies, η_{overlap} is overlapping efficiency of the pump and laser modes. The slope efficiency η_{sl} can be derived from

the pump power and the laser output power. To find the slope efficiency is useful to estimate the intracavity loss using Eq. (3.5). Since all efficiencies are smaller than unity, the following relationship can be obtained,

$$\eta_{\text{sl}} < \eta_{\text{st}} \cdot \frac{T_{\text{OC}}}{T_{\text{OC}} + L_i}. \tag{3.6}$$

The stokes efficiency $\eta_{\text{st}} = \lambda_{\text{pump}}/\lambda_{\text{laser}}$ is known from pump and laser wavelengths. From Eq. (3.6), the intracavity loss L_i can be expressed as follows:

$$L_i < T_{\text{OC}} \cdot (\frac{\eta_{\text{st}}}{\eta_{\text{sl}}} - 1). \tag{3.7}$$

Therefore, smaller transmittance output coupler (OC) is useful to estimate the cavity loss more precisely. The Caird analysis is a well-known method to estimate the cavity loss from the slope efficiencies with different transmittance OCs [108]. The Caird analysis is according to $\eta_{\text{sl}} = \eta_0 \cdot T_{\text{OC}}/(T_{\text{OC}} + L_i)$ where η_0 is the internal slope efficiency defined as the slope efficiency with $T_{\text{OC}} = 0$. Theoretically, the slope efficiency increases as increasing the output coupling. However, in Tm lasers, for larger OCs, the laser performance will be deteriorated [109, 27, 61, 110]. This is mostly explained by the increased thermal load indirectly induced by ETU between excited Tm^{3+} ions. ETU is depending on the ion density on the upper laser level $^3\text{F}_4$, and the excited ions via ETU generate heat with relaxation. Thus thermal load will increase at higher inversion levels, leading to thermal lensing and cavity-mode instabilities. Such phenomenon is also experimentally found in other rare-earth ion doped lasers [111, 112, 113] even in Yb lasers [114, 115] which have only two manifolds. This would be explained by the same mechanism, increased thermal load induced by energy transfer from an excited ion to another dopant ion or impurities in active materials.

3.2 Fundamental physics of mode-locking

Mode-locking is a technique to obtain periodic optical pulses by locking the relative phase of the longitudinal modes oscillating in the cavity. The effective gain at a certain optical frequency ν valances with the loss of the cavity [116] as follows:

$$\gamma_t(\omega) = \alpha - \frac{1}{l} \ln r_1 r_2, \tag{3.8}$$

where γ_t is the effective gain, α is a linear loss of the cavity round trip, l is the length of gain material (assuming that l is the same as the cavity length), and r_1 and r_2 are the reflectivities of cavity mirrors. The frequency interval of the longitudinal modes is determined by the optical length of the cavity as follows:

$$\nu_{k+1} - \nu_k = \frac{c}{2nl}. \tag{3.9}$$

Here, if the gain is sufficient to overcome the loss, several longitudinal modes which have a spectral distance with Eq. (3.9) can oscillate simultaneously as shown in Fig. 3.2. When multiple longitudinal modes oscillate, the optical-electric field at an arbitrary point can be described as follows:

$$E(t) = \sum_m C_m \exp\left[(\omega_0 + m + \Omega)t + \phi_m\right], \tag{3.10}$$
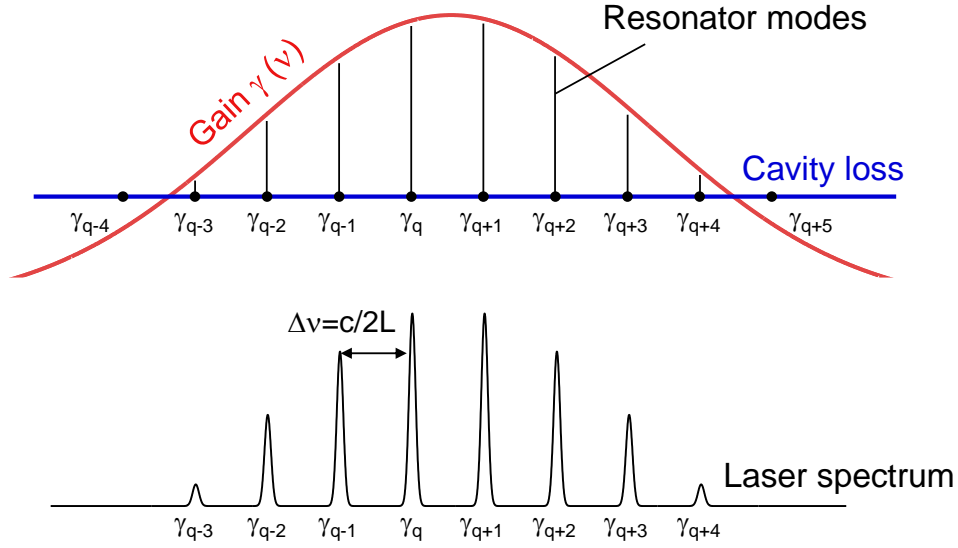
Figure 3.2: Schematic of multi-longitudinal mode structure in a laser.

where C_m is amplitude, ϕ_m is the phase of the mth mode, and Ω is the free spectral range of angular frequency ($\Omega = \pi c/l$). Equation (3.10) is a periodical function with a period of $\tau \equiv 2\pi/\Omega$. τ is equivalent to the cavity round-trip time. Optical-electric field at $t + \tau$ is described as follows:

$$
\begin{aligned}
E(t+\tau) &= \sum_m C_m \exp\left\{ i\left[(\omega_0 + m\Omega)\left(t + \frac{2\pi}{\Omega}\right) + \phi_m \right] \right\} \\
&= \sum_m C_m \exp\left\{ i\left[(\omega_0 + m\Omega)\,t + \phi_m \right] \right\} \exp\left\{ i\left[2\pi\left(\frac{\omega_0}{\Omega} + m\right) \right] \right\} \\
&= E(t) \exp\left(i2\pi\omega_0/\Omega \right).
\end{aligned}
\tag{3.11}
$$

Equations (3.10) and (3.11), are the same except for some phase terms. $E(t)$ can be periodical when ϕ_m is constant in time. However, in general, ϕ_m is unstable and easy to change in time. Consequently, intensity of the laser will vary in time and deteriorate the temporal coherence. This is caused by random interference between oscillating modes. Mode-locking technique is relative phase ϕ_m between the modes. For example, when the phase ϕ_m of all modes is 0 and assuming that the amplitude of each mode C_m is identical, the optical-electric field can be described as:

$$
\begin{aligned}
E(t) &= \frac{1}{\sqrt{N}} \sum_{m=1}^{N} \exp\left[i(\omega_0 + m\Omega)t \right] \\
&= \frac{1}{\sqrt{N}} \exp\left\{ i[\omega_0 + (N+1)\Omega/2]t \right\} \frac{\sin(N\Omega t)}{\sin(\Omega t/2)}.
\end{aligned}
\tag{3.12}
$$

Here, the amplitude of electric field is normalized to have constant energy independent of N. As a result, the power of the laser is proportional to $E(t)E^*(t)$ and described as follows:

$$
P(t) \propto \frac{1}{N} \frac{\sin^2(N\Omega t/2)}{\sin^2(\Omega t/2)}.
\tag{3.13}
$$

Mathematically, Eq. (3.13) indicates following characteristics:

1. Mode-locked pulses are extracted from the cavity by a period of $\tau = 2\pi/\omega = 2l/c$ which is corresponding to the round-trip time.

2. Peak intensity is scaled by the number of modes N.

3. A pulse width is determined as $\tau_0 = \tau/N$. When $N \gg 1$, the pulse width approaches to FWHM of the peak.

To simplify Eq. (3.12), the electric field of an optical pulse can be written as follows:

$$E(t) = A(t) \exp\left[i(\Phi(t) - \omega_0 t)\right] + c.c., \tag{3.14}$$

where A(t) is an electric fied envelope, $\Phi(t)$ is the phase, and ω_0 is the center angular frequency. The notation in the frequency domain can be derived via Fourier transformation and resulting in:

$$E(\omega) = \frac{1}{\sqrt{2\pi}} \int_0^\infty A(\omega) \exp\left[i(\phi(\omega) - \omega_0 t)\right]d\omega + c.c.. \tag{3.15}$$

The soliton mode-locked pulse has the sech^2 shaped envelope, thus $A(t)$ in Eq. (3.14) and intensity $I(t)$ are

$$A(t) = A_0 \mathrm{sech}(\frac{t}{\tau}),$$
$$I(t) = A_0^2 \mathrm{sech}^2(\frac{t}{\tau}). \tag{3.16}$$
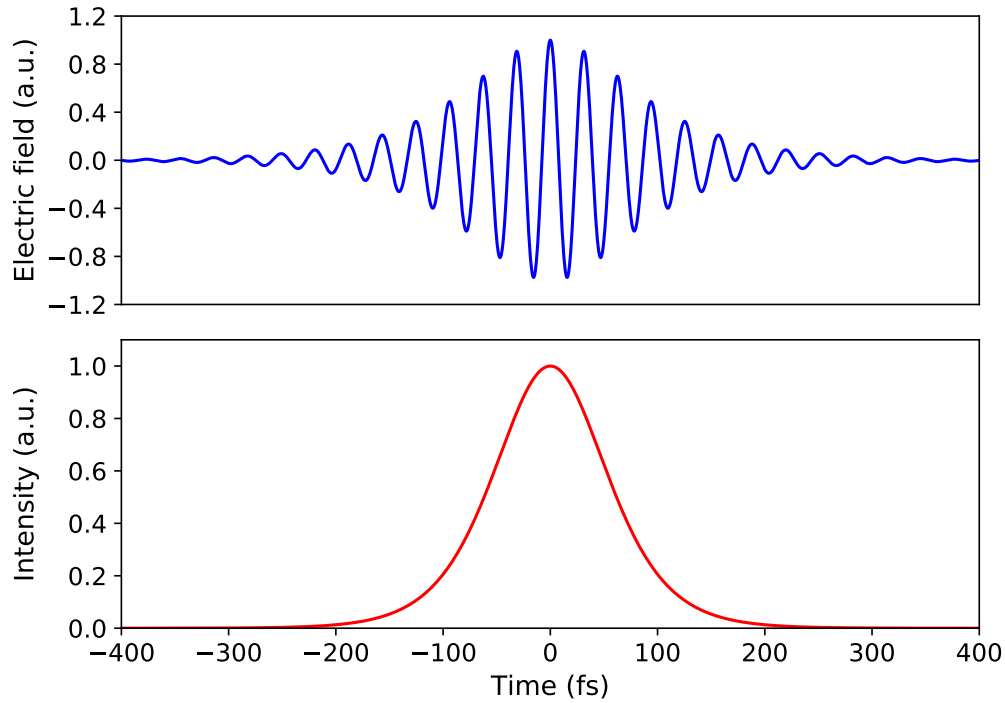
Figure 3.3: Schematic of electric field and intensity of optical pulse.

The schematics of the electric field and intensity of an optical pulse in the time domain is shown in Fig. 3.3. Here, A_0 and τ are constant. τ is related to the pulse width as $\tau_p = 1.67\tau$. According to the uncertainty principle, the pulse width τ_p and the spectral bandwidth $\Delta\nu$ (FWHM) of optical pulse have the following relationship.

$$\tau_p \cdot \Delta\nu \geq k. \tag{3.17}$$

where k is a constant which is depending on the pulse envelope shape, e.g. 0.441 for Gaussian shaped pulse and 0.315 for sech^2 shaped pulse. Eq. (3.17) means that broader spectral bandwidth results in shorter pulse width. When $\tau_p \cdot \Delta\nu = k$, the optical pulse has no chirp [cf. Chapter 3.2.1] and is called Fourier transform limited pulse.

3.2.1   Soliton mode-locking

Soliton is one of the mathematical resolutions of nonlinear equations. Soliton waves can propagate with constant shape and velocity. Soliton mode-locked pulses are pulses with a certain balance between self phase modulation (SPM) and negative dispersion. It enables to maintain pulse shape during propagation by canceling negative dispersion and SPM each other. In solid-state bulk lasers, as the laser cavity is composed of spatially discrete optical components such as active medium and dispersion mirrors, the generated optical pulse in effective anomalous dispersion regime is so-called *quasi-soliton* pulse.

Self-phase modulation

A temporal profile of an optical pulse causes the optical Kerr effect by interacting with nonlinear χ^3 materials. Once the optical pulse incident to the nonlinear material, the refractive index of the material will change according to the light intensity. The intensity-dependent refractive index is written as:

$$n(I) = n_0 + n_2 I(t). \tag{3.18}$$

Subsequently, the modulated refractive index will induce an intensity-dependent phase shift. This is so-called self-phase modulation (SPM).

The phase shift caused by SPM for the propagation of a distance L is written as:

$$\Phi(t) = -\omega_0 t + \frac{\omega_0}{c}(n_0 + n_2 I(t))L. \tag{3.19}$$

Here, the carrier frequency $\omega(t)$ determined by differentiating Eq. (3.19) is as follows:

$$\begin{aligned}
\omega(t) &= \frac{d\Phi(t)}{dt} = \omega_0 - \frac{\omega_0}{c}n_2 L \frac{dI(t)}{dt} \\
&\equiv \omega_0 + \delta\omega(t),
\end{aligned} \tag{3.20}$$

where $\delta\omega(t)$ is the frequency shift due to SPM. Intensity-dependent frequency modulation of an optical pulse is illustrated in Fig. 3.4(a, b). The strength of SPM depends on the light intensity as well as the nonlinear refractive index n_2 which is a materials' intrinsic parameter. Eventually, SPM modulates the carrier frequency of the optical pulse while maintaining the envelope of the electric

field. In other words, SPM *chirps* the optical pulse. Figure 3.4(c) shows an example of an electric field modulated by SPM. For positive nonlinear refractive indices $n_2 > 0$, the phase velocity of the higher frequency component is faster, so the pulse is *positive* chirped. In the frequency domain, the optical spectrum becomes broader.
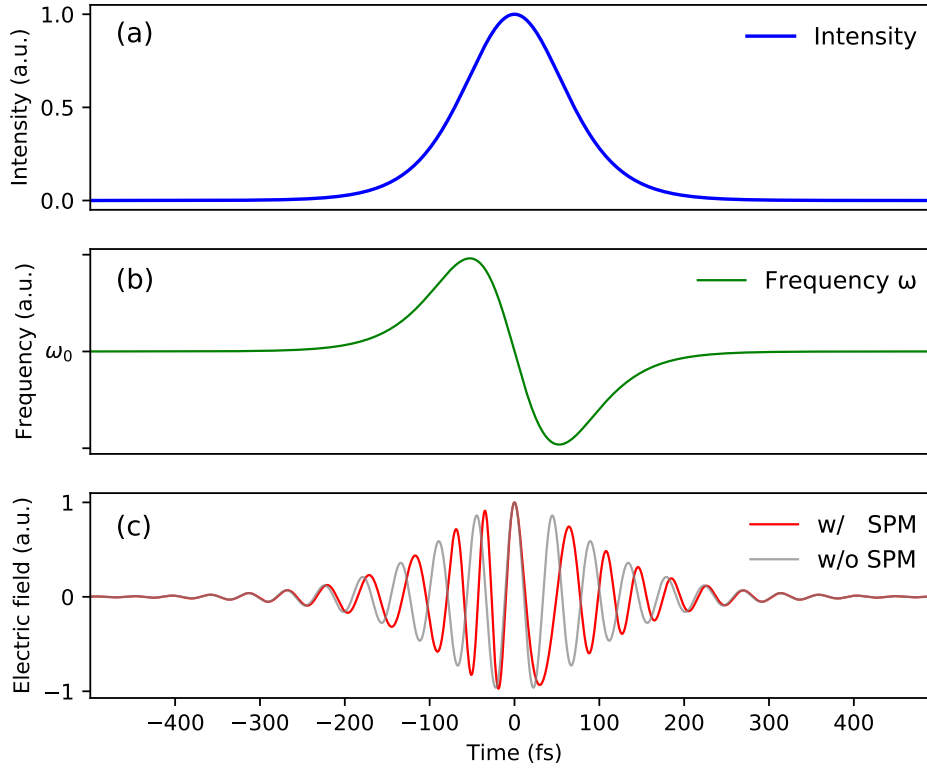
Figure 3.4: Schematics of SPM. (a) Intensity of optical pulse, (b) modulated frequency of optical pulse and (c) modulated electric field.

Dispersion

When an optical pulse passes through a dispersive element, it undergoes a frequency chirp. The phase of the optical pulse $\phi(\omega)$ in Eq. (3.15) can be expressed as the following Taylor series:

$$\phi(\omega) = \phi_0 + \frac{d\phi(\omega)}{d\omega} \cdot (\omega - \omega_0) + \frac{1}{2!} \frac{d^2\phi(\omega)}{d\omega^2} \cdot (\omega - \omega_0)^2 + \dots. \tag{3.21}$$

The first term is a constant which is independent from ω, thus it does not cause frequency chirp. The second term corresponds to linear phase shift and the third and higher terms correspond to nonlinear chirp. The coefficients $\frac{d\phi(\omega)}{d\omega}$ in the second term and $\frac{d^2\phi(\omega)}{d\omega^2}$ in the third term are known as GVD and GDD, respectively. The coefficients of higher-order terms are so-called high-order dispersion (HOD). The frequency chirp in the laser cavity is caused by material dispersion, angular dispersion, waveguide dispersion, and so on. If GDD and HOD are not 0, the phase of each longitudinal mode of the pulse is not synchronized, resulting in the change of the pulse shape. Therefore, to obtain the

shortest pulse duration without chirping, dispersion compensation is important. Chirp-free pulse corresponds to transform-limited pulse. In general, the influence of HOD on the pulse width is significantly small compared with GDD. For the design of ML solid-state lasers, GDD is primarily taken into account.

The propagation of a slowly varying finite amplitude plane wave considering SPM and GDD, known as the nonlinear Schroödinger equation, is written as:

$$\frac{\partial A(z,\tau)}{\partial z} = \frac{1}{2}ik_2\frac{\partial^2 A(z,\tau)}{\partial \tau^2} - i\gamma|A(z,\tau)|^2 A(z,t). \tag{3.22}$$

The second term respects the influence of dispersion and k_2 is GDD. The third term corresponds to SPM where γ is the SPM coefficient expressed as

$$\gamma = \frac{n_2\omega_0}{cA_{eff}}, \tag{3.23}$$

where A_{eff} is the laser effective mode-field area. From this equation, by solving for $\partial A/\partial z = 0$, the pulse energy of the soliton E_p and pulse duration τ have the following relationship:

$$E_p = \frac{1.76|D_2|}{\gamma\tau}, \tag{3.24}$$

where D_2 is a total GDD per cavity round-trip and this is so-called the fundamental soliton solution.

3.3   Kerr-lens mode-locking

To achieve phase locking between oscillating longitudinal modes (mode-locking) as described above, the modulation with the period of cavity round trip time $c/2L$ is needed. In the CW regime, the distance between adjacent longitudinal modes is not constant because of dispersion. By applying modulation with the period of $c/2L$, sidebands created by the modulation couple to adjacent longitudinal modes, resulting in synchronization with the original laser mode. Consequently, the relative phase of numerous longitudinal modes is locked. This effect is so-called frequency pulling. As the modulator, the saturable absorber (SA) is generally used for passive mode-locking. The SA has higher absorption for only lower-intensity light. By inserting the SA in the laser cavity, since weak light is affected by higher loss, only high-intensity light (pulse) can survive during propagation. There are *real* and *artificial* SA. The *real* SA means nonlinear elements such as semiconductor saturable absorber mirror (SESAM), single-walled carbon nanotube (SWCNT), graphene, black phosphorus, transition metal dichalcogenides, topological insulator, and so on [117]. They are basically solid-state components and have finite unsaturated losses. The *artificial* SA is the method creating nonlinear loss or gain based on nonlinear optical effect, e.g. Kerr-lens mode-locking, nonlinear polarization rotation (NPR), nonlinear optical/amplifying loop mirror (NOLM/NALM), and Mamyshev oscillator. In general, the *real* SA benefits for self-start operation and long-term stability. However, they are usually categorized as slow SA and have smaller modulation depth. On the contrary, since the *artificial* SA is based on nonlinear effect, the response time can be femtosecond order, thus they are

categorized as fast SA.

Kerr-lens mode-locking (KLM) is one of the artificial SA using the optical Kerr effect. When high-intensity light incidents to a nonlinear medium, the refractive index will change $n(I) = n_0 + n_2 I$ by the optical Kerr effect. The change of the refractive index affects the spatial profile of the incident beam as well as the temporal profile. If the incident beam has a Gaussian shape, the refractive index will change according to the spatial beam profile, resulting in lensing effect and self-focusing of the beam. This is called Kerr-lensing and more intense light will undergo tighter focusing.
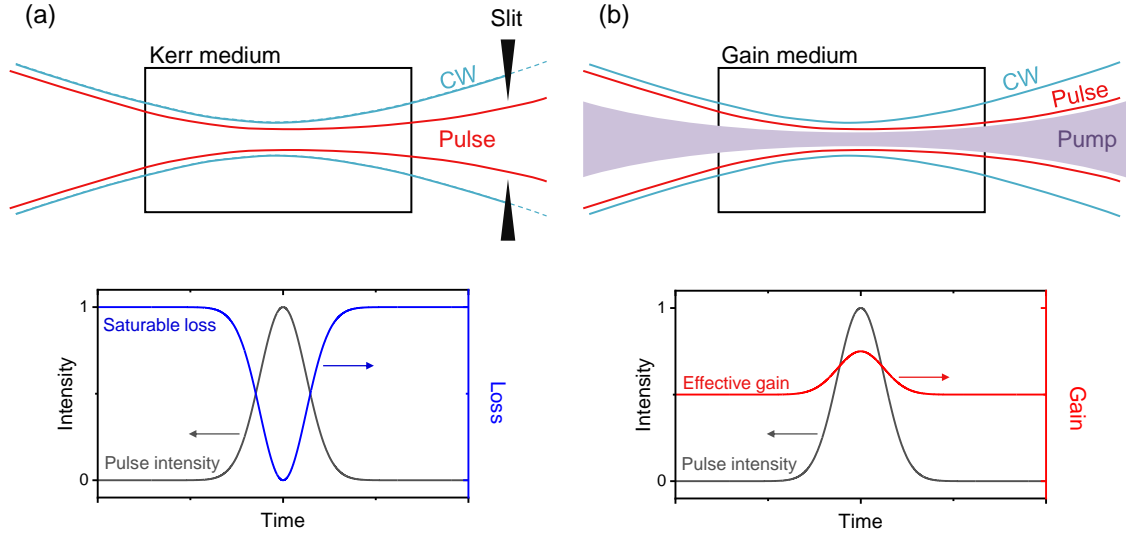
Figure 3.5: Schematic of Kerr-lens mode-locking using (a) hard aperture effect and (b) soft aperture effect.

KLM is categorized into two different methods to obtain the modulation. Figure 3.5 shows the schematic of the KLM with two types of modulation. By inserting the slit to add losses only for high intense part of the beam can survive during round-trips, thus loss modulation can be obtained as shown in Fig. 3.5(a). The other method is achieved by setting the pump beam slightly smaller than the continuous wave laser mode, high intense part tightly focused by Kerr-lensing will obtain higher gain. That makes gain modulation (Soft-aperture effect). In other words, KLM is achieved by optimizing the cavity condition for the high intense light (pulsed light). Therefore, if the CW component can not satisfy the stable condition and only pulsed component can lase, modulation depth could be theoretically 100%, which is similar to the idea of Mamyshev oscillator which can completely suppress the CW components [118, 119]. In general, as the nonlinear refractive index n_2 reduces at longer wavelengths, Kerr-lensing effect becomes weaker at longer wavelengths. Moreover, the Rayleigh length becomes shorter at longer wavelengths, thus KLM at 2 μm wavelength range is more challenging compared with conventional near-infrared (NIR) range. For Tm-based lasers, KLM Tm lasers at 2 μm and 2.3 μm wavelength ranges have been demonstrated in 2017 for the first time [120, 121]. Both KLM lasers were achieved by a detailed cavity design and high beam quality pump lasers.

In this study, we adopted the soft-aperture KLM to achieve pulsed laser operation. KLM has some advantages compared with other mode-locking method. Table 3.1 shows a comparison of KLM

and SESAM mode-locking which is the most common "real" SA in the 2 µm lasers. KLM enables large modulation depth, a fast response time, and a high damage threshold. Moreover, soft aperture KLM is using gain modulation mechanism, thus it does not need any loss elements (no unsaturated losses). This is actually the most established method to achieve the shortest pulse generation from various solid-state lasers [122, 123, 21]. However, since KLM is achieved using the spatial change of beam profile, it is quite sensitive to the alignment. As a result, self-start operation and long-term stability are generally challenging. The practical cavity design for KLM lasers is described in section 3.5.

Table 3.1: Comparison of KLM and SESAM mode-locking.

	KLM (Soft-Apeature)	SESAM*
Relaxation time	fs	1-30 ps
Nonsaturable loss	0	1-30%
Modulation depth	overlap ratio between pump and laser	1-30%**
Damage threshold	J/cm^2***	$\sim$mJ/cm^2
Long term stability	$\times$	$\bigcirc$
Self-start	$\times$	$\bigcirc$

*referred to BATOP, GmbH

**depends on nonsaturable loss

***depends on the host material. For sesquioxides: [124]

3.4 Limitations of mode-locked operation

3.4.1 Q-switching instability

Q-switch instability is a problem in mode-locking operations. Figure 3.6 illustrates CW mode-locking and Q-switch mode-locking. The latter is originated from a fluctuation of the population inversion caused by the nonlinear loss depending on the intracavity intensity [125]. A giant pulse generated by Q-switch instability could damage optics, thus this is an undesirable phenomenon for most of the time. The suppression of Q-switch instability has been studied mostly focusing on the SESAM mode-locking [126, 127]. The simple criteria were derived for suppressing Q-switch instability. However, the criteria are based on the assumption of an invariant spatial beam profile, thus it can not be applied for KLM with a significant beam profile change. The criteria for KLM was developed in Ref. [128]. The basic criterion for Q-switch instability can be written as:

$$\frac{1}{\tau_{\text{inv}}} + \frac{\tilde{P}}{E_{\text{sat}}} > - \left. \frac{\tilde{P}}{T_R} \frac{dq}{dP} \right|_{\tilde{P}} .$$

(3.25)

where $1/\tau_{inv}$ is the decay rate of the population inversion, $\tilde{P}/E_{sat}$ is the stimulated transition probability, T_R is the round trip time, q is the nonlinear loss per round trip, and $\tilde{P}$ is the average power. The left-hand side of Eq. (3.25) can be regarded as the effective rate of gain recovery and the right-hand side represents the rate of change of the nonlinear loss. Therefore, when the gain

recovery rate exceeds the change of nonlinear loss, the mode-locking remains stable. Further detailed discussion about this theory for the case of KLM is discussed in [128]. Practically, in the general soft-aperture KLM lasers, Q-switch instability can be suppressed by increasing intracavity power, making the spatial mode matching between the pump beam and the cavity mode. The latter can be achieved by optimizing the cavity design and the alignment.
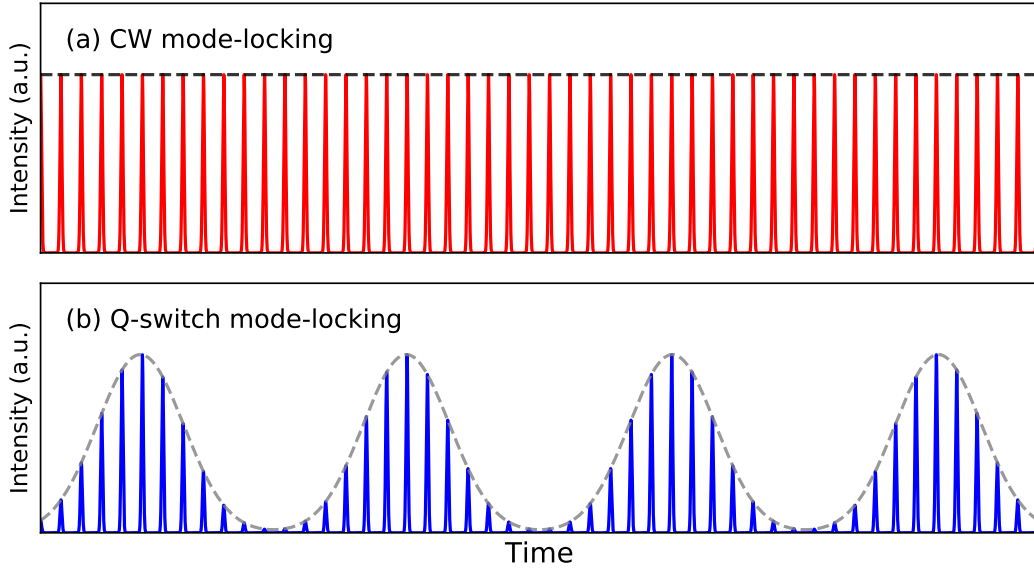
Figure 3.6: Schematic of (a) CW and (b) Q-switch mode-locking.

3.4.2 Multi-pulse operation

When the pulse duration in the ultrashort pulse lasers is close to the minimal value, the laser operation tends to show instability and pulse splitting. As the net GDD reduces to zero, a nonregular pulsing or a stable multi-pulse operation often occurred [129]. While the multi-pulse operation is generally considered as an obstacle for pulse shortening, this can be also used to achieve high repetition rate lasers by harmonic mode-locking [130]. The nature of the destabilization of single-pulse operation in the soliton-mode-locked regime is owed to the interplay between the gain and loss saturation in the combination with spectral filtering. As a result, stable multi-pulse operation is caused via background amplification due to insufficient gain saturation by the pulse with reduced pulse energy or excitation of the pertubation bounded within the high-energy pulse. Figure 3.7 shows an example of the optical spectrum and the waveform in a multi-pulse laser operation. In mode-locked laser experiments, the transition from single-pulse to multi-pulse operation is observed when the pump power increased. In the multi-pulse operation, the average output power and pulse duration increase, and a pulse energy decreases. The spectral bandwidth becames narrower compared with single-pulse operation and sometimes the spectral fringes can be seen. The fringe is corresponding to the pulse-to-pulse distance.

To suppress the multi-pulse operation, the following methods are available: decrease of the pump power, decrease of the gain relaxation time, increase of modulation depth, increase of output

coupling, and increase of the gain saturation.
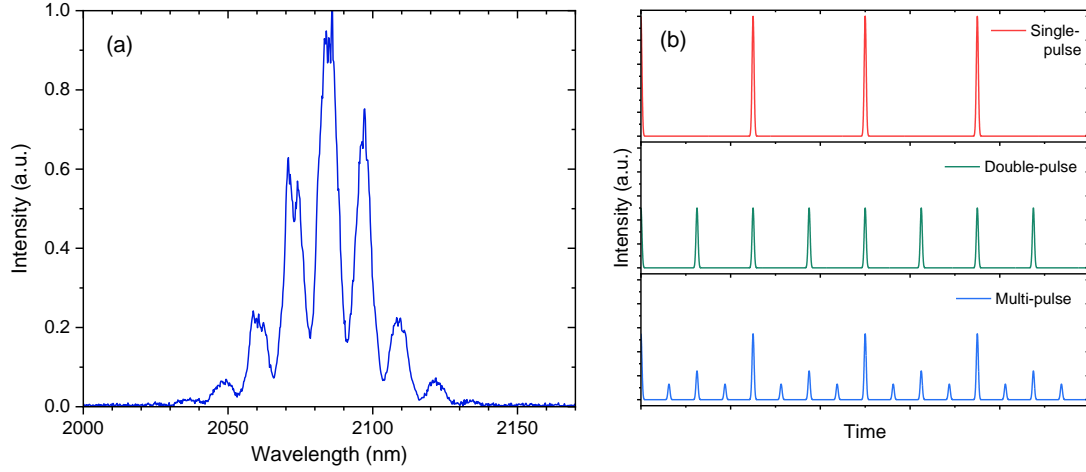
Figure 3.7: (a) Example of observed optical spectrum and (b) schematics of pulse train of multi-pulse operation.

3.4.3 Available shortest pulse duration from Tm laser

Here we discuss about the limit of the shortest pulse duration from mode-locked Tm lasers considering the above-mentioned factors. First of all, since the stable single-pulse mode-locking is sustained by sufficient gain saturation for the whole spectral range, the gain medium with a broad and flat gain profile is necessary for ultrashort pulse generation. However, a large modulation depth and sufficiently strong SPM can overcome the gain bandwidth limitation [131]. This enables to broaden mode-locked spectrum beyond the gain bandwidth. Of course, the spectral component outside of the gain profile can not contribute to gain saturation. From this point of view, broadened spectral components can be considered as an additional loss for the ML pulse. Therefore, to sustain ML operation, the laser cavity should be satisfied the following condition:

$$L_{\mathrm{ML}} + L_{\mathrm{SA}} < L_{\mathrm{CW}}, \tag{3.26}$$

here, L_{ML} is the total loss for ML pulse, L_{SA} is the loss caused by SA effect, and L_{CW} is the total loss for CW laser. This also can be explained by gain, the effective gain for ML pulse must exceed that for CW. In the general ML lasers, this is achieved by SA effect suppressing CW lasing. Therefore, large modulation depth is the key to sustain spectral broadening even for outside of the gain. It should be noted that the pulse duration and the pulse energy have a relationship from Eq.(3.23) and (3.24) as:

$$\tau_{\mathrm{soliton}} = \frac{1.76|D_2|}{E_p} \frac{\lambda A_{\mathrm{eff}}}{n_2}. \tag{3.27}$$

In this equation, n_2 is the specific value for the gain media and/or Kerr-medium in the cavity. Generally, Tm-based gain material shows particularly small n_2 compared with other laser active materials. Since the refractive index and nonlinear refractive index decrease as wavelength became longer, Tm-doped materials show smaller value than that of 1 μm Yb- and 1.5 μm Er-based gain

materials. In addition, 2.4 μm Cr:ZnS/ZnSe chalcogenide laser materials show an order of magnitude higher value. Therefore, the basic strategy for ultrashort pulse generation from Tm-based lasers is increasing pulse energy by making high-Q cavity with smaller GDD and low transmittance OC. Under these conditions, while the average output power should decrease for the shortest pulse generation, it enables significantly high intracavity peak power, e.g., graphene mode-locked Cr:ZnS laser generates pulses as short as 45 fs with an average output power of 500 mW at a repetition rate of 64.7 MHz using a 34% OC [132], resulting in an intracavity peak power of 0.47 MW. KLM Tm:Lu$_2$O$_3$ laser achieved a pulse duration of 60 fs with an average output power of 81 mW at a repetition rate of 93.7 MHz using a 0.5% OC [133], resulting in an intracavity peak power of 2.9 MW. This unique feature is interesting for applications using nonlinear process such as spectral broadening using intracavity SRS [134, 135], Brillouin feedback and/or SC generation [136] as well as intracavity second harmonic generation (SHG) or HHG.

3.5 Cavity design for Kerr-lens mode-locked laser

3.5.1 ABCD matrix calculation

Before starting the experiments, we need to design a laser cavity. Temporal and spatial evolution of the electric field of the laser output can be analyzed by the Maxwell equation. However, the Gaussian profile laser beam can be applied to geometrical analysis using q parameter defined as follows:

$$\frac{1}{q(z)} = \frac{1}{R(z)} - j\frac{\lambda}{\pi n_0 w^2(z)}, \tag{3.28}$$

where $R(z)$ indicates the curvature radius of the wavefront of the Gaussian beam and $w(z)$ is the beam spot diameter. The propagation of a Gaussian beam is shown in Fig. 3.8.
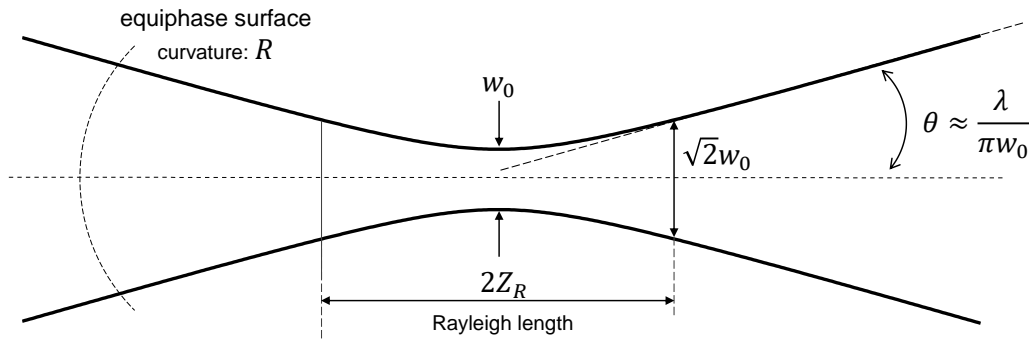
Figure 3.8: Propagation of a Gaussian beam.

When the Gaussian beam passes optics such as a lens, the modified Gaussian beam can be expressed as follows:

$$q_2 = \frac{Aq_1 + B}{Cq_1 + D}, \tag{3.29}$$

where, $A, B, C,$ and D are the elements of ray-transfer matrices of the optics defined as

$$\begin{bmatrix} r_{\text{out}} \\ r'_{\text{out}} \end{bmatrix} = \begin{bmatrix} A & B \\ C & D \end{bmatrix} \begin{bmatrix} r_{\text{in}} \\ r'_{\text{in}} \end{bmatrix}, \tag{3.30}$$

where, r and r' are the position of the beam height and the angle against the optical axis, respectively. Table 3.2 shows the coefficients of basic ray-transfer matrices. This expression of ray-transfer matrices is quite useful when we deal with complex series of optics for the cavity design. When the Gaussian beam passed the multiple optics, the ray-transfer matrices can be expressed as the product of each of the independent matrices as shown in Fig. 3.9.

$$\begin{bmatrix} A_T & B_T \\ C_T & D_T \end{bmatrix} = \begin{bmatrix} A_{n-1} & B_{n-1} \\ C_{n-1} & D_{n-1} \end{bmatrix} \cdots \cdot \begin{bmatrix} A_2 & B_2 \\ C_2 & D_2 \end{bmatrix} \cdot \begin{bmatrix} A_1 & B_1 \\ C_1 & D_1 \end{bmatrix}, \tag{3.31}$$

$$q_{\text{out}} = \frac{A_T q_{\text{in}} + B_T}{C_T q_{\text{in}} + D_T}. \tag{3.32}$$

Therefore, the above expression enables us to define the curvature and beam diameter of the Gaussian beam during propagation.

$$\begin{bmatrix} A_T & B_T \\ C_T & D_T \end{bmatrix} = \begin{bmatrix} A_3 & B_3 \\ C_3 & D_3 \end{bmatrix} \begin{bmatrix} A_2 & B_2 \\ C_2 & D_2 \end{bmatrix} \begin{bmatrix} A_1 & B_1 \\ C_1 & D_1 \end{bmatrix}$$
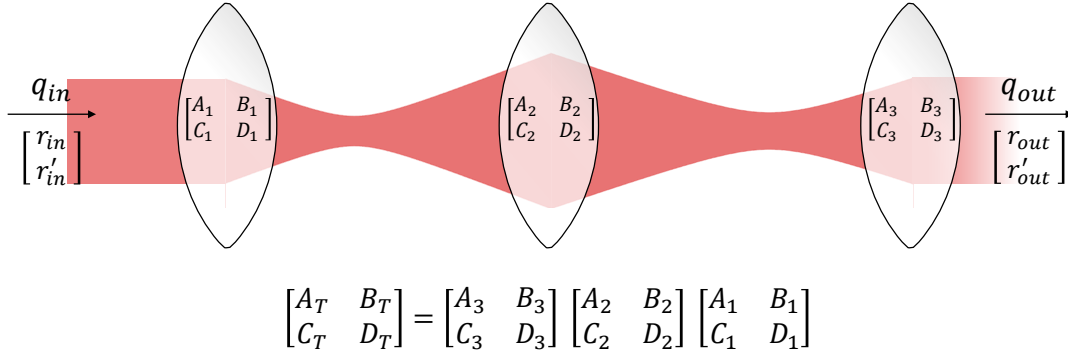
Figure 3.9: Ray-transfer matrix of series of optics.

For the stable laser cavity, the laser mode parameter must be identical at the same position after a round trip, thus, the q-parameter is imposed so-called self-consistent condition [116],
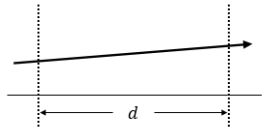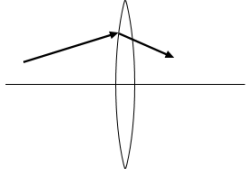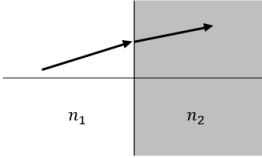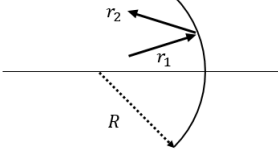
$$q_s = \frac{A q_s + B}{C q_s + D}. \tag{3.33}$$

Since the ray-transfer matrix is the unimodular matrix, the condition can be modified by sovling Eq. (3.33) for q_s as follows.

$$\frac{1}{q_s} = \frac{(D - A) \pm \sqrt{(D - A)^2 + 4BC}}{2B} \tag{3.34}$$

$$= \frac{D - A}{2B} + j\frac{\sin\theta}{B}. \tag{3.35}$$

Table 3.2: Ray-transfer matrices for basic optics

Parallel plate with thickness d		$\begin{bmatrix} 1 & d \\ 0 & 1 \end{bmatrix}$
Thin lens with the focal length f		$\begin{bmatrix} 1 & 0 \\ -\dfrac{1}{f} & 1 \end{bmatrix}$
Interfaces of media with different refractive indices		$\begin{bmatrix} 1 & 0 \\ 0 & \dfrac{n_1}{n_2} \end{bmatrix}$
Spherical mirror with curvature R		$\begin{bmatrix} 1 & 0 \\ -\dfrac{2}{R} & 1 \end{bmatrix}$

Here,

$$\theta = \left| \cos^{-1}\left(\frac{D+A}{2} \right) \right|. \tag{3.36}$$

The beam diameter can be defined from Eq. (3.28), and it must have a finite value. Therefore, the stable condition for the laser cavity can be described as follows:

$$\left| \frac{D+A}{2} \right| < 1. \tag{3.37}$$

Under this stable condition, the beam radius w at the arbitrary position in the laser cavity can be calculated using the matrix elements.

$$w = \left(\frac{\lambda}{\pi n} \right)^{1/2} \frac{(|B|)^{1/2}}{[1 - [(D+A)/2]^2]^{1/4}}. \tag{3.38}$$

Figure 3.10 shows the example of the cavity design for the simple plane-concave linear cavity which is utilized in Chapter 5. The laser performance is strongly depending on the pump density and the mode-matching efficiency between the pump and laser mode in the gain medium (cf. Section 3.1). Therefore, the proper choice of the cavity configuration and the lens unit for pump focusing are important.
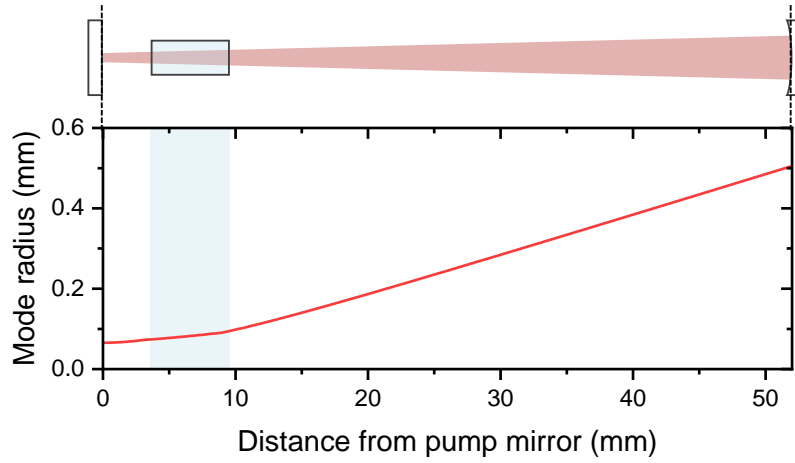
Figure 3.10: Beam diameter calculation in the plane-concave cavity.

3.5.2 Astigmatically compensated cavity

In this study, we used the conventional astigmatically compensated Z-shaped cavity for the mode-locking experiments. The schematic of the Z-shaped laser cavity is shown in Fig. 3.11.
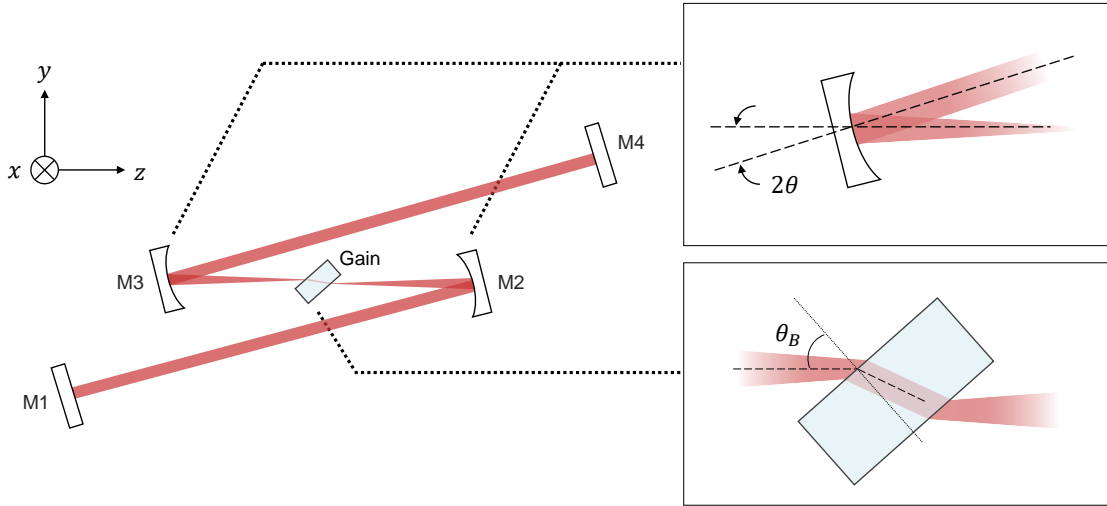
Figure 3.11: Schematic of Z-shaped cavity.

In this cavity, since the beam incidents to the gain medium and the spherical mirrors at some angles (cf. Fig. 3.11), these components exhibit astigmatism. For Brewster's cell with the thickness of t, the effective thickness for the sagittal and tangential plane can be written as follows [137]:

$$d_{\text{sag}} = \frac{t\sqrt{n^2 + 1}}{n^2}, \tag{3.39}$$

$$d_{\text{tan}} = \frac{t\sqrt{n^2 + 1}}{n^4}. \tag{3.40}$$

For the spherical mirrors with a focal length of f, the effective focal length can be written as follows:

$$f_{\text{sag}} = f \times \cos\theta, \tag{3.41}$$

$$f_{\text{tan}} = f/\cos\theta. \tag{3.42}$$

From Eq. (3.39) and (3.42), the difference of optical path between sagittal and tangential plane can be compensated each other by adjusting the incident angle *theta* to satisfy the following equation:

$$d_{\text{sag}} - d_{\text{tan}} \approx f_{\text{tan}} - f_{\text{sag}}. \tag{3.43}$$

To include the effect of astigmatism on the cavity design, we need to consider the ray-transfer matrices of the astigmatisms. I depicted the model of Brewster's cell (gain medium) as shown in Fig. 3.12 and 3.13.
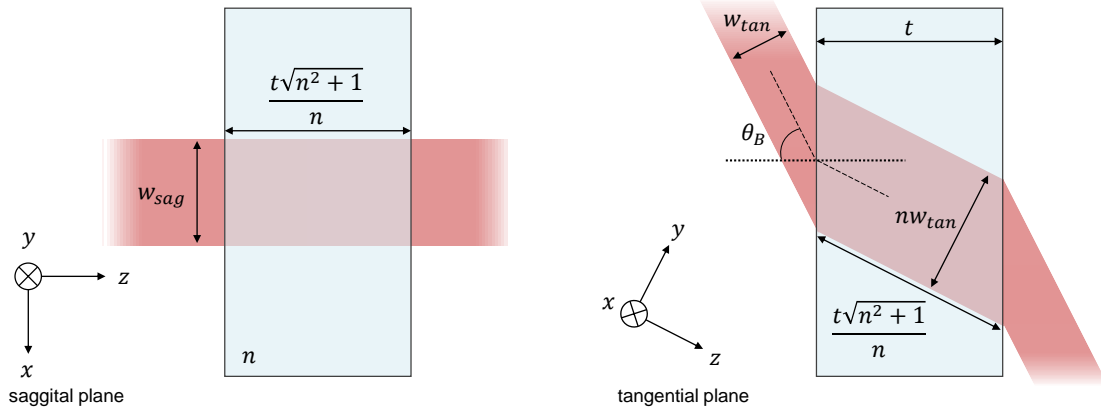
Figure 3.12: Astigmatisms in Brewster's cell. Variation of beam diameter.
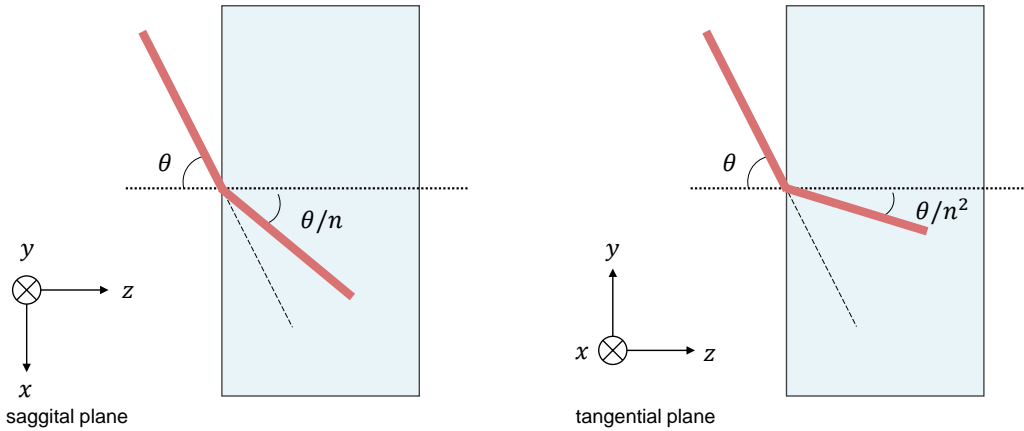
Figure 3.13: Astigmatisms in Brewster's cell. Variation of refractive angle.

For the saggital plane, when the beam incidents to the cell, the beam diameter is identical, but the angle against the optical axis is affected due to the difference of refractive index between air

and the Brewster's cell by a factor of $1/n$. Subsequently, the beam will propagate for the length of $t\sqrt{n^2+1}/n$. For the tangential plane, the incident beam diameter becomes n times larger, and the angle is also affected by a factor of $1/n^2$. Therefore, the the ray-transfer matrices at the Brewster's cell can be written as follows:

$$S_{\text{in,sag}} = \begin{bmatrix} 1 & 0 \\ 0 & 1/n \end{bmatrix}, \tag{3.44}$$

$$S_{\text{in,tan}} = \begin{bmatrix} n & 0 \\ 0 & 1/n^2 \end{bmatrix}, \tag{3.45}$$

$$S_{\text{out,sag}} = \begin{bmatrix} 1 & 0 \\ 0 & n \end{bmatrix}, \tag{3.46}$$

$$S_{\text{out,tan}} = \begin{bmatrix} 1/n & 0 \\ 0 & n^2 \end{bmatrix}. \tag{3.47}$$

Here, $S_{\text{in,sag}}, S_{\text{in,tag}}, S_{\text{out,sag}},$ and $S_{\text{out,tan}}$ are the matrices of the interface of Brewster's cell for incident and output for the sagittal and tangential plane, respectively. By calculating matrices for the propagation through the Brewster's cell using Eq. (3.44) - (3.47), we can obtain the matrices as:

$$S_{\text{sag}} = \begin{bmatrix} 1 & 0 \\ 0 & n \end{bmatrix} \begin{bmatrix} 1 & \dfrac{t\sqrt{n^2+1}}{n} \\ 0 & 1 \end{bmatrix} \begin{bmatrix} 1 & 0 \\ 0 & \dfrac{1}{n} \end{bmatrix} = \begin{bmatrix} 1 & \dfrac{t\sqrt{n^2+1}}{n^2} \\ 0 & 1 \end{bmatrix}, \tag{3.48}$$

$$S_{\text{tan}} = \begin{bmatrix} \dfrac{1}{n} & 0 \\ 0 & n^2 \end{bmatrix} \begin{bmatrix} 1 & \dfrac{t\sqrt{n^2+1}}{n} \\ 0 & 1 \end{bmatrix} \begin{bmatrix} n & 0 \\ 0 & \dfrac{1}{n^2} \end{bmatrix} = \begin{bmatrix} 1 & \dfrac{t\sqrt{n^2+1}}{n^4} \\ 0 & 1 \end{bmatrix}. \tag{3.49}$$

Now, comparing with Table 3.2, we can see the product of matrices [Eq. (3.48), (3.49)] regarding Brewster's cell is identical to the propagation with thickness $t\sqrt{n^2+1}/n^2$ and $t\sqrt{n^2+1}/n^4$. These results are well matched with Eq. (3.39) and (3.40). For the angle incident to the spherical mirrors, we can obtain the coefficients in the matrix just by replacing the modified focal length [Eq. (3.41), (3.42)] as follows:

$$M_{\text{sag}} = \begin{bmatrix} 1 & 0 \\ -\dfrac{1}{f \times \cos\theta} & 1 \end{bmatrix}, \tag{3.50}$$

$$M_{\text{tan}} = \begin{bmatrix} 1 & 0 \\ -\dfrac{1}{f/\cos\theta} & 1 \end{bmatrix}. \tag{3.51}$$

3.5.3   Nonlinear ABCD matrix calculation

Since KLM is achieved by the modulation of the spatial profile of the laser, we need to consider the Kerr-lens effect for the cavity design. Equation 3.18 can be described using the beam diameter w as below:

$$n' = n_0 + n_2 I = n_0 + n_2 \frac{P}{\pi w^2/4}. \tag{3.52}$$

Here, w^2 is replaced as $w_t \cdot w_s$. Based on Eq. (3.52) and the ray-transfer matrix for the gradient-index profile, the ABCD matrix of the Kerr medium can be described as follows [116]:

$$M_{\text{KL}} = \begin{bmatrix} \cos\gamma t & \frac{1}{\gamma}\sin\gamma t \\ -\gamma\sin\gamma t & \cos\gamma t \end{bmatrix}, \tag{3.53}$$

$$\gamma = \frac{1}{w^2}\sqrt{\frac{4n_0 P}{n'\pi}}. \tag{3.54}$$

More simply, the Kerr-lensing effect can be approximated as an effective focal length [138],

$$\frac{1}{f_{\text{KL}}} = \frac{4n_2 z}{\pi}\frac{P}{w^4}, \tag{3.55}$$

$$M_{\text{KL,a}} = \begin{bmatrix} 1 & l \\ -\frac{1}{f_{\text{KL}}(w)} & 1 \end{bmatrix}, \tag{3.56}$$

where l is the length of the Kerr medium. For the calculation of the beam radius with Kerr-effect, we utilized iterative numerical calculation according to the flowchart (cf. Fig.3.14 [139]) based on the model of lens relay shown in Fig. 3.15 which is equivalent to Fig. 3.11.
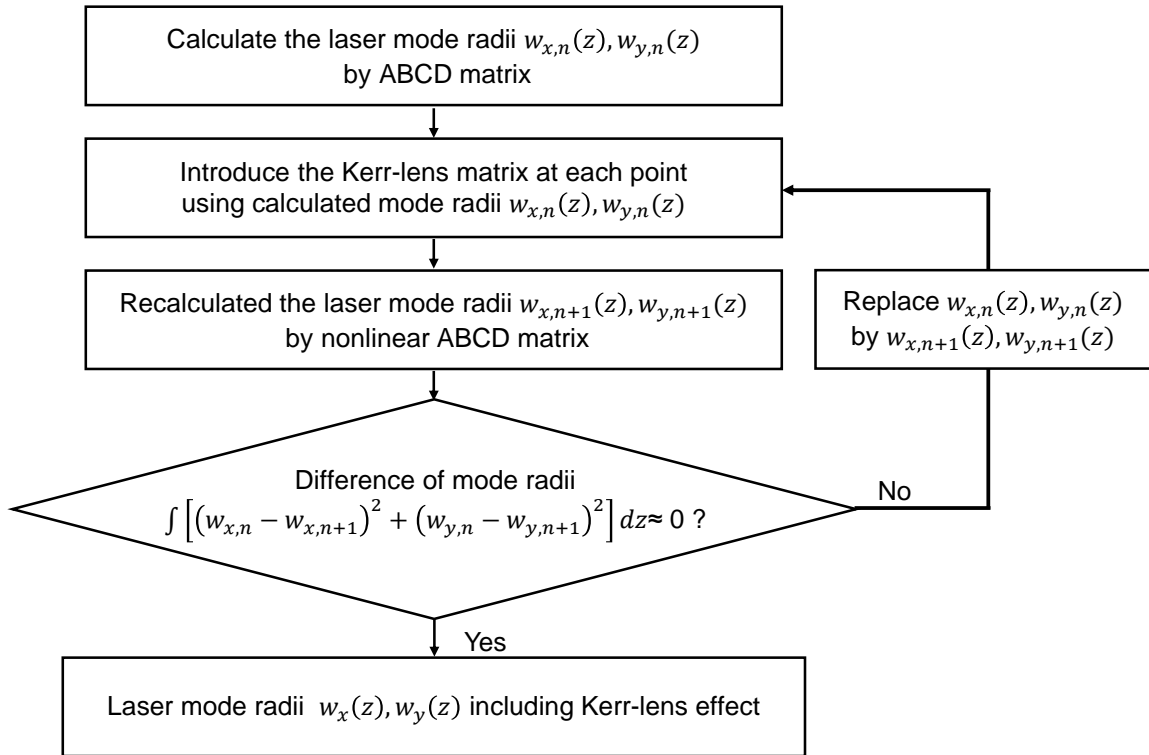
Figure 3.14: Flowchart of calculation for the laser mode with Kerr-effect.
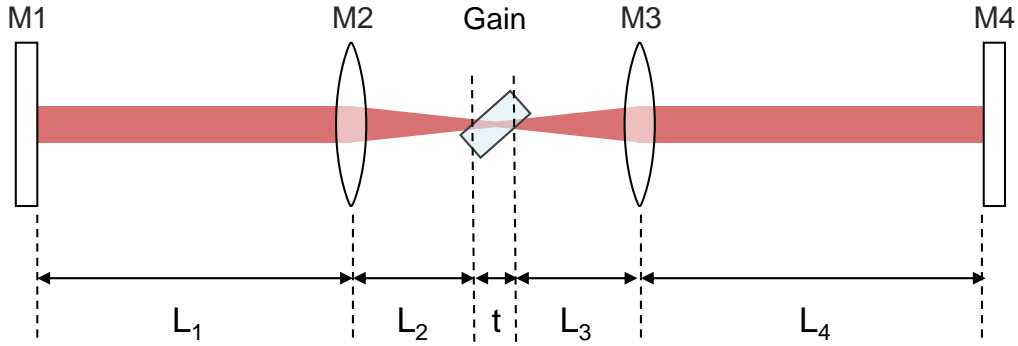
Figure 3.15: Model of lens relay equivalent to Z-shaped cavity for ABCD calculation.

To achieve soft aperture KLM, mode matching efficiency between pump and laser mode must increase for high intense light (pulsed light) to cause more efficient gain saturation with pulsed light. Thus, the magnitude of soft aperture effect can be defined by the ratio of the mode radii of weak light w_{CW} and high intense light w_{KLM}.

Figure 3.16 shows the 2D-map of the ratio of the mode radii for CW and pulsed light during gain material. L_2 and L_3 correspond to the distance between the concave mirror and gain crystal (cf, Fig. 3.15). For the calculation, cavity parameters shown in Table 3.3 were used. This figure indicates that the soft aperture effect becomes larger when the cavity condition is close to an unstable region for the sagittal and tangential plane, which is consistent with the empirically known fact. From Fig. 3.16, the point where the soft aperture effect is maximized is slightly different for the sagittal and tangential planes. At (a) shown in Fig. 3.16, the soft aperture effect is obtained in the sagittal plane, however, the soft aperture effect is *negative* in the tangential plane ($w_{\mathrm{CW}}/w_{\mathrm{KLM}} > 1$). We calculated the laser mode radii for CW and pulsed light using the cavity length which would lead to the largest soft aperture effect for both planes ((b) shown in Fig. 3.16).

Table 3.3: Parameters for the cavity mode calculation.

L_1	780 mm
L_4	760 mm
L_2 and L_3	varied
ROC of M2 and M3	100 mm
Incident angle into the M2 and M3	5.9°
Thickness of gain medium t	5 mm
Refractive index	1.9 (Tm:Lu$_2$O$_3$)
Intracavity peak power	1 MW

Figure 3.17 shows the calculated mode radii of CW and pulsed light. Owing to the Kerr-lensing effect, the laser mode of pulsed light is significantly changed from CW. During the gain crystal, the mode radii of pulsed light become smaller than that of CW light, resulting in better mode-matching with the pump beam.
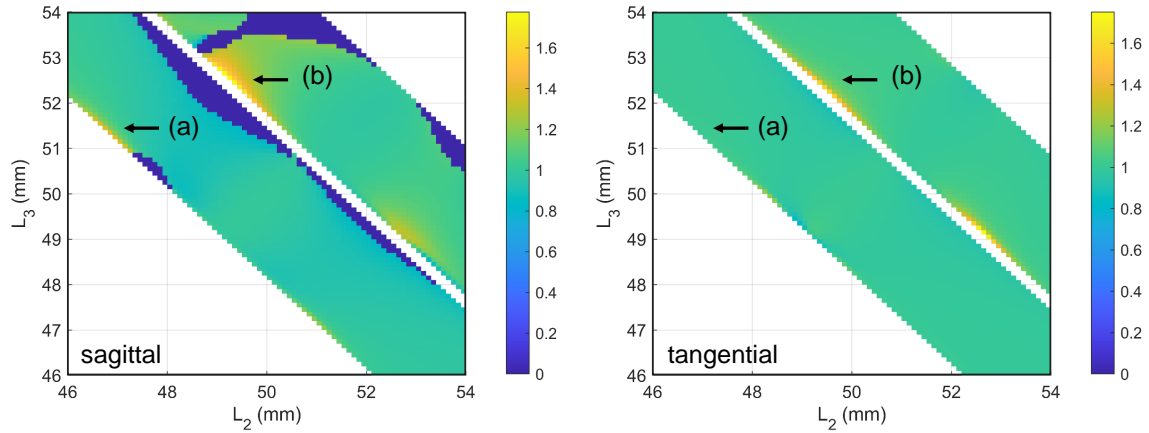
Figure 3.16: 2D-map of the soft aperture Kerr-lens effect.
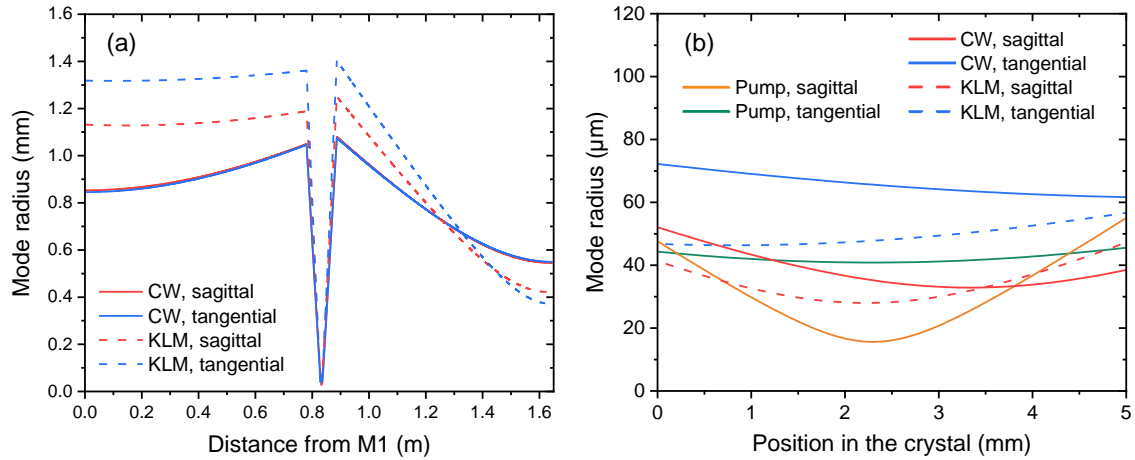
Figure 3.17: Calculated mode radius (a) in the KLM laser cavity (b) in the gain crystal.

In practice, after calculating the laser mode inside the cavity, we construct the cavity according to the parameters which satisfy the stable condition. For the initiation of mode-locking and large modulation depth, i.e. the largest shrinkage by Kerr-lensing effect, the cavity condition is optimized by varying the distance between M2 and M3 (L_2, L_3). The laser cavity defines the laser mode and the repetition rate. The stable region and the mode shrinking ratio are varied with the distance between each mirror as well as the cavity length. In addition, the Kerr-lensing effect is depending on the repetition rate as it affects intracavity peak power. Therefore, to start setting the cavity parameters is not so easy. If there is no requirement regarding laser specifications such as the repetition rate or the pulse energy, it is better to make a prototype following other papers or prior works, afterward, improve the laser cavity based on the experiments as well as the calculations for stable mode-locking (cf. Section 3.4).

Chapter 4

Combined gain media lasers based on Tm-doped sesquioxides

As described in Chapter 3, the achievable shortest pulse duration is mainly determined by the gain bandwidth. Combined gain media is a powerful technique to extend gain bandwidth overcoming the limitation of the single gain medium, which is desirable for broad wavelength tuning and ultrashort pulse generation. It is realized by using different gain media simultaneously in the same cavity. This idea was first proposed by A.Kaminskii in 1968 [140] and SESAM/Kerr-lens mode-locked Yb:Sc$_2$O$_3$/Yb:Y$_2$O$_3$ combined gain media lasers have been demonstrated in 2009 [141]. Tokurakawa *et al.* demonstrated the shortest pulse duration among Yb-based lasers at the time. Basically, this technique can be utilized for any gain materials. For short wavelength infrared (SWIR) lasers, an extremely broad tuning range was demonstrated in a combined gain Cr:ZnSe and Cr:CdSe laser [142]. In this study, we utilized this technique for 2 μm mode-locked Tm laser for the first time and achieved the shortest pulse duration of 41 fs among ever-reported Tm-based mode-locked lasers.

Section 4.1 deals with spectroscopic properties of Tm:Lu$_2$O$_3$ and Tm:Sc$_2$O$_3$ and a simulation of the effective gain to optimize parameters for the broadest gain bandwidth. In Section 4.2, continuous wave and tunable laser experiments are described, and in Section 4.3, Kerr-lens mode-locked experiments are described. Section 4.5 gives a discussion about the experimental results including the spectral broadening effect.
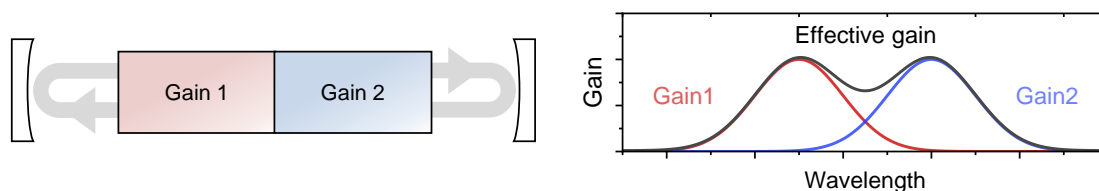
Figure 4.1: Schematic of the combined gain media. The red and blue curves in the right figure are the gain spectra of each of gain materials and the black curve is the effective gain of the combined gain media.

4.1   Tm:Lu$_2$O$_3$/Tm:Sc$_2$O$_3$ combined gain media

4.1.1   Effective gain of the combined gain media

The idea of the combined gain media laser is very simple: different gain materials are used simultaneously in the same cavity (shown in Fig. 4.1), so that the laser can benefit from the gain spectra of both materials. This can be considered as an intracavity passive beam combining in the spectral domain.

Figure 4.2 shows the absorption and emission cross section spectra of Tm:Lu$_2$O$_3$ and Tm:Sc$_2$O$_3$. Their emission bands spread exceeding 2000 nm, which are the longest wavelengths among Tm-doped laser materials due to large Stark splitting caused by the strong crystal field of sesquioxides. While Tm:Lu$_2$O$_3$ has emission peaks at ∼1950 nm and ∼2060 nm, Tm:Sc$_2$O$_3$ has peaks at longer wavelengths around sim1980 nm and ∼2120 nm owing to the stronger crystal field strength on the smaller Sc^{3+} site compared to larger Lu^{3+} site. As a result, the linear combined gain spectrum can be broad and flat.
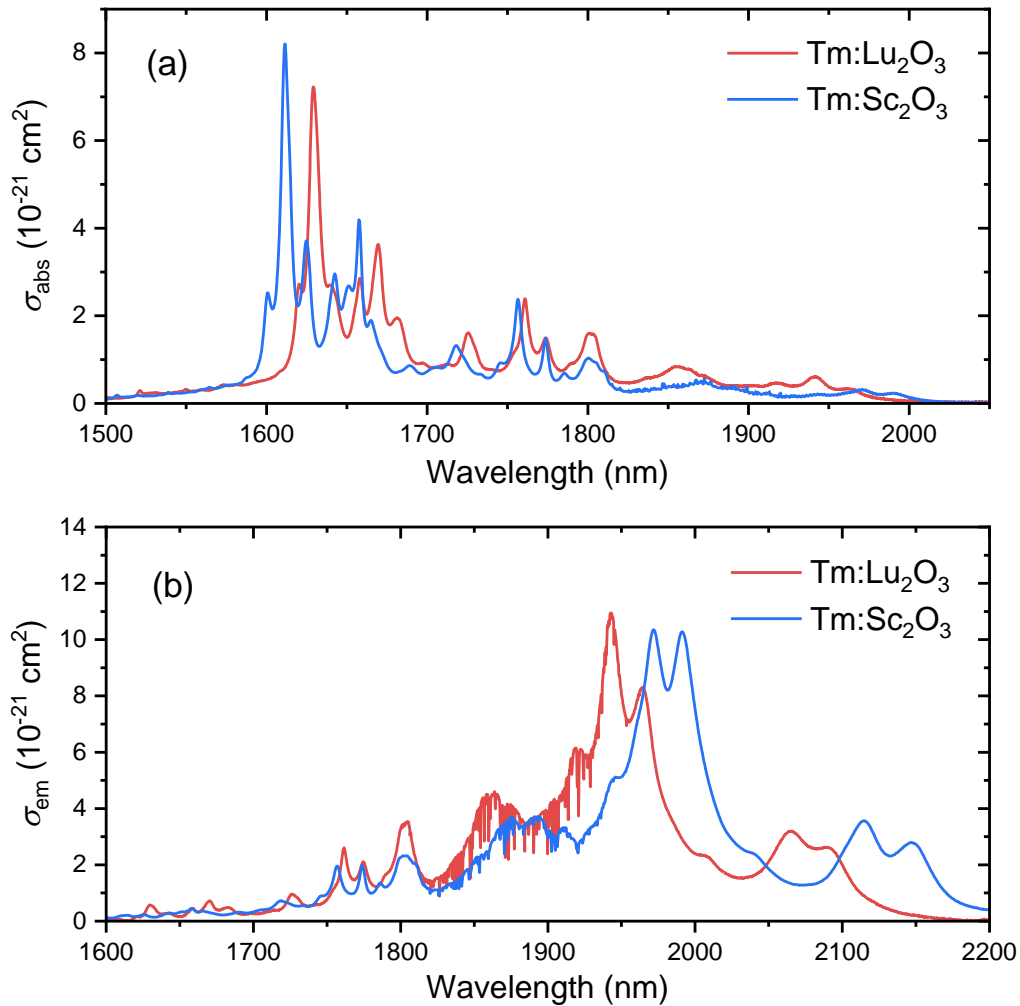
Figure 4.2: (a) Absorption and (b) emission cross sections of Tm:Sc$_2$O$_3$ and Tm:Lu$_2$O$_3$.

The effective gain cross section σ_{eff} resulting from the use of Tm:Lu$_2$O$_3$ and Tm:Sc$_2$O$_3$ can be described as:

$$\sigma_{\text{eff}} = \alpha[\beta_1\sigma_{\text{em},1} - (1 - \beta_1)\sigma_{\text{abs},2}] + (1 - \alpha)[\beta_2\sigma_{\text{em},2} - (1 - \beta_2)\sigma_{\text{abs},2}], \qquad (4.1)$$

where $\sigma_{\text{em},1}, \sigma_{\text{em},2}, \sigma_{\text{abs},1}, \sigma_{\text{abs},2}$, are the emission and absorption cross sections of Tm:Lu$_2$O$_3$ and Tm:Sc$_2$O$_3$, respectively. β_1 and β_2 indicate the population inversion, the fraction of populated ion density and the total ion density, for each gain medium. α indicates the ratio of the Tm^{3+}-ions in the Tm:Lu$_2$O$_3$ against the total amount of Tm^{3+} ions in both gain media. α is resulted from the parameters of both gain media, thus it can be tuned by the doping concentration and/or the thickness of the gain materials. The inversion parameter β is mainly determined by the pump intensity. Figure 4.3 shows the example of calculation results with different α and β. The effective gain σ_{eff} shape and bandwidth strongly depend on the ratios α and β, thus the broader gain bandwidth and a flat and smooth profile can be obtained by a proper choice of all parameters.
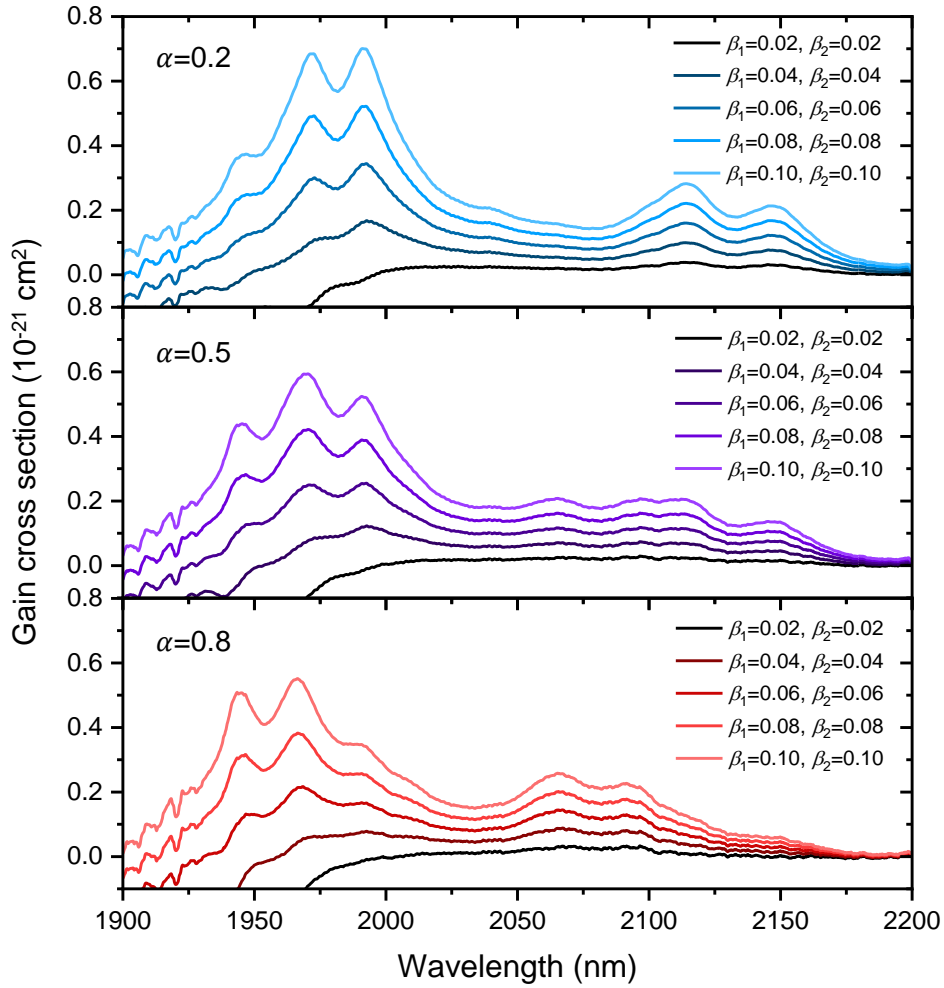
Figure 4.3: Simulated effective gain of combined gain media with different α and β.

4.1.2   Gain saturation in the combined gain media laser

When Tm:Lu$_2$O$_3$ and Tm:Sc$_2$O$_3$ are used in the same cavity, each gain will be independently saturated depending on the operating wavelengths. Therefore, the combined gain media can be regarded as *artificial* inhomogeneously broadened gain material, although Tm:Lu$_2$O$_3$ and Tm:Sc$_2$O$_3$ are homogeneously broadened materials. The saturation gain of homogeneously broadened gain material considering the laser wavelength can be described as follows:

$$g_s(\lambda) = \frac{g_0(\lambda)}{1 + \int I(\lambda)/I_s(\lambda)d\lambda}, \qquad (4.2)$$

where g_s is saturation gain, g_0 is small-signal gain, $I(\lambda)$ and $I_s(\lambda)$ are laser intensity and saturation intensity, respectively. The saturation intensity for a three-level laser system $I_s(\lambda)$ [66] is

$$I_s = \frac{h\nu[W_p + (1/\tau_{\mathrm{f}})]}{\sigma[1 + (g_2/g_1)]}, \qquad (4.3)$$

where $h\nu$ is photon energy, W_p is the pump rate, τ_f is the fluorescence lifetime of upper laser level, σ is emission cross section, and g_1, g_2 are the degeneracy of the lower and upper laser level. The saturation gain of combined gain media can be expressed as follows:

$$\begin{aligned} g_{\mathrm{s,combined}} &= g_{s,1} + g_{s,2} \\ &= \frac{g_{0,1}(\lambda)}{1 + \int I(\lambda)/I_{s,1}(\lambda)d\lambda} + \frac{g_{0,2}(\lambda)}{1 + \int I(\lambda)/I_{s,2}(\lambda)d\lambda}, \end{aligned} \qquad (4.4)$$

where, $g_{s,1}, g_{s,2}, g_{0,1}, g_{0,2}$, and $I_{s,1}, I_{s,2}$ are saturation gain, small-signal gain, and saturation intensity of each gain material, respectively. From Eq. (4.4), the strength of gain saturation in each gain material is defined by $\int I(\lambda)/I_{s,1}(\lambda)d\lambda$ and $\int I(\lambda)/I_{s,2}(\lambda)d\lambda$.
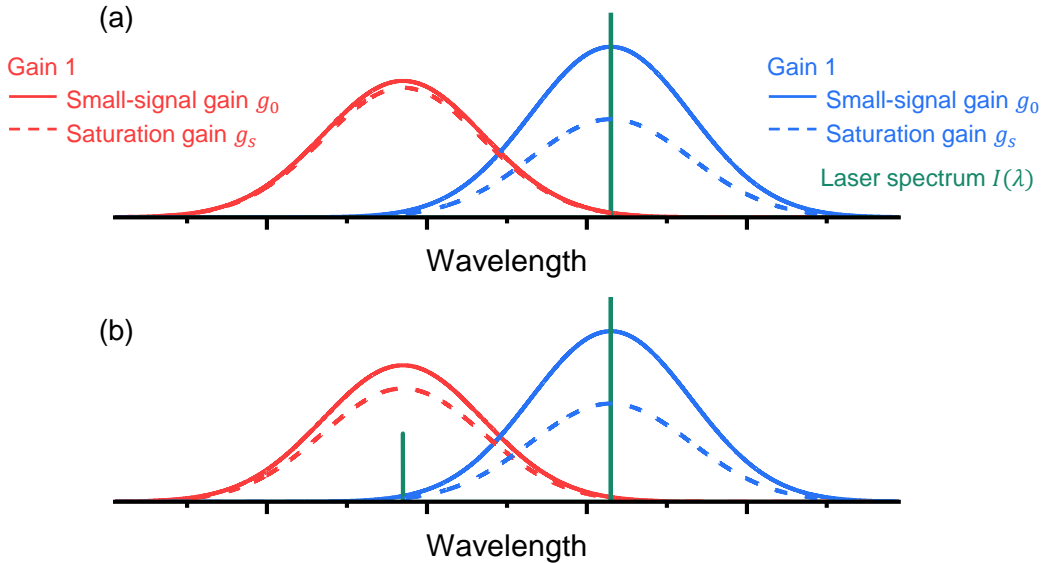
Figure 4.4: Gain saturation in the combined gain media CW laser with (a) single-wavelength and (b) dual-wavelengths.

Figure 4.4 shows the example of gain saturation in the combined gain media in CW laser regime. If the small-signal gain of Gain2 is larger than that of Gain1, lasing will start at the wavelength corresponding to the peak wavelength of Gain2 above laser threshold. At this time, the gain saturation efficiently occurs in Gain1, but Gain1 is not saturated since the laser wavelength is out of gain band of Gain1. By further increasing pumping power and inversion population in Gain1 reaches lasing threshold, lasing will occur at the peak wavelength of Gain1 in addition to Gain2 (cf. Fig. 4.4).

In the case of pulsed laser operation, the laser spectrum is broadened by mode-locking. Figure 4.5 shows the case of gain saturation with narrow laser spectral at the peak wavelength of Gain2. As the laser spectrum is located at longer wavelengths, gain saturation strongly occurs in Gain2, and weakly occurs in gain1, resulting in the larger saturation gain for Gain1 and the laser spectrum can be broadened toward shorter wavelengths. When the mode-locked spectrum is sufficiently broadened, gain saturation will equally occur in both gain materials. The effective saturation gain will be the broadest and the profile of the saturation gain will be identical to the small signal gain if the saturation intensity of both materials is the almost same.
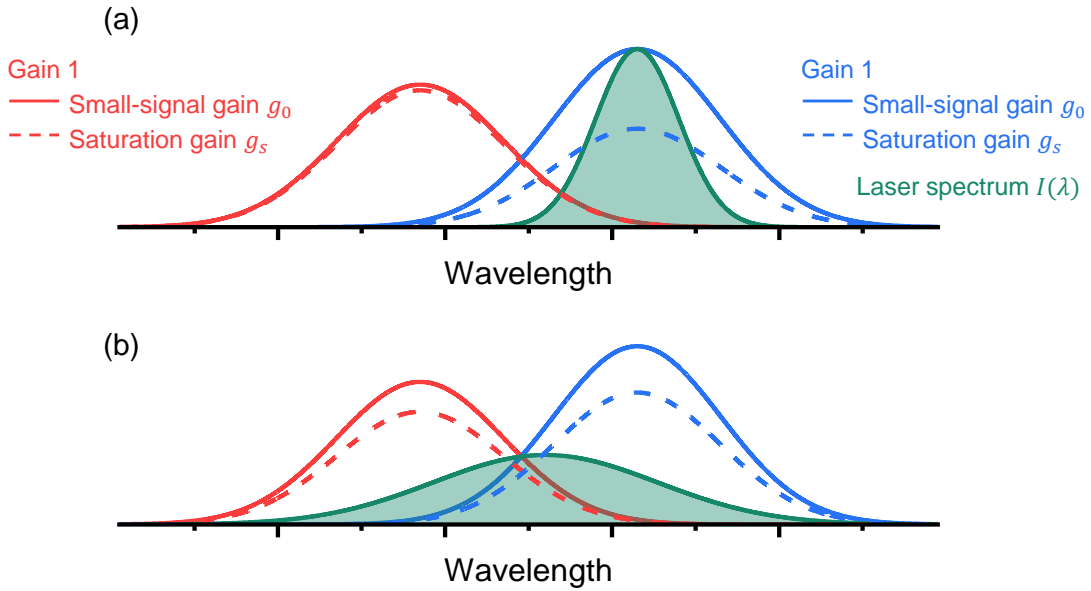
Figure 4.5: Gain saturation in the combined gain media ML laser with (a) narrow and (b) broad optical spectrum.

This inhomogeneously gain saturation is unique behavior in the combined gain media laser. Even if the conventional homogeneously broadened material had the same effective small-signal gain spectrum as that of the combined gain media in Fig.4.5, spectral broadening toward shorter wavelengths is difficult since the saturation gain at shorter wavelengths is reduced owing to homogeneously gain saturation. Therefore, combined gain media is advantageous for broader gain bandwidth as well as spectral broadening in the mode-locked operation. It should be noted, when we choose the gain materials to use as combined gain media, the saturation intensity of each material should be considered in addition to the gain band to fully use the gain band of both materials.

4.2 CW and tunable operation of combined gain laser

4.2.1 Experimental setup for CW combined gain media laser

Figure 4.6 shows the experimental setup of the combined gain media laser. we used an astigmatism-compensated Z-shaped cavity composed of two concave mirrors (R=100 mm, R>99.9% at 1850-2200 nm), an end mirror, and a wedged output coupler. Wavelength tunability was measured by inserting a prism in front of the end mirror and achieved by the angular dispersion of the prism. As gain media, we utilized two sets of combined gain media, a 3.7-mm thick 1.0 at.%-doping $Tm:Sc_2O_3$ crystal and two different $Tm:Lu_2O_3$ ceramics, which all remain uncoated. The properties of gain media are shown in Table 4.1. The $Tm:Sc_2O_3$ and a $Tm:Lu_2O_3$ were physically contacted and held in the same holder as shown in Fig. 4.7. The gain media were placed in the focus between the two concave mirrors at Brewster's angle. It should be noted that since Lu_2O_3 and Sc_2O_3 have similar refractive indices of $\approx$1.9, Brewster's angles of both materials are $\approx$63°. Therefore, we can utilize this configuration in this case.

Table 4.1: Properties of the $Tm:Lu_2O_3$ and the $Tm:Sc_2O_3$.

	doping concentration (%)	thickness (mm)	pump absorption @ 1611 nm (%)
$Tm:Lu_2O_3$ -1	1.5	4.0	18
$Tm:Lu_2O_3$ -2	4.0	4.0	40
$Tm:Sc_2O_3$	1.0	3.7	68
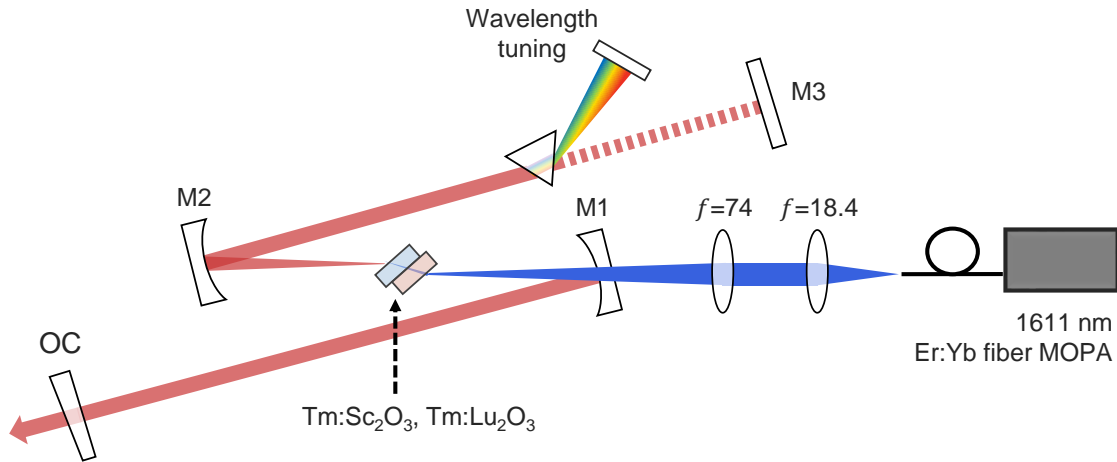
Figure 4.6: Experimental setup of the combined gain media laser (M1, M2: curved mirrors (R=100 mm), M3: a flat high reflective mirror, OC: a wedged output coupler). For CW laser operation, a dashed beam path was used.
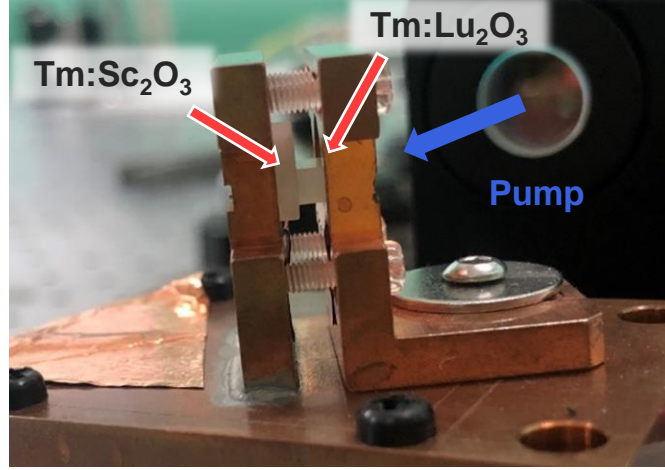
Figure 4.7: Photograph of the combined gain media in the laser cavity.

As a pump source, we used a home-build 1611 nm Er:Yb-doped all fiber master-oscillator power amplifier (MOPA) which has a linear polarized output with a maximum output power of 3 W [42]. At the pumping wavelength, $Tm:Lu_2O_3$ has a lower absorption cross section than $Tm:Sc_2O_3$ (cf. Fig. 4.2(a) and Table 4.1). In order to balance pump absorption for both gain media, the $Tm:Lu_2O_3$ was placed closer to the pump source and the $Tm:Sc_2O_3$ at the opposite side, so that the $Tm:Sc_2O_3$ was pumped by the residual pump beam transmitting the $Tm:Lu_2O_3$. The estimated beam diameters of the pump and the cavity fundamental mode at the focal point were 43×43 µm^2 and 66×65 µm^2, respectively.
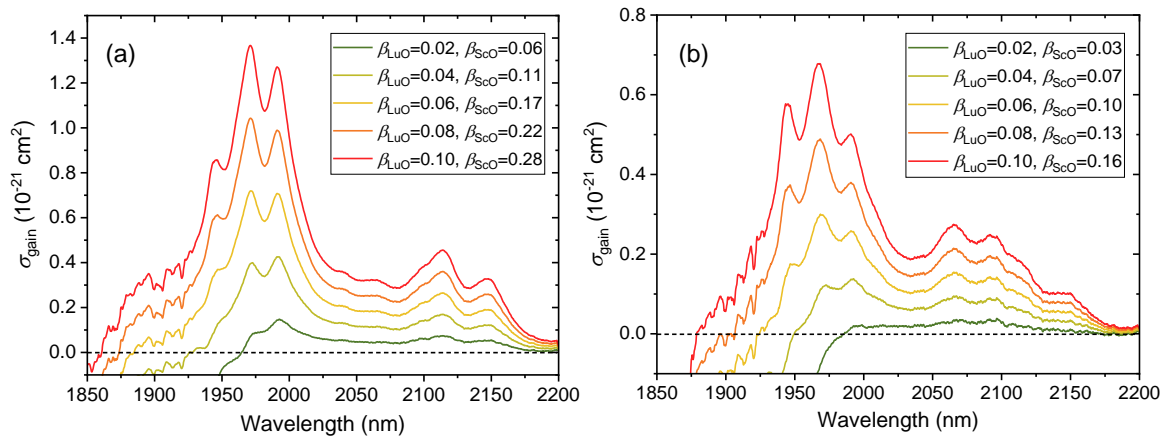
Figure 4.8: Calculated effective gain cross sections of (a) the 4 mm-thick Tm(4.0%):Lu_2O_3 and the 3.7 mm-thick Tm(1.0%):Sc_2O_3, (b) the 4 mm-thick Tm(1.5%):Lu_2O_3 and the 3.7 mm-thick Tm(1.0%):Sc_2O_3 combined gain. Note that the ratio between β_{LuO} and β_{ScO} must remain constant as both media are pumped by the same pump source in this configuration.

The calculated effective gain spectra of two different combinations under these conditions were shown in Fig. 4.8. In Fig. 4.8(a), since the doping concentration of the Tm:Lu$_2$O$_3$ -1 is low, the total contribution of Tm:Lu$_2$O$_3$ is smaller than Tm:Sc$_2$O$_3$. On the contrary, in Fig. 4.8(b), the higher doping concentration of the Tm:Lu$_2$O$_3$ -2 makes the larger contribution of Tm:Lu$_2$O$_3$. In addition, due to the smaller absorbed pump power of the Tm:Sc$_2$O$_3$, the inversion level of the Tm:Sc$_2$O$_3$ β_2 is significantly smaller than Tm:Lu$_2$O$_3$, thus the gain at shorter wavelengths is suppressed in (b) compared with (a).

4.2.2   CW laser operation

The CW laser experiments were performed using different OCs with transmittance of 1.0%, 1.5 %, 3.0%, 5.0%, 9.0% and 10%. Figure 4.9 shows the laser output characteristics using the 4 mm-thick Tm(1.5 at.%):Lu$_2$O$_3$ ceramic and the 3.7 mm-thick Tm(1.0 at.%):Sc$_2$O$_3$ crystal. With the increase of OC transmittance, the slope efficiency increased. The highest slope efficiency of 60% and maximum output power of 800 mW were obtained using the 9.0% OC. However, for the 10% OC, the slope efficiency decreased to 57%. The Stokes efficiency η_{stokes} is $\approx$ 76%, thus highly efficient laser operation was achieved. The laser wavelengths were 2120 nm for lower transmittance OCs and 1980/1990 nm for higher OCs. This is typical for the quasi-three level lasers, as the gain at shorter wavelengths increases at higher inversion levels.
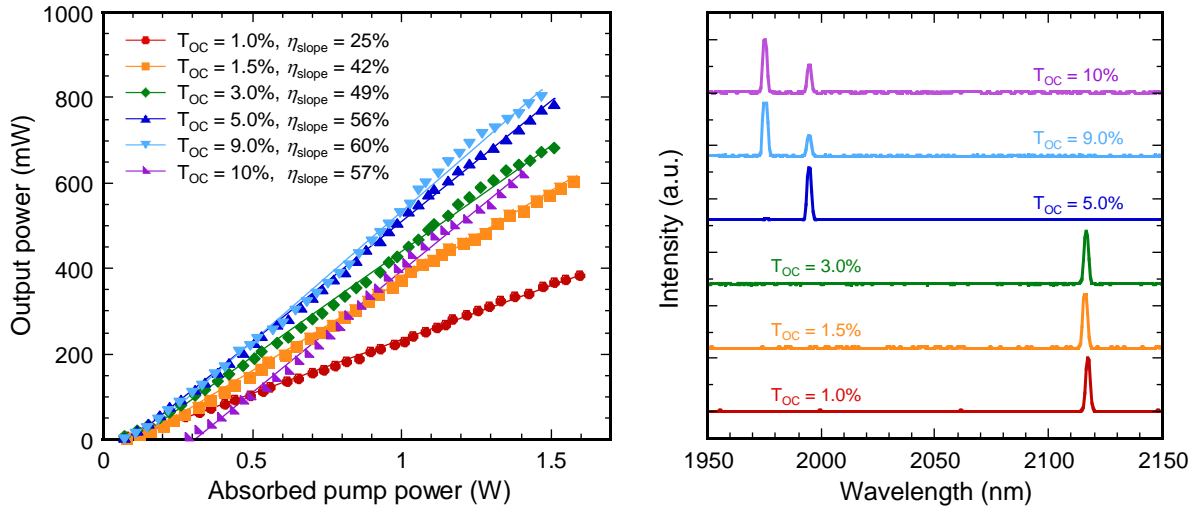
Figure 4.9: (a) Laser output power as a function of absorbed pump power of the combined gain Tm(1.5 at.%):Lu$_2$O$_3$ and Tm(1.0 at.%):Sc$_2$O$_3$ laser and (b) free running spectra.

Figure 4.10 shows the CW laser result using the 4 mm-thick Tm(4.0 at.%):Lu$_2$O$_3$ ceramic and the 3.7 mm-thick Tm(1.0 at.%):Sc$_2$O$_3$ crystal. In this case, the highest slope efficiency of 57% was obtained using the 5.0% OC and the slope efficiency already dropped for the 9.0% OC. This is generally explained by the ETU increased at high inversion levels [61]. Especially for higher doping levels, the closer average distance between excited ions features detrimental energy transfer processes, resulting in a low laser performance for the combination of the higher doped Tm:Lu$_2$O$_3$

and the $Tm:Sc_2O_3$ with the higher transmittance OCs, compared with the previous experiment. The laser wavelength was almost the same as in the previous experiment; however, the dual-wavelength operation was more often observed in this experiment as the gain of $Tm:Lu_2O_3$ increased with a higher doping level.
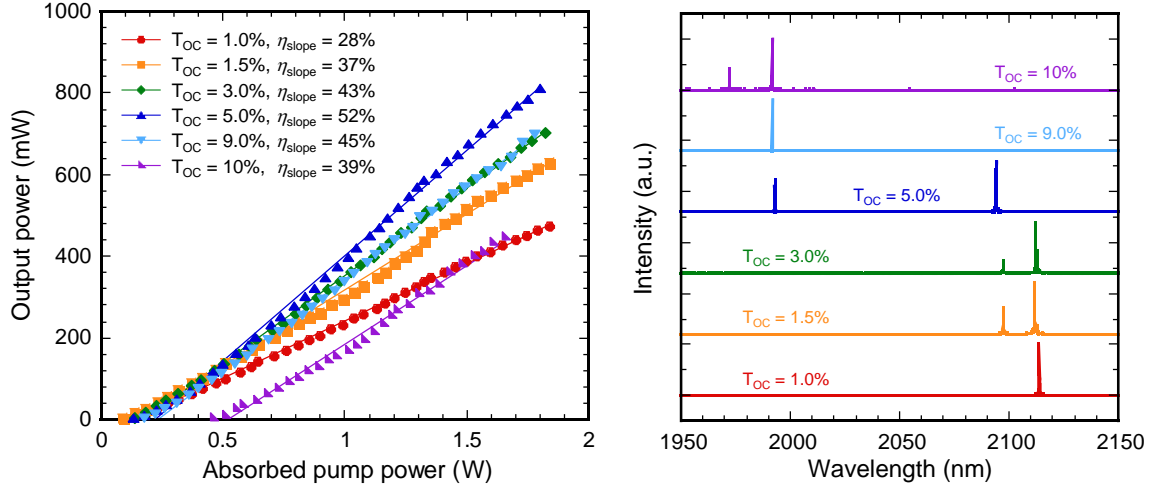
Figure 4.10: (a) Laser output power as a function of absorbed pump power of the combined gain $Tm(4.0 \text{ at.}\%):Lu_2O_3$ and $Tm(1.0 \text{ at.}\%):Sc_2O_3$ laser and (b) free running spectra.

4.2.3 Wavelength tunablility

Wavelength tunability was measured by inserting a prism (fused silica) as a tuning element in the cavity. Figure 4.11 shows the results of wavelength tuning for each combination of the gain media. For the combination of the $Tm(1.5 \text{ at.}\%):Lu_2O_3$ and the $Tm(1.0 \text{ at.}\%):Sc_2O_3$, wavelength tuning from 1890 to 2243 nm was obtained using a 1.0% OC. By replacing a OC to a 0.5% one, the wavelength could be tuned from 1881 to 2217 nm. For the 0.5% OC, the longer wavelength edge was limited by the specific coating of the OC. For both OCs, broad and flat tuning curves were obtained. For the combination of the $Tm(4.0 \text{ at.}\%):Lu_2O_3$ and the $Tm(1.0 \text{ at.}\%):Sc_2O_3$, wavelength tuning from 1962 to 2252 nm and from 1962 to 2228 nm was obtained using the 1.0% OC and the 0.5% OC, respectively. For this case, the longer wavelength edge was almost the same as in the previous experiment. However, the shorter wavelength edge was limited by the increased loss caused by the reabsorption in the $Tm:Sc_2O_3$ compared with the previous experiment. As the absorbed pump power in the $Tm:Lu_2O_3$ increased owing to higher doping concentration, the inversion level for the $Tm:Sc_2O_3$ decreased and the ratio of ground state absorption (GSA) increased. These results reflect the feature of the gain spectra (cf. Fig. 4.8). The measured tuning range was extended beyond 2000 nm where no strong water vapor absorption exists and a maximum tuning range of 353 nm was achieved. This should support ultrashort pulse generation in mode-locking experiments.
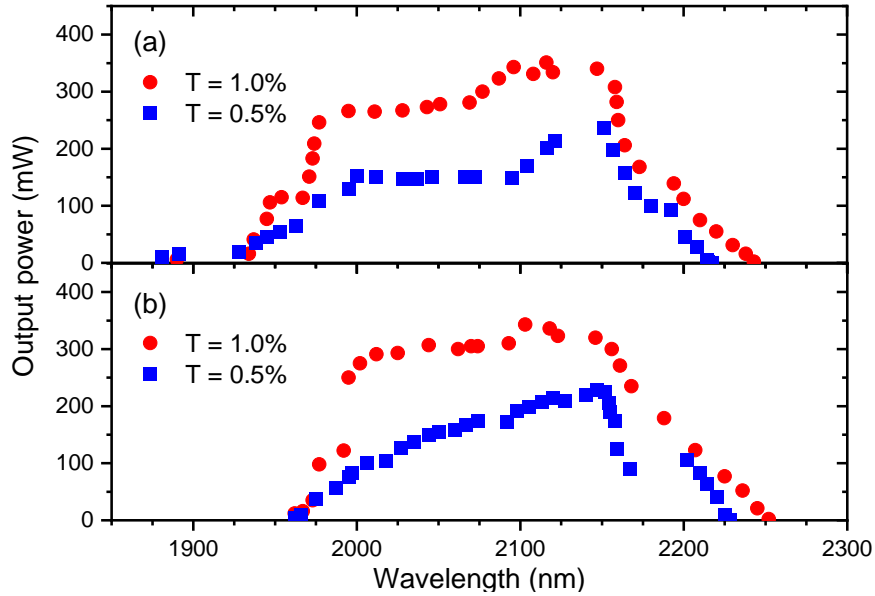
Figure 4.11: Wavelength tunability of the combined gain (a) $Tm(1.5$ at.%$):Lu_2O_3$ and $Tm(1.0$ at.%$):Sc_2O_3$ laser and (b) $Tm(1.5$ at.%$):Lu_2O_3$ and $Tm(1.0$ at.%$):Sc_2O_3$ laser with 1.0% and 0.5% OC under 2.1 W pumping.

4.3 Kerr-lens mode-locked combined gain laser

4.3.1 Experimental setup for KLM combined gain media laser

KLM experiments were performed with the same cavity configuration as the CW laser experiment (cf. Fig. 4.6), but the cavity mirrors were replaced by the chirped mirrors for dispersion compensation. Table 4.2 shows the list of the combinations of gain media and cavity dispersion.

Table 4.2: Combination of gain media and the cavity GDD for KLM experiments.

Gain media	OC (%)	Total GDD (fs^2)
4.0 mm $Tm(1.5$ at.%$):Lu_2O_3$+3.7 mm $Tm(1.0$ at.%$):Sc_2O_3$	1.0	-780
	0.5	-780
4.0 mm $Tm(4.0$ at.%$):Lu_2O_3$+3.7 mm $Tm(1.0$ at.%$):Sc_2O_3$	3.0	-1580
	3.0	-2560
	1.0	-880
	0.5	-880

4.3.2 KLM $Tm(1.5$ at.%$):Lu_2O_3$/$Tm(1.0$ at.%$):Sc_2O_3$ laser

First, we used the 4 mm-thick $Tm(1.5$ %$):Lu_2O_3$ and the 3.7 mm-thick $Tm(1.0$ at.%$):Sc_2O_3$ as gain media. KLM operation was initiated by moving the mirror M2 (see Fig. 4.6). Using a 1.0% OC, KLM was obtained at an absorbed output power of 0.79 W. Figure 4.12 shows the output characteristics of the KLM laser. When the ML operation started, the average output power increased. This is

typical behavior for KLM lasers because the cavity condition is optimized for high intense light (pulsed light) in the KLM, resulting in higher output powers.

Figure 4.12: (a) Average output power and (b) optical spectrum (grey: measured spectrum, red: sech^2 fit) of the combined gain Tm(1.5 at.%):Lu$_2$O$_3$ and Tm(1.0 at.%):Sc$_2$O$_3$ laser using the 1.0% OC. (c) SHG intensity autocorrelation trace after compression (red circle: measured data, black: sech^2 fit).

In this configuration, pulses as short as 71 fs were obtained directly after the OC with a maximum output power of 105 mW. After compression using a 1 mm-thick Si plate (GDD$\sim$+770 fs^2), the pulse duration of 63 fs was determined by SHG intensity autocorrelation as shown in Fig. 4.12(c). A pulse repetition rate was 93.3 MHz, thus the corresponding pulse energy and peak power were 1.13 nJ and 17.8 kW, respectively. The spectral bandwidth was 74 nm at a center wavelength of 2097 nm. By further increasing pump power, the transition to the multi-pulse operation was observed and the pulse duration was broadened.

Figure 4.13: (a) Average output power and (b) optical spectrum (grey: measured spectrum, red: sech^2 fit) of the combined gain Tm(1.5 at.%):Lu$_2$O$_3$ and Tm(1.0 at.%):Sc$_2$O$_3$ laser using the 0.5% OC. (c) SHG intensity autocorrelation trace after compression (red circle: measured data, black: sech^2 fit).

We replaced the OC with 0.5% one to further shorten the pulse duration. In this case, KLM could be initiated at an absorbed pump power of 0.67 W. Figure 4.13 shows the output characteristics. At a maximum average output power of 52 mW, pulses as short as 60 fs were obtained after compression. the spectral bandwidth of 78 nm was obtained at a center wavelength of 2097 nm. Therefore, the

time-bandwidth product was ≈0.32, indicating transform-limited pulses. The pulse energy and the peak power were 0.58 nJ and 9.3 kW, respectively.
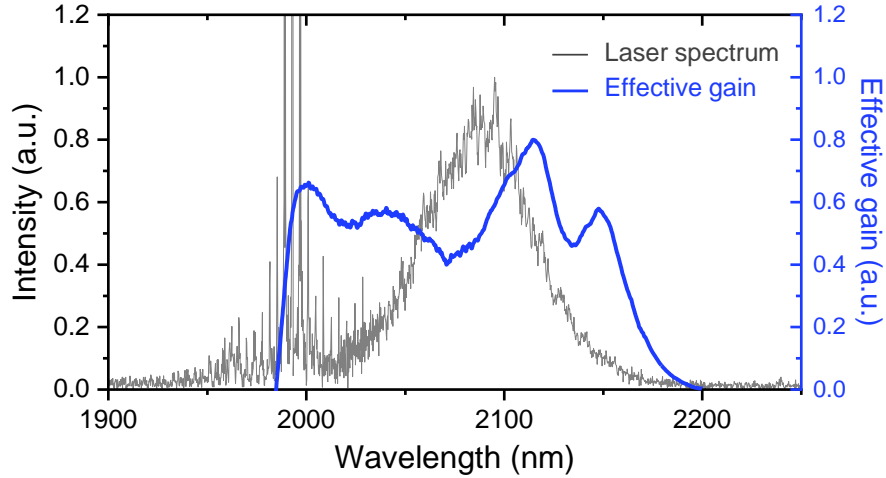
Figure 4.14: Optical spectrum of the KLM Tm(1.5 at.%):Lu_2O_3 and Tm(1.0 at.%):Sc_2O_3 laser with CW component (grey) and effective gain (blue).

In this case, the shortest pulse duration and mode-locked operation were limited by the appearance of the CW component around 1980 nm as shown in Fig.4.14. The wavelength of the CW component corresponded to the peak of the effective gain. As described in Chapter 3, ML is sustained by the balance between spectral broadening effect by SPM and SA effect to suppress the CW operation. However, if the SA effect can not fully support spectral broadening, a transition to the multi-pulse operation or appearance of the CW component will occur. Intuitively, it can be considered that the laser oscillating mode will change to be more "comfortable" condition for gain saturation. In this case, the CW component appeared, and the power density of the CW component only increased by further increasing pump power afterward.

4.3.3 KLM Tm(4.0 at.%):Lu_2O_3/Tm(1.0 at.%):Sc_2O_3 laser

Next, to overcome the limitation in the previous experiment, we used the Tm(4.0 at.%):Lu_2O_3 and the Tm(1.0 at.%):Sc_2O_3 for the second experiment. Using the higher doped Tm:Lu_2O_3, the gain peaks at shorter wavelengths were suppressed by increased absorption loss in the Tm:Sc_2O_3, and a flatter gain profile was obtained (cf. Fig. 4.8). Thus, the broadband mode-locked operation without the appearance of CW component would be expected.

First, we used a 3.0% OC and increased cavity GDD. KLM was obtained at an absorbed pump power of 1.4 W. By increasing the pump power, a maximum average output power of 316 mW at an absorbed pump power of 1.8 W (cf. Fig. 4.15(a)). The optical spectrum of the mode-locked laser is shown in Fig. 4.15(b). The spectral bandwidth was 64 nm at the center wavelength around 2090 nm. The pulse duration after compression was 73 fs as shown in Fig. 4.15(c). The repetition rate was 93.2 MHz and the calculated pulse energy and peak power were 3.4 nJ and 46.4 kW, respectively.
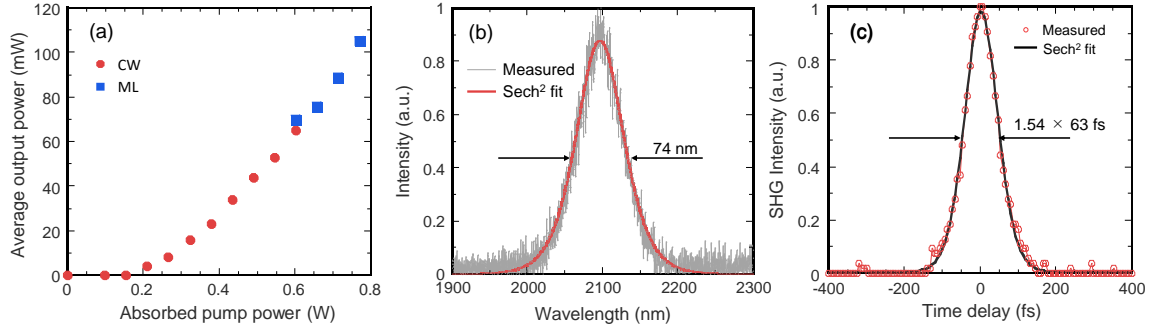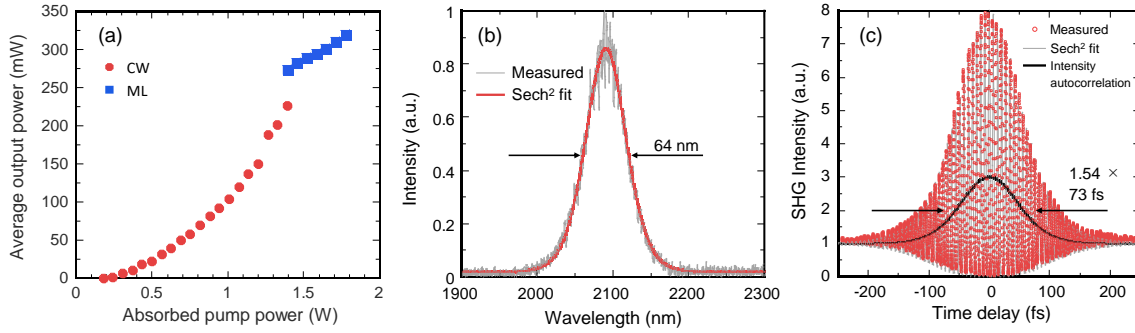
Figure 4.15: (a) Average output power and (b) optical spectrum (grey: measured spectrum, red: sech^2 fit) of the combined gain Tm(4.0 at.%):Lu$_2$O$_3$ and Tm(1.0 at.%):Sc$_2$O$_3$ laser using the 3.0% OC. (c) SHG interferometric and intensity autocorrelation traces after compression (red circle: measured data, grey: sech^2 fit, black: intensity autocorrelation).

Using the same transmittance OC, we further increased cavity GDD to -2560 fs^2 by inserting prism pair in the cavity. As a result, we obtained mode-locked laser operation with higher output powers (cf. Fig.4.16). A maximum average output power of 538 mW was achieved at an absorbed pump power of 2.7 W with a longer pulse duration of 118 fs. The calculated pulse energy and peak power were 5.8 nJ and 49 kW, respectively. The increased pulse energy compared with the prior experiment can be explained by Eq. (3.24). According to Eq. (3.24), large cavity dispersion D_2 leads to large pulse energy.
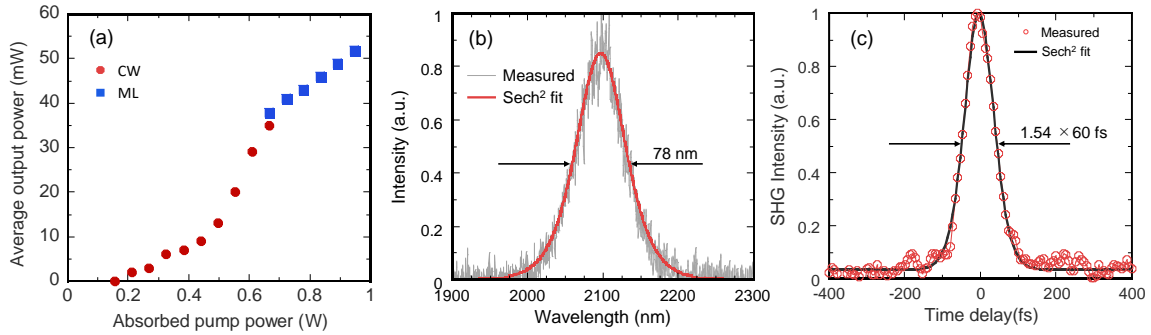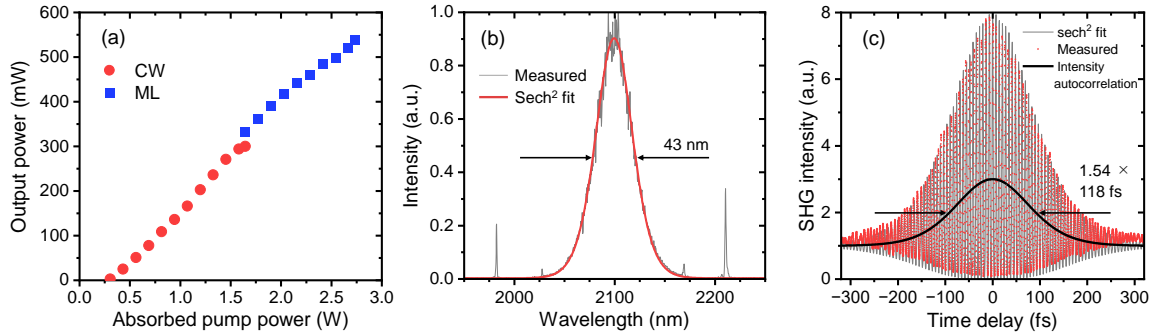

Figure 4.16: (a) Average output power and (b) optical spectrum (grey: measured spectrum, red: sech^2 fit) of the combined gain Tm(4.0 at.%):Lu$_2$O$_3$ and Tm(1.0 at.%):Sc$_2$O$_3$ laser using the 3.0% OC with increased cavity GDD. (c) SHG interferometric and intensity autocorrelation traces after compression (red circle: measured data, grey: sech^2 fit, black: intensity autocorrelation).

For a shorter pulse duration, we replaced the OC with 1.0% OC and reduced the cavity dispersion to -880 fs^2. The ML laser characteristics are shown in Fig. 4.17. In this case, KLM is obtained at an absorbed pump power of 1.3 W. The threshold of ML is lower than the previous experiment because of the higher intracavity power owing to the lower transmittance of OC. A maximum average output power of 81 mW was obtained at an absorbed pump power of 1.6 W. As expected, the pulse duration directly after the OC was reduced to 67 fs at a repetition rate of 93.2 MHz. After an

external compression by a 3 mm-thick ZnSe window (GDD$\sim$+495 fs^2), pulses as short as 52 fs were obtained as shown in Fig. 4.17(c). The spectral bandwidth was 89 nm centered around 2095nm (Fig. 4.17(b)). The broadened spectrum was obtained by the combination of the large SPM and the broad gain spectra of the combined gain media. The time-bandwidth product was 0.315, thus the chirp free pulses were obtained by the proper compression.
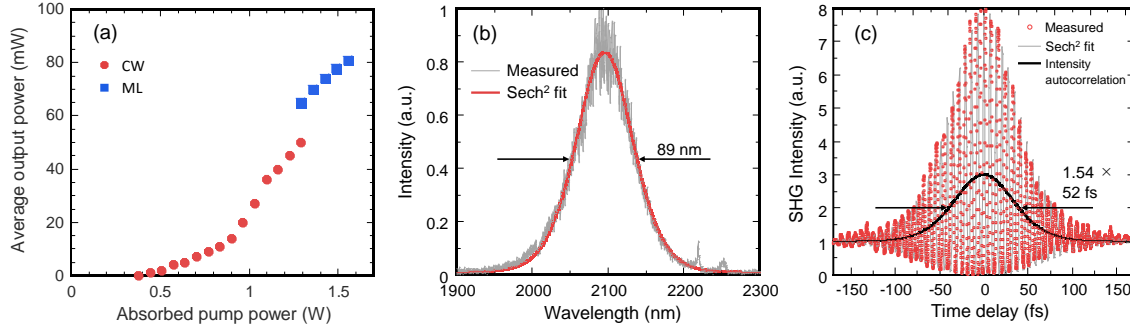
Figure 4.17: (a) Average output power and (b) optical spectrum (grey: measured spectrum, red: sech^2 fit) of the combined gain Tm(4.0 at.%):Lu$_2$O$_3$ and Tm(1.0 at.%):Sc$_2$O$_3$ laser using the 1.0% OC. (c) SHG interferometric and intensity autocorrelation traces after compression (red circle: measured data, grey: sech^2 fit, black: intensity autocorrelation).

Finally, in order to obtain the further shorter pulses at the expense of a reduced output power, we increased the quality-factor (Q-factor) of the cavity by replacing the 1.0% OC with a 0.5% OC. The KLM was obtained with the laser characteristics shown in Fig. 4.18.
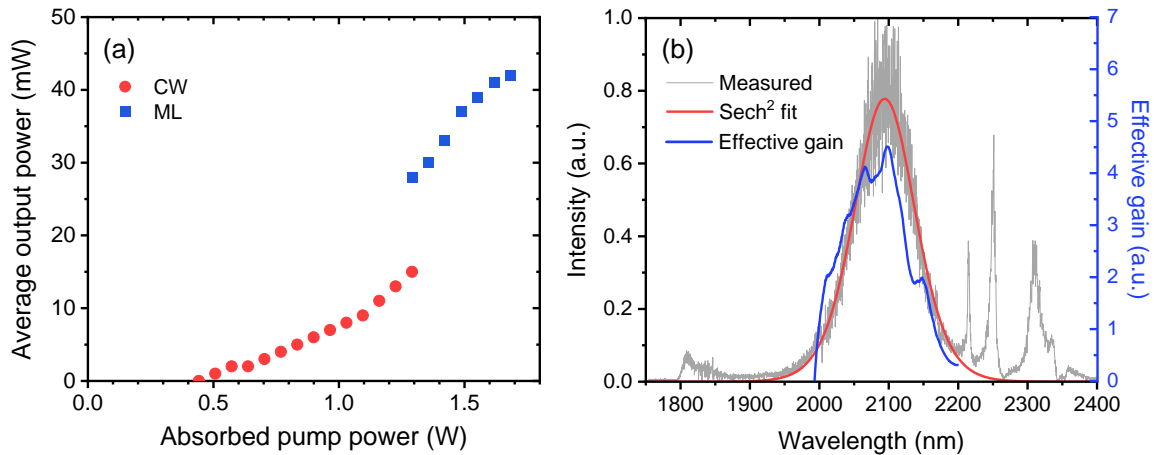
Figure 4.18: (a) Average output power and (b) optical spectrum (grey: measured spectrum, red: sech^2 fit, blue: effective gain spectrum of the combined gain) of the combined gain Tm(4.0 at.%):Lu$_2$O$_3$ and Tm(1.0 at.%):Sc$_2$O$_3$ laser using the 0.5% OC.

In this configuration, the broadest spectrum was observed at a center wavelength of around 2094 nm with a maximum average output power of 42 mW. In addition to the sech^2-shaped (soliton-shaped)

spectrum, some spectral components are found in the wavelength range between 2210 nm and 2350 nm as shown in Fig. 4.18(b), where both gain media have no gain (cf. Fig. 4.2). It should be noted that the reflection band of the OC is narrower than the mode-locked spectrum (up to ∼2170 nm, >99.0%). These additional spectral components could be explained by Raman-assisted spectral broadening [134] caused by a significantly increased intracavity peak power resulting from the high Q-factor cavity, since it was only observed for this 0.5% OC (This is described in the following Section 4.4.1 in more detail). In fact, while a reduced average power for lower OC transmittance, the laser using the 0.5% OC shows the highest intracavity peak power of 2.20 MW compared with 1.55 MW and 1.70 MW at 3.0% and 1.0% OC, respectively. Figure 4.20 shows the Raman gain spectrum of combined gain media. The wavelength range where the additional spectral components appeared is located inside the Raman gain band calculated as the convolution of the Raman spectrum and the soliton spectrum. The structural characteristics of the optical spectrum of the mode-locked pulses as well as the cavity conditions are similar to previous reports of spectral broadening due to intra-pulse SRS [134, 135]. The transform-limited pulse duration calculated using only the sech^2-shaped soliton mode-locked component of the optical spectrum is 45 fs. In contrast, from the whole spectrum, the transform-limited pulse duration reaches ∼29 fs as shown in Fig. 4.19(a).
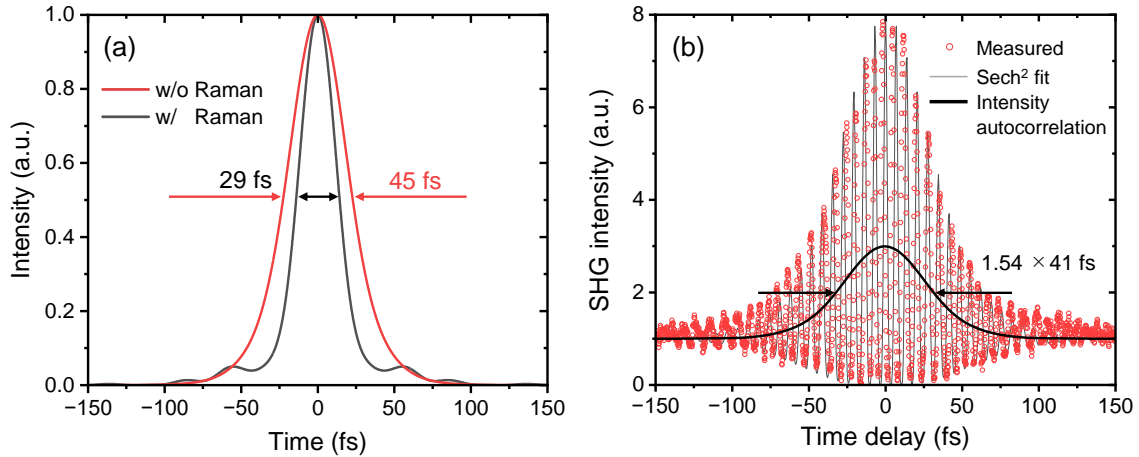
Figure 4.19: (a) Calculated transform-limited pulse duration with (grey) and without (red) the 2210-2350 nm spectral components. (b) SHG interferometric and intensity autocorrelation traces after compression (red circle: measured data, grey: sech^2 fit, black: intensity autocorrelation).

As an experimental result, the pulse duration measured by the SHG autocorrelation trace amounted to 41 fs (cf. Fig. 4.19(b)), which indicates that the additional spectral components contribute somewhat to pulse shortening. To evaluate the stability of ML operation, we measured radio frequency (RF) spectra shown in Fig. 4.21. The signal with a signal-to-noise ratio of more than 70 dB at the fundamental repetition rate of 93.3 MHz was obtained, thus we confirmed the stable ML operation.
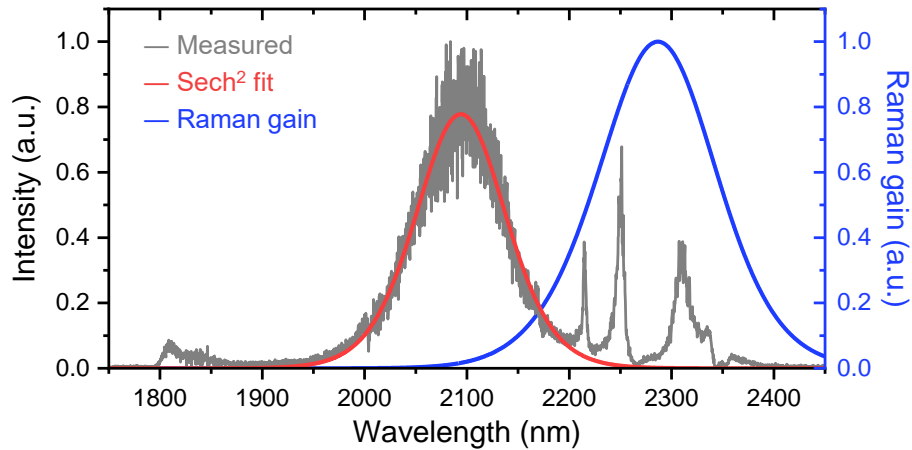
Figure 4.20: Mode-locked spectrum (grey) and Raman gain spectrum (red) of Tm:Lu$_2$O$_3$ and Tm:Sc$_2$O$_3$ combined media, which was calculated as the convolution of the Raman spectrum and the mode-locked spectrum.
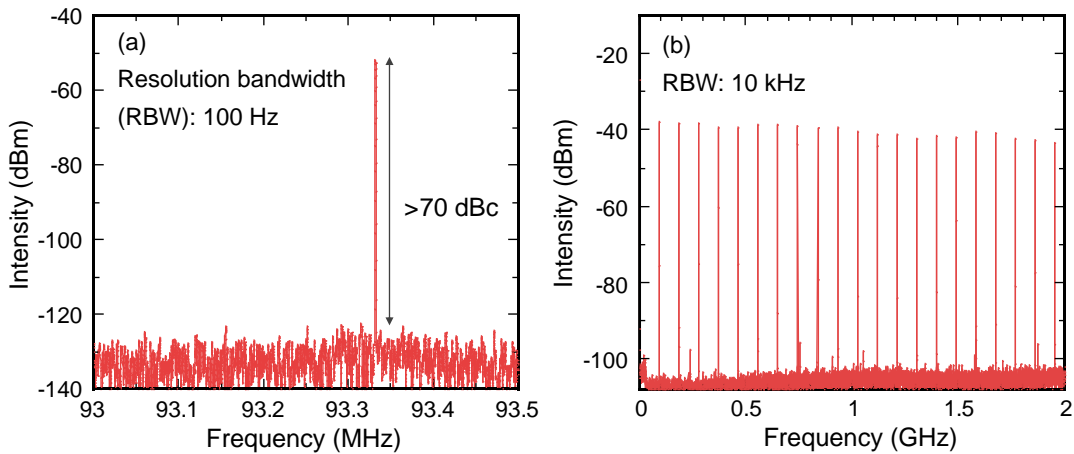
Figure 4.21: RF spectra in (a) 500 kHz and (b) 1 GHz span range.

Note that the additional spectral components act as a nonlinear loss for the ML pulses, as they do not contribute to stimulated emission owing to the lack of gain at these wavelengths (cf. Section 3.4). Therefore, a high modulation depth of KLM sustained extremely broadband ML laser operation without multi-pulsing or the appearance of narrow CW components in this case. Therefore, KLM has been shown to be a suitable method to achieve stable ML in the anomalous spectral broadening regime, thus overcoming the additional nonlinear losses. Moreover, it is worth noting that, although the spectra of the lasers are nonlinearly broadened (by Raman processes and/or self-phase modulation) beyond the gain bandwidth, the broadened gain bandwidth of the combined gain media is necessary to sustain mode-locked operation under such large nonlinear spectral broadening effect.

4.4   Discussions

4.4.1   Anomalous spectral broadening at longer wavelength region

In the last 5 years, ultrashort pulse generation from Tm-based solid-state ML lasers has significantly evolved. Actually, most of the ML spectra of mode-locked lasers with pulse durations on the order of 50-fs show anomalous spectral broadening in the longer wavelength range [29, 30, 26, 31, 135] as same as this study (cf. Fig. 4.18).

The intracavity spectral broadening was first explained by Kimura *et al.* [134]. They found anomalous spectral broadening in the high-Q cavity KLM Yb:CALGO laser. From the threshold-like behavior and the additional spectral components only present on the longer wavelength side, they attributed this to the intracavity SRS effect. The model and simulation using the nonlinear Schrödinger equation is described in Ref. [134]. They achieved pulse shortening from 67 fs to 22 fs by the use of broadened spectral components.

On the other hand, Zhao *et al.* attributed the observation of the anomalous spectral broadening to the multiphonon-assisted transitions of the Tm^{3+} ions [31]. They compared the Raman spectrum of the gain medium to the Stark sub-levels and concluded that the virtual energy levels created by phonon-electron coupling enable the longer wavelength emission, i.e. there is stimulated emission gain at the longer wavelengths where additional spectral components were observed. However, if there is really a stimulated emission gain, CW wavelength tuning should reach those wavelengths. Loiko *et al.* reported the extremely long wavelength laser operation using Tm:KLuW crystal in the CW and Q-switching regimes [143]. Liang *et al.* demonstrated extremely long wavelength operation using multiphonon-assisted transition in the Yb:YCOB laser by constructing high-Q cavity optimized for the particular wavelengths [144].
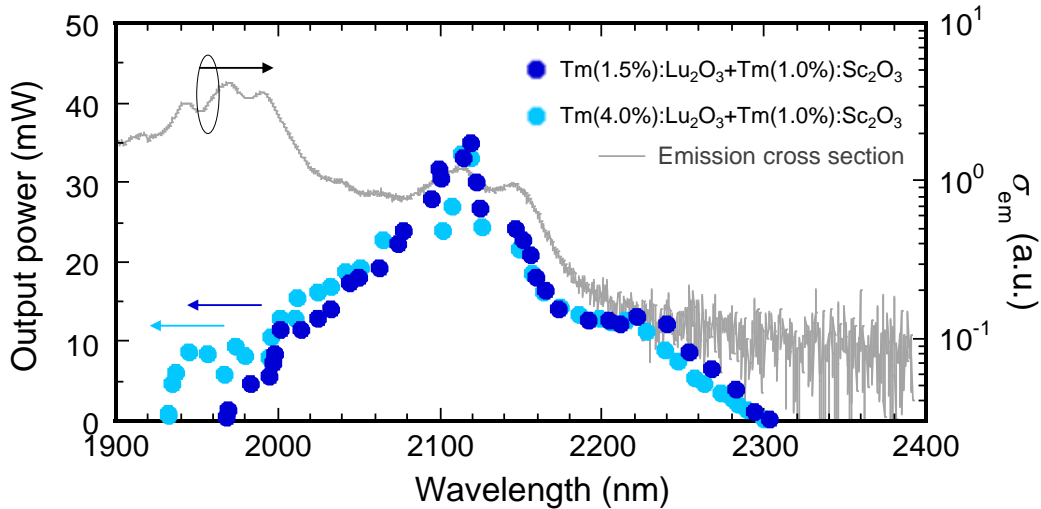
Figure 4.22: Wavelength tunability of the combined gain laser using high Q-factor cavity consisted of all cavity mirrors with high reflectivity R>99.9%(1980-2450 nm) and the emission cross section of the $Tm:Sc_2O_3$. Note that the $Tm:Sc_2O_3$ shows fluorescence at longer wavelengths than the $Tm:Lu_2O_3$, thus wavelength tuning above 2200 nm is achieved only by the gain of the $Tm:Sc_2O_3$.

Therefore, to see the multiphoton-assisted lasing in the Tm-doped sesquioxide laser, we did an additional wavelength tunable experiment using higher Q-factor cavity using a <0.1% OC. Figure 4.22 shows a wavelength tunability of the combined gain $Tm:Lu_2O_3$/$Tm:Sc_2O_3$ laser. The operation wavelength could reach up to 2300 nm. Concerning the emission cross section of the $Tm:Sc_2O_3$ (gray curve in Fig. 4.22), wavelength range beyond 2200 nm corresponds to the tail of the emission spectrum. Due to the limited sensitivity of the measurement system, it is difficult to identify the end of this tail, thus it may be possible to extend the laser wavelength toward further longer wavelengths by optimizing cavity condition. However, our experimental results indicate that, even though multiphonon-assisted transitions play a role, lasing beyond 2300 nm was impossible using the $Tm:Lu_2O_3$/$Tm:Sc_2O_3$ because there is no stimulated emission gain available beyond 2300 nm.

In addition, we observed the threshold-like behavior of the anomalous spectral broadening during the KLM experiment. Figure 4.23 shows examples of observed laser spectra in the KLM $Tm:Lu_2O_3$ laser. By increasing pump power, the soliton spectrum centered around 2100 nm was significantly broadened at the average output power of 10.3 mW. At the same time, additional spectral components appeared above 2200 nm. The broadened spectrum indicates a shorter pulse duration, resulting in increase of the peak intensity. Therefore, the appearance of the additional spectral components can be explained by the nonlinear effect and the experimental result is consistent with the report which attributes the anomalous spectral broadening to intracavity SRS [134].
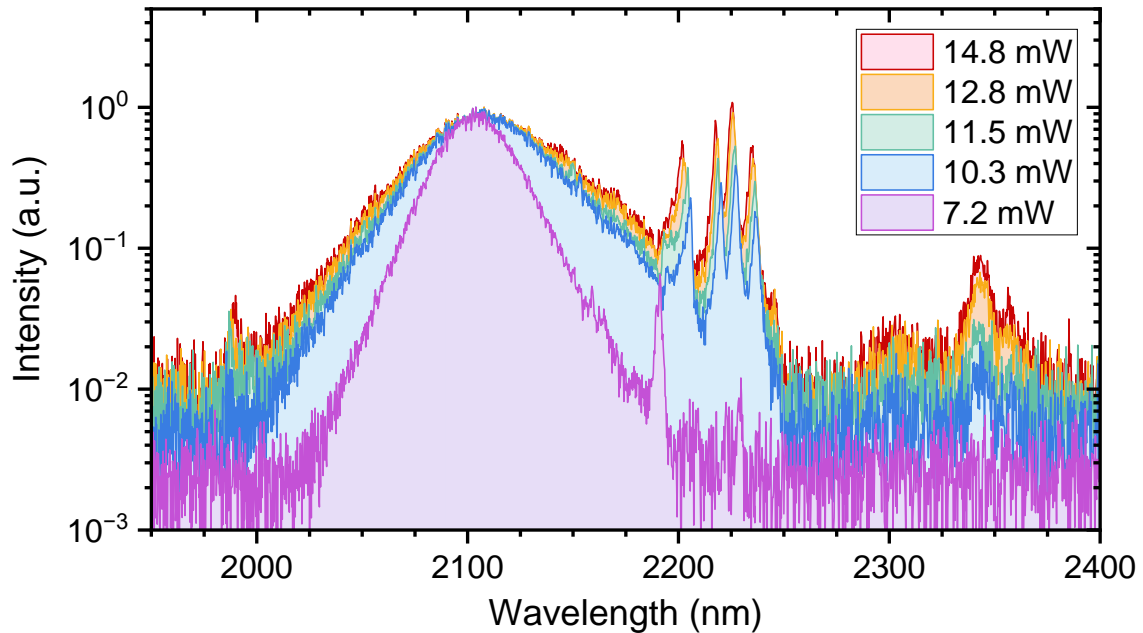
Figure 4.23: Optical spectra of the high Q-factor KLM $Tm:Lu_2O_3$ laser at different average output power.

4.4.2   Comparison with single-gain ML lasers

To evaluate the impact of the combined gain media, we compare with the KLM single gain lasers [135, 133]. KLM experiments of the single gain Tm-doped sesquioxide lasers were performed using the same cavity configuration and the pump source as described above. The properties of the gain media and cavity GDD are shown in Table4.3. The shortest pulse duration was obtained using a 0.5% OC among a variety of OCs for both cases.

Table 4.3: Properties of the Tm:Lu$_2$O$_3$ and the Tm:Sc$_2$O$_3$, and the cavity GDD.

Gain medium	Total GDD (fs^2)
4.0 mm, Tm(4.0 at.%):Lu$_2$O$_3$ ceramic	-1160
3.7 mm, Tm(1.0 at.%):Sc$_2$O$_3$ crystal	-1420
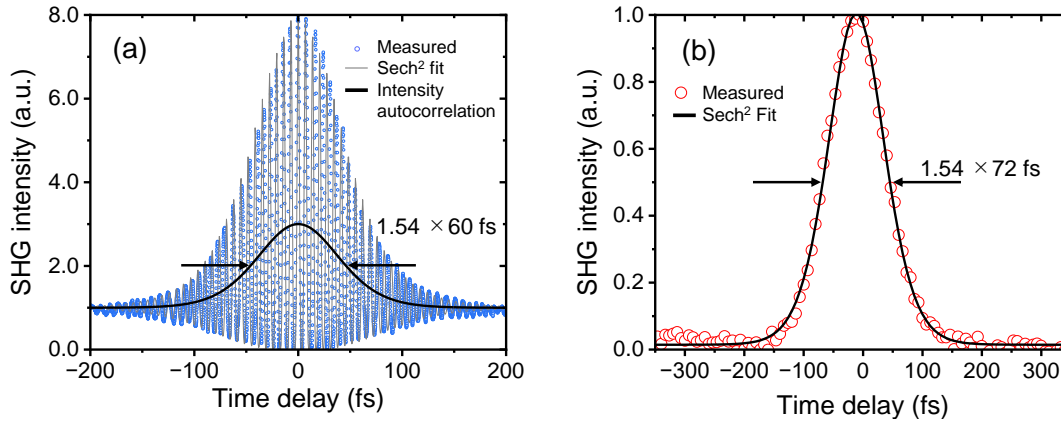
Figure 4.24: Intensity autocorrelaion trace of the KLM (a)Tm:Lu$_2$O$_3$ and (b) Tm:Sc$_2$O$_3$ lasers.

We obtained mode-locked laser operation with the pulse duration of 60 fs and 72 fs after compression using the Tm:Lu$_2$O$_3$ and the Tm:Sc$_2$O$_3$, respectively. Figure 4.24 shows the autocorrelation trace of the KLM Tm:Lu$_2$O$_3$ and Tm:Sc$_2$O$_3$ lasers. The maximum average output power was 81 mW and 130 mW, respectively. Figure 4.25 shows the comparison of optical spectra of the single gain KLM Tm:Lu$_2$O$_3$ laser and the Tm:Sc$_2$O$_3$ laser, and the combined gain KLM laser. The center wavelengths of the single-gain lasers were 2100 nm and 2108 nm and the spectra were broadened from 1980 to 2240 nm and from 2000 to 2220 nm for the Tm:Lu$_2$O$_3$ and the Tm:Sc$_2$O$_3$, respectively. The narrow spectral peaks on the spectra could be Kelly sidebands which are often found in soliton ML lasers [145, 146]. The soliton-shaped optical spectrum of the combined gain laser covers the whole spectral range of both single-gain lasers and is further broadened toward shorter wavelengths. As described in Section 4.1.2, the difference between the single gain medium and the combined gain media is gain saturation. In the combined gain media, gain saturation would inhomogeneously occur, while it homogeneously occurs in the single gain medium. That should support the spectral broadening in the mode-locked operation. Therefore, the experimental results indicate that the ultrashort pulse generation in the combined gain laser was achieved by the broad and flat gain profile as well as inhomogeneous gain saturation in the combined gain media.
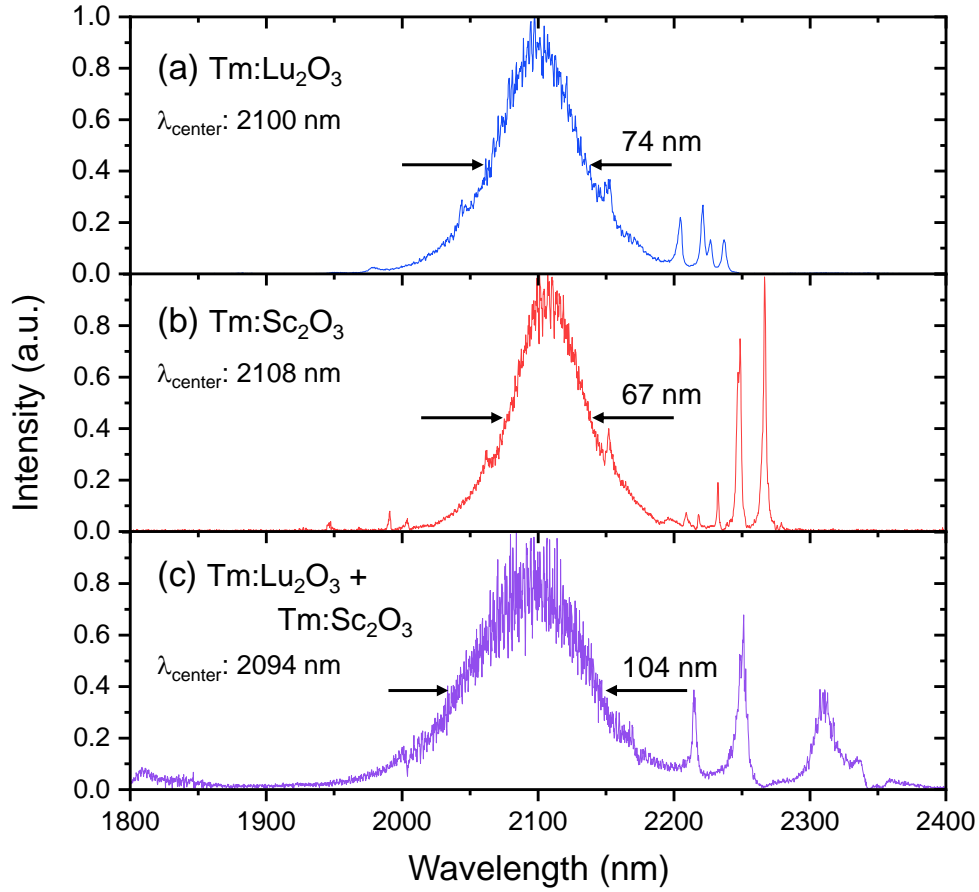
Figure 4.25: Optical spectra of the KLM (a) $Tm:Lu_2O_3$, (b) $Tm:Sc_2O_3$, and (c) combined gain lasers.

4.5 Summary

In this chapter, we demonstrate the combined gain KLM lasers aiming for the broader gain bandwidth exceeding the limit of the single gain medium. By combining a $Tm:Lu_2O_3$ and a $Tm:Sc_2O_3$, a broad and flat effective gain profile was obtained. In addition, we confirmed that the effective gain spectrum changes by changing the contribution of each gain medium from the calculation. The highest slope efficiency of 60% in the CW operation shows the highly efficient laser performance with the combined gain configuration, and the extremely broad tuning range from 1890 to 2243 nm indicates the huge potential for the ultrashort pulse generation. In the KLM experiments, using a 3.0% OC, the highest average output power of 538 mW with a pulse duration of 118 fs was achieved. In a high-Q-factor cavity configuration using a 0.5% OC, the pulse duration of 41 fs corresponding to 5.9 optical cycles was obtained. Figure 4.26 shows the average output power and the pulse duration of Tm-based mode-locked bulk lasers. We achieved the shortest pulse duration and high average power laser operation with relatively short pulse durations. These results were achieved by the broadband gain and the flat gain profile adjusted by the proper combination of the gain materials with the suitable doping concentration and the pumping condition.
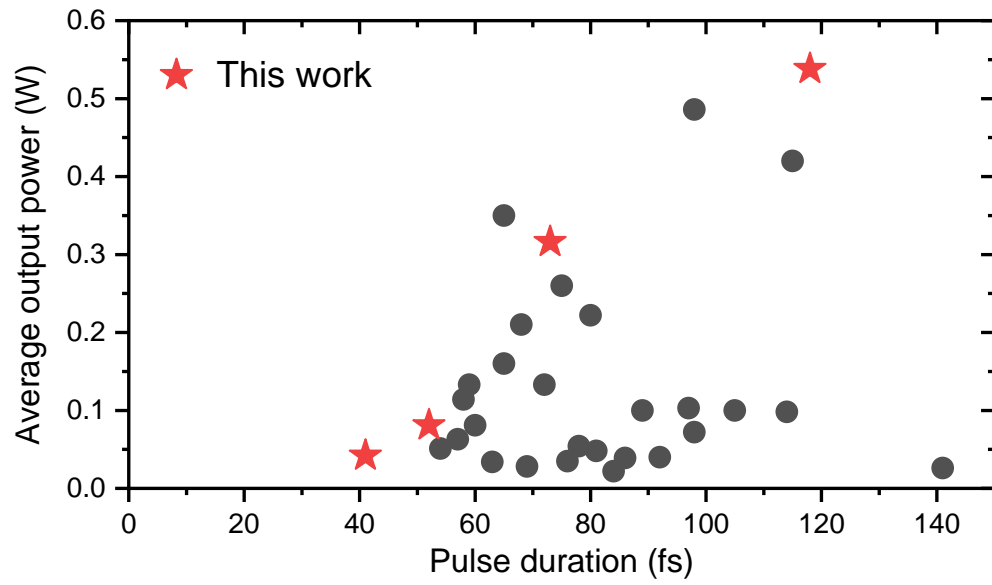
Figure 4.26: Average output power and pulse duration of Tm-based mode-locked bulk lasers.

Chapter 5

Tm-doped mixed sesquioxides

This chapter proposes another idea to realize a broadband gain. Here, mixed sesquioxides consist of three cubic sesquioxides in an arbitrary ratio $(\mathrm{Lu}_x\mathrm{Sc}_y\mathrm{Y}_z)_2\mathrm{O}_3$ $(x + y + z = 1)$, so that the optical spectra can be considered as the average of those of Tm-doped pure sesquioxide. This idea is similar to combined gain media. However, doped ions in the mixed sesquioxides are influenced by various crystal fields owing to randomly distributed host cations (cf. Fig. 5.1), resulting in broader and smoother spectral profile by inhomogeneous spectral broadening. Moreover, as described in Section 2.3, the fabrication of conventional sesquioxides is challenging. Although the combined gain sesquioxide laser has been shown as a powerful technique for high-power ultrashort pulse generation, the laser performance strongly depends on the quality of the gain materials [147]. In this chapter, we demonstrate the crystal growth of Tm-doped mixed sesquioxides, and spectroscopic investigations and laser experiments were carried out to explore its potential for ultrafast lasers.

Section 5.1.1 gives a background of this study including the history of the fabrication and laser applications of mixed sesquioxides. Section 5.2 deals with the Cz-growth. Subsequently, the characterizations of as-grown crystals are described in Section 5.3. Section 5.4 deals with the laser experiments using as-grown crystals and different pump sources, and Section 5.6 gives a discussion about the results and comparison with ceramics technology.
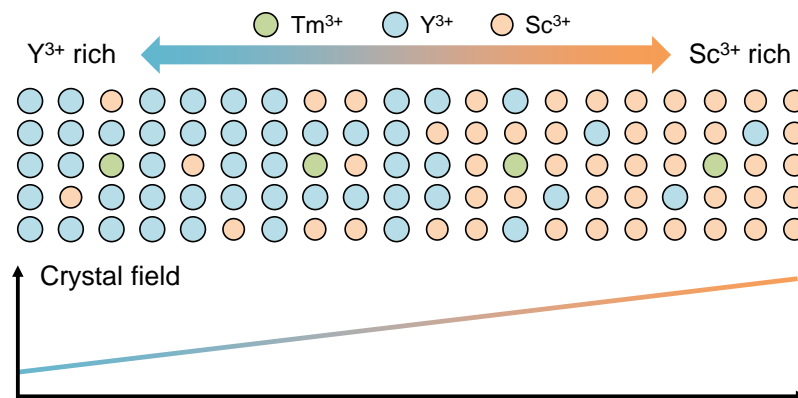
Figure 5.1: Conceptional schematic of mixed sesquioxide crystal structure (oxygen ions are omitted) with varied crystal field strength.

5.1   Introduction

5.1.1   Historical overview on mixed sesquioxides for solid-state lasers

As the first investigation of mixed sesquioxide as a laser material, Bagdasarov et al. focused on Nd:YScO$_3$ in 1975 [148]. Afterward, the main advantage of the mixed sesquioxide regarding broad spectral features was revealed using Yb:LuScO$_3$ in the 2000s [149, 150, 151, 152]. The Yb:LuScO$_3$ shows an emission bandwidth of more than 20 nm and pulses as short as 74 fs were achieved by KLM laser [152].

In the last decade, Tm-doped mixed sesquioxides have also been investigated for 2 µm ultrafast lasers. A Tm:LuScO$_3$ crystal was grown by the HEM method [153] and highly efficient CW laser operation with a slope efficiency of 55% was demonstrated [61]. In addition, a SESAM mode-locked Tm:LuScO$_3$ laser achieved 148-fs pulses [58]. This was the only Tm-doped mixed sesquioxide crystal reported so far, because of the difficulties in the growth of the high-quality sesquioxide crystals. Therefore, in recent years, mixed sesquioxide ceramics have been highly developed. There are many successful reports on their fabrication [90, 154, 155] as well as CW [155, 156, 157] and ML lasers [31, 44, 29, 26]. However, the laser efficiencies with sesquioxide ceramics did not reach the results with single crystals [158]. This can be partly attributed to the tendency for increased scattering losses in ceramics (cf. Section 2.3).
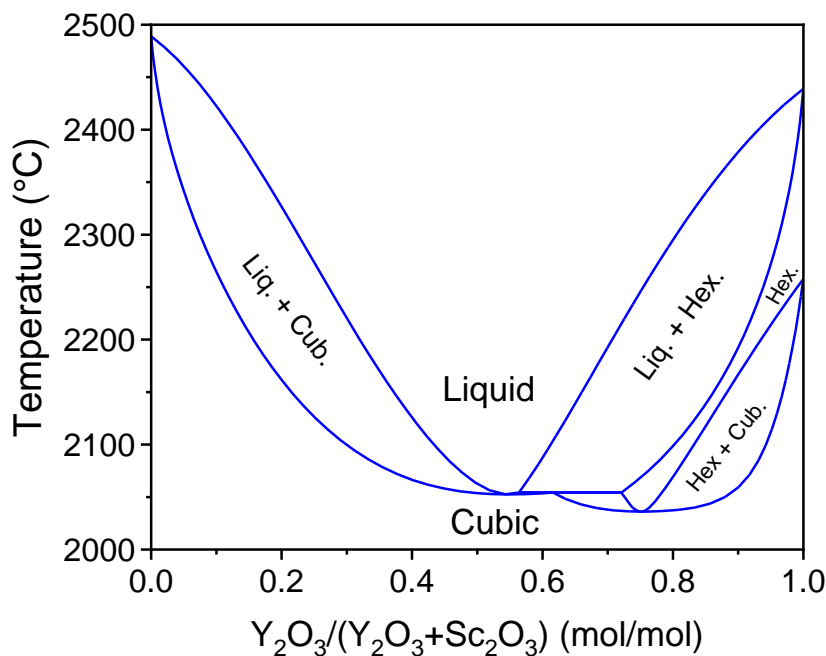
Figure 5.2: Binary phase diagram of the system Sc$_2$O$_3$-Y$_2$O$_3$ [62].

In 2021, Kränkel et al. reinvestigated the phase diagram of mixed sesquioxides [62] and revealed the availability of the Cz method for mixed sesquioxide crystal growth. Figure 5.2 shows the binary phase diagram of the system Sc$_2$O$_3$-Y$_2$O$_3$. The lowest melting temperatures below 2150°C were

found in the composition around $Sc_2O_3:Y_2O_3 = 50:50$. This temperature range is suitable for the conventional Cz method using iridium (Ir) crucibles to grow large-size high-quality laser crystals. Until now, Er- and Yb-doped mixed sesquioxides have been successfully grown by the Cz method. Particularly for Yb:$YScO_3$, highly efficient laser operation was demonstrated [159]. These studies show the huge potential of the Cz-grown mixed sesquioxide crystals as highly efficient laser material as well as their future commercial availability.

5.1.2 Comparison with ceramics technology

For rare-earth-doped cubic sesquioxides, ceramics are excellent host materials as they can be fabricated at significantly lower sintering temperatures than their melting temperatures. Moreover, especially for the SWIR lasers, the influence of scattering in the ceramics can be mitigated compared with the conventional Vis-NIR lasers as scattering losses decrease in proportion to wavelength λ^{-4}. The fabrication of transparent $YScO_3$ ceramics is reported by several groups [160, 161, 162, 163]. However, $YScO_3$ has a perovskite phase at 1200-1700°C [164, 165] and perovskite $YScO_3$ exhibits uniaxial birefringence which causes scattering losses at grain boundary. Therefore, the formation of the perovskite phase should be avoided and the formation of single-phase bixbyite $YScO_3$ requires special treatment. According to Ref. [164], in the rare-earth scandates (RE_2O_3-Sc_2O_3, RE = rare-earth ion), the formation of the perovskite phase is inhibited by decreasing the ion radius of RE^{3+}. $YScO_3$ which has moderate ion radii partly made perovskite phase by sintering in air at 1600°C.

```
┌─────────────────────────────────────┐
│   Weight the starting materials      │
│   (Tm_0.02 Y_0.49 Sc_0.49)_2 O_3     │
└─────────────────────────────────────┘
                  │
                  ▼
┌─────────────────────────────────────┐
│   Ball milling (wet milling) (6 h)   │
└─────────────────────────────────────┘
                  │
                  ▼
┌─────────────────────────────────────┐
│      Remove ethanol solvent          │
│      by drying mill slurry           │
└─────────────────────────────────────┘
                  │
                  ▼
┌─────────────────────────────────────┐
│          Molding to a rod            │
└─────────────────────────────────────┘
                  │
                  ▼
┌─────────────────────────────────────┐
│   Cold isostatic pressing (CIP)      │
│      (180 sec, 2000 bar)             │
└─────────────────────────────────────┘
                  │
                  ▼
┌─────────────────────────────────────┐
│         Sintering (10 h)             │
│ at 300, 600, 900, 1200, 1500, 1700 °C│
└─────────────────────────────────────┘
                  │
                  ▼
┌─────────────────────────────────────┐
│        Powder-XRD analysis           │
└─────────────────────────────────────┘
```
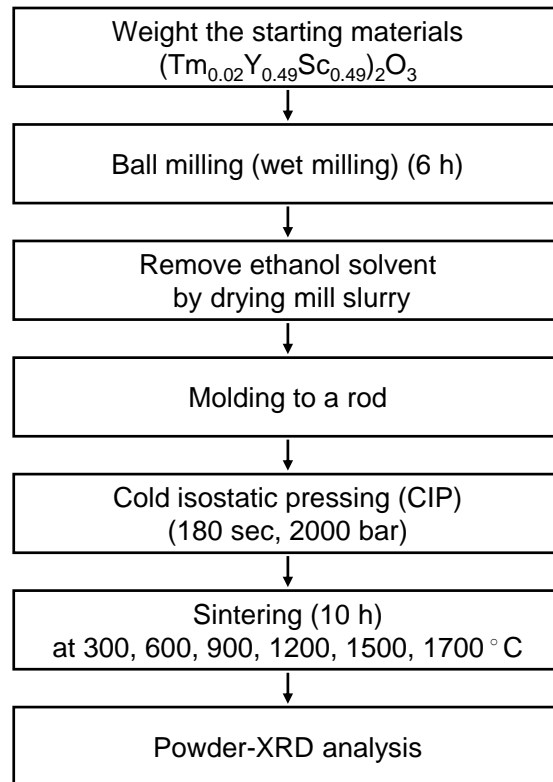
Figure 5.3: Procedure of TmYScO$_3$ sintering experiment.

To observe the phase transition in the Y_2O_3-Sc_2O_3 system in the temperature range between 300 and 1700°C, we performed an experiment following the procedure shown in Fig. 5.3. The raw materials of Tm_2O_3, Y_2O_3, and Sc_2O_3 were prepared according to the composition of $(Tm_{0.002}Y_{0.49}Sc_{0.49})_2O_3$. It was uniformly mixed by ball milling, and it was afterward molded in a rod shape and sintered in air at different temperatures. The phase of the sintered materials was identified by powder-X-ray diffraction (XRD) measurements. Figure 5.4(a) shows the XRD-pattern of the sintered materials. At sintering temperature of 1200°C, the perovskite phase appeared. The peaks in the XRD pattern of sintering temperature of 1700°C shown in Fig. 5.4(b) indicate the mixture of perovskite and bixbyite phase.

According to Ref. [164], the formation of the perovskite phase is supported by the high-pressure environment, and single-phase perovskite was obtained by sintering under 20,000 MPa. The formation of the perovskite phase is also depending on the synthesis method [165]. Therefore, to avoid the formation of the perovskite phase, the synthesis under low pressure is desirable, thus the vacuum sintering method is suitable to obtain single-phase bixbyite $YScO_3$ [161]. For the laser quality Tm-doped $YScO_3$ ceramics, Pirri et al. fabricated a $(Tm_{0.05}Y_{0.698}Sc_{0.252})_2O_3$ ceramic and lasing could be obtained with a maximum slope efficiency of 9.45% and tuning range from 1927 to 2108 nm [160]. The laser performance seemed to be limited by the quality of the ceramics. In addition, transparent $YScO_3$ ceramics were only reported with Y-rich compositions [161, 162], although they could suppress the formation of perovskite phase even in the Sc increased compositions. On the other hand, $YScO_3$ crystals can not be grown with Y-rich compositions because of the existence of hexagonal phase at higher temperatures, and the crystal growth is only possible with around $(Y_{0.5}Sc_{0.5})_2O_3$ compositions. In terms of the spectral broadening effect in the mixed material, the broadest emission spectrum can be obtained with the composition where each host material contributes equally [166]. Therefore, for ultrafast lasers, the Cz-grown $Tm{:}YScO_3$ cystals should be advantageous in terms of the spectroscopic properties and the quality of as-grown crystals.
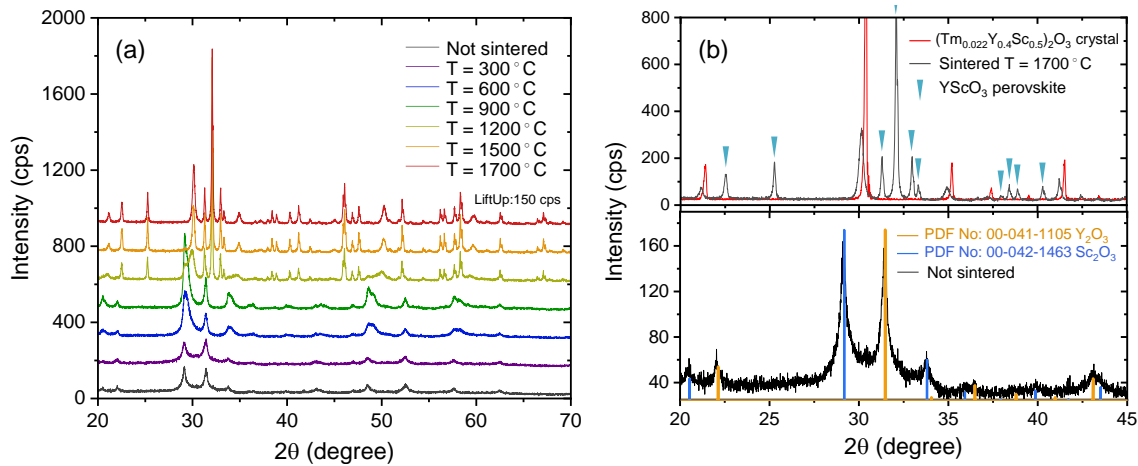
Figure 5.4: XRD pattern of (a) $(Tm_{0.02}Y_{0.49}Sc_{0.49})_2O_3$ sintered at different temperatures and (b) comparison with peaks of Y_2O_3, Sc_2O_3, $YScO_3$ bixbyite, $YScO_3$ perovskite phase.

5.1.3   Spectroscopic characteristics of mixed sesquioxides

In the mixed sesquioxides $(Lu_xSc_yY_z)_2O_3$ $(x + y + z=1)$, the difference of lattice constant of the constituents leads to distortion of crystal structure, resulting in various crystal field strengths. That makes the absorption and emission spectra broad and smooth, i.e., inhomogeneous spectral broadening effect. Among cubic sesquioxides, Sc_2O_3 has the smallest lattice constant (Sc_2O_3: 9.86, Y_2O_3: 10.60, Lu_2O_3: 10.39 Å), thus by mixing Sc_2O_3 with Lu_2O_3 or Y_2O_3, a large modification of the crystal field strength would be expected. Mixed sesquioxides combine the absorption and emission features of their constituents. Tm-doped Sc_2O_3 shows the emission band in significantly longer wavelength region compared with that of Tm-doped Lu_2O_3 and Y_2O_3 [158]. Therefore, it is intuitive that the emission band of Tm:LuScO$_3$ or Tm:YScO$_3$ extends to longer wavelengths compared with Tm:LuYO$_3$. It should be noted that as the emission wavelengths of Tm:Lu$_2$O$_3$ and Tm:Y$_2$O$_3$ are almost the same, the combined emission band in Tm:LuScO$_3$ and Tm:YScO$_3$ are also almost identical. Besides, in the mixed sesquioxides, the peak wavelengths of absorption and emission spectra would be tuned by changing the compositions, however, it depends on the availability of the fabrication method with desired compositions.

In this study, we demonstrate the Cz-growth of Tm-doped mixed sesquioxide crystals for ultrashort pulse lasers. Because of the availability and the Cz-growth method and expected spectroscopic features, we choose Y_2O_3 and Sc_2O_3 as the host material.

5.2   Czochralski growth of mixed sesquioxide

Tm-doped YScO$_3$ crystals were grown by the Czochralski method from Ir crucibles. The raw materials of Tm_2O_3, Y_2O_3, and Sc_2O_3 powders with a purity of 99.999% (5N) were mixed for the compositions $(Tm_{0.02}Y_{0.49}Sc_{0.49})_2O_3$ and $(Tm_{0.028}Y_{0.486}Sc_{0.486})_2O_3$. The detailed growth procedure and parameters for each growth are shown in Fig. 5.5 and Table 5.1. The starting powders prepared according to the procedure were placed in an RF-heated Ir crucible ($\approx$40 mm both in diameter and height) embedded in ZrO_2 and Al_2O_3 insulation. The growth was performed using a Yb(0.4 at.%):YScO$_3$ crystal as a seed crystal with random orientation. To reduce the vertical thermal gradient in the growth setup, an Ir afterheater was utilized.

Table 5.1: Growth parameters for Tm-doped YScO$_3$ crystals

	Growth rate (mm/h)	Rotation rate (rpm)	Growth atmosphere	Cooling time (h)
1st growth	0.7	10	Static 100% Ar	15
2nd growth	0.6	10	Flowing 100% Ar	24

The photographs of two as-grown crystal boules with different Tm-doping levels are shown in Fig. 5.6. These are transparent and show no inclusions. For both crystals, length and diameter were about 5 cm and 2 cm, respectively. At the bottom of the boule, a spiral formation was observed for both crystals. This growth instability is owed to the absorption of thermal radiation during growth and reduced heat transportation at high growth temperatures. This is also found in the Cz-growth of pure sesquioxides [167].
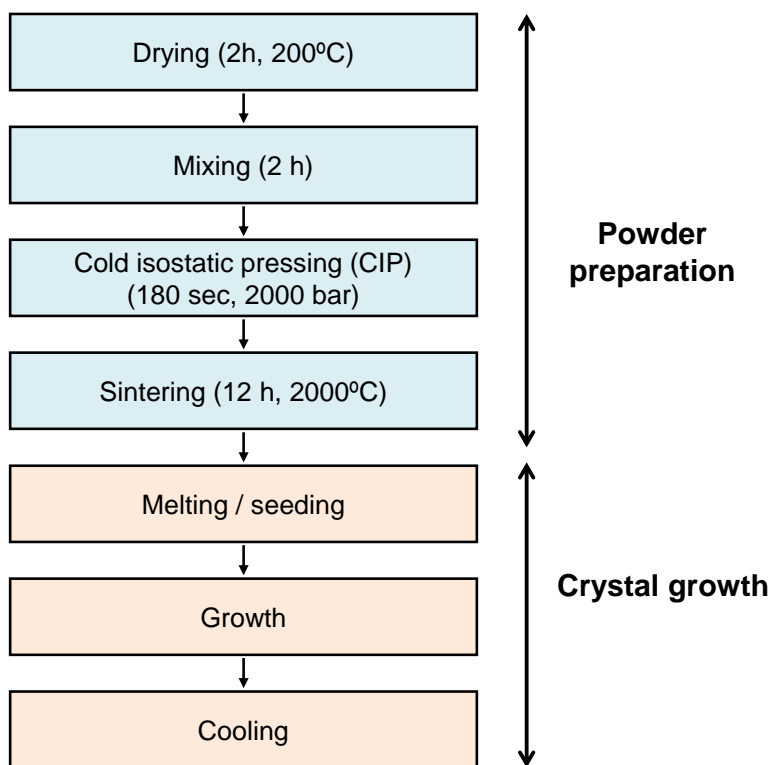
Figure 5.5: Cz growth procedure.
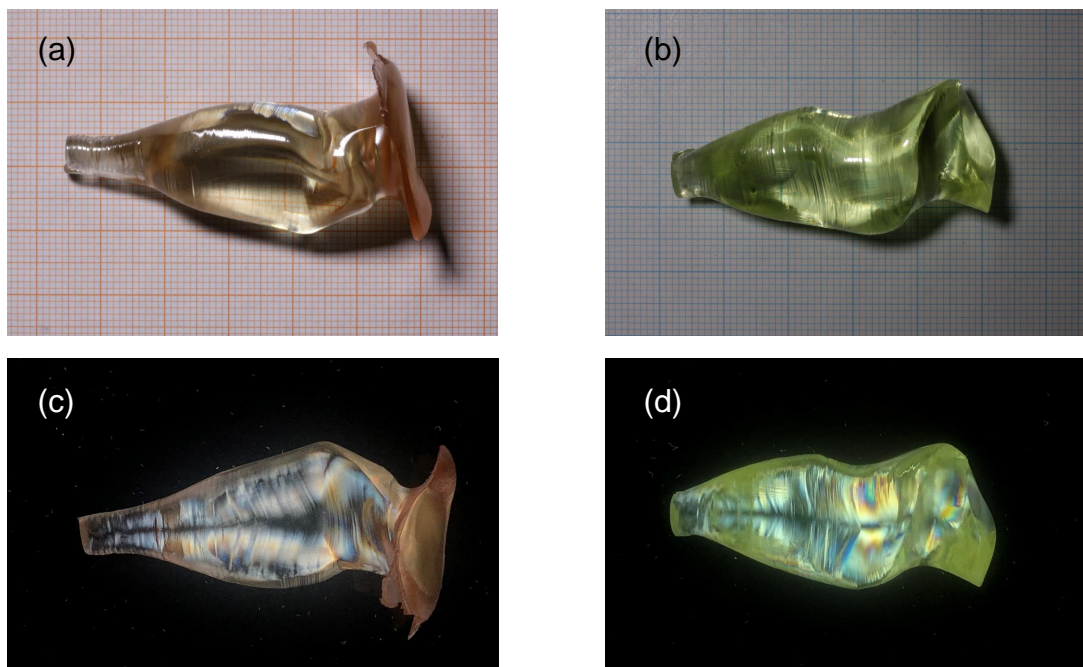
Figure 5.6: Photographs of the as-grown (a) Tm(2.2 at.%):YScO$_3$ and (b) Tm(3.1 at.%):YScO$_3$ crystals. Cross polarizer images of (c) Tm(2.2 at.%):YScO$_3$ and (d) Tm(3.1 at.%):YScO$_3$ crystals.

The 1st crystal grown in a static Ar atmosphere shows brownish color. The transmission spectrum of the 1st sample was measured from ultra violet (UV) to NIR wavelength range using a dual-beam UV/Vis/NIR spectrometer (Perkin Elmer, Lambda 1050) set to a resolution of 1 nm (shown in Fig. 5.7). This spectrum was not corrected for Fresnel reflection. The broad absorption can be seen from UV to 1000 nm, but this color could be removed by annealing in a reducing atmosphere (forming gas with a composition of H_2:N_2=5:95) at 1500°C for 15 h as seen in the blue curve in Fig. 5.7.
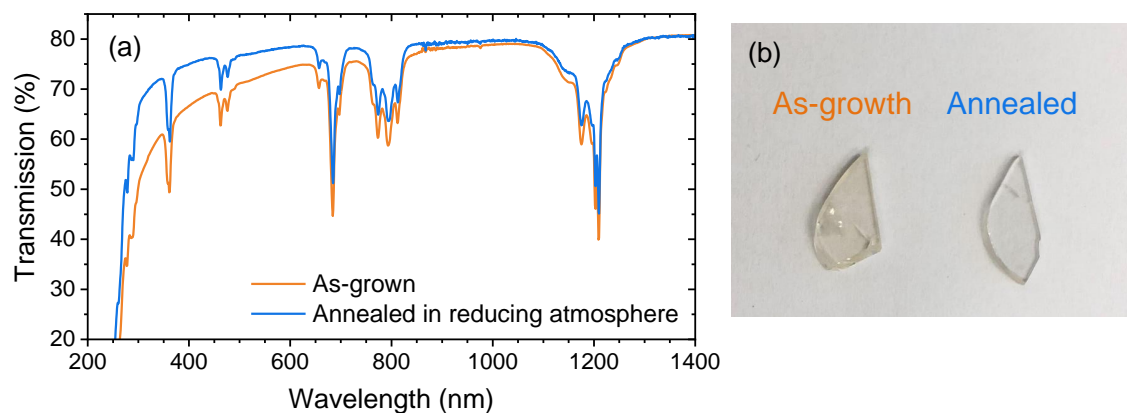
Figure 5.7: (a) Transmission spectra of the as-grown (orange) and annealed in reducing atmosphere (blue) Tm(2.2 at.%):$YScO_3$ crystal shown in Fig. 5.6(a) in the UV to the NIR spectral range. (b) Photograph of the as-grown and annealed sample.

From this result, the coloration seemed to be caused by an excess of oxygen in the growth atmosphere, however, the origin of this coloration is still unclear. Subsequently, the 2nd growth run was performed in a continuously flowing As gas to exclude residual oxygen from the furnace. This results in the greenish-colored crystal, which is typically found in Tm-doped crystals and no further annealing is required for this boule.

Figures 5.6(c, d) show cross polarizer images of the as-grown crystals. The bright parts indicate light depolarization due to strong internal stress. This stress may be induced by the thermal gradient during growth. To solve this problem, second growth run was performed with a slower pulling speed and longer cooling time. However, this did not mitigate the stress. Eventually, a lot of cracks were made during cutting the crystals.

5.3 Characterizations

5.3.1 Crystallography

Powder-XRD measurement

Powder-XRD measurements were performed to evaluate the phase of the crystal and determine the lattice constant. Figure 5.8 shows the measured XRD-pattern and PDF references of bixbyite Sc_2O_3 (lattice constant a = 9.846 Å) and Y_2O_3 (a = 10.604 Å). Each peak indicates the mirror index of cubic structure. The peak positions locate between those of Sc_2O_3 and Y_2O_3 as expected. Based

on the peak positions, the lattice constant of Tm(2.2 at.%):YScO$_3$ was calculated to be 10.14 Å by the Vegard's law. Thus the cation density was 3.07×10^{22} cm^{-3}.
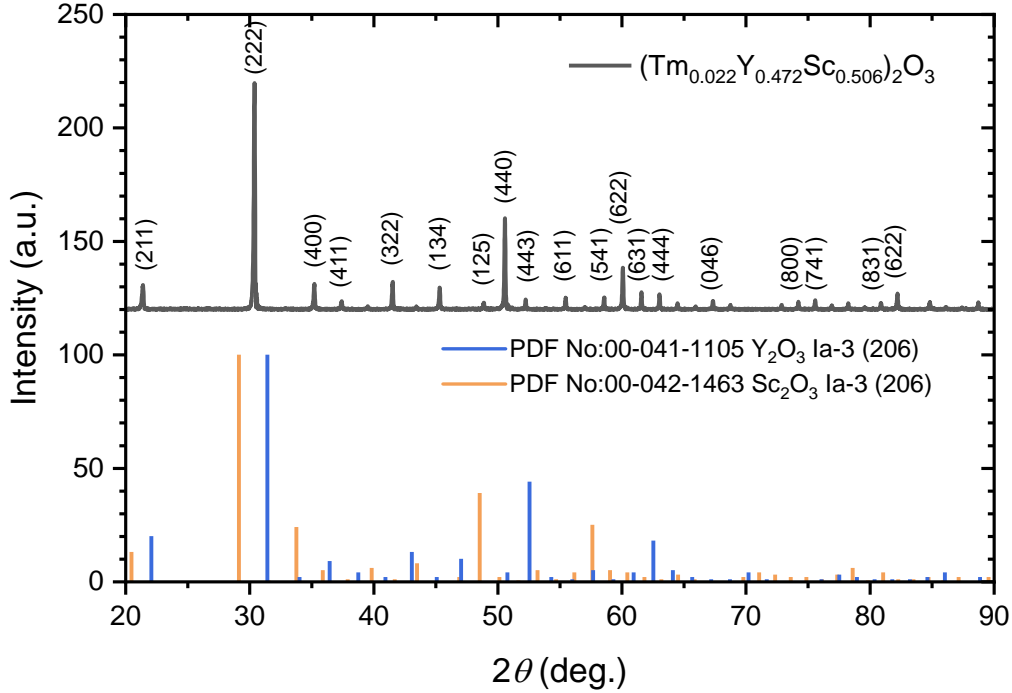
Figure 5.8: Powder-XRD pattern and mirror indices of (Tm$_{0.022}$Y$_{0.472}$Sc$_{0.506}$)$_2$O$_3$ and the standard pattern of Sc$_2$O$_3$ and Y$_2$O$_3$.

ICP-OES analysis and segregation coefficient

The actual crystal composition was investigated by inductively coupled plasma optical emission spectrometry (ICP-OES) analysis using the top part of each crystal boule. The determined compositions are shown in Table 5.2. From the difference of the composition between the initial melt and the crystal, Tm^{3+} may preferentially substitute Y^{3+} rather than Sc^{3+} site as expected with respect to their ionic radii (Sc: 0.885, Tm: 1.020, Y: 1.040 Å for sixfold coordination).

Table 5.2: Composition of the crystals

	Starting powder	As-grown crystal
1st crystal	(Tm$_{0.02}$Y$_{0.49}$Sc$_{0.49}$)$_2$O$_3$	(Tm$_{0.022}$Y$_{0.472}$Sc$_{0.506}$)$_2$O$_3$
2nd crystal	(Tm$_{0.028}$Y$_{0.486}$Sc$_{0.486}$)$_2$O$_3$	(Tm$_{0.031}$Y$_{0.474}$Sc$_{0.495}$)$_2$O$_3$

Regarding the Tm^{3+} concentration along the growth direction, the segregation coefficient k can be calculated via the Scheil equation:

$$C_s(g)/C_0 = k(1-g)^{(k-1)}, \tag{5.1}$$

where $C_s(g)$ is the solute concentration in the grown crystal, g is the fraction of the melt solidified to the initial melt, and C_0 is the solute concentration in the initial melt. Here, for small g (beginning of the crystal), k can be calculated simply as $C_s(g)/C_0$. The calculated segregation coefficients for Tm^{3+}, Y^{3+} and Sc^{3+} are shown in Table 5.3.

Table 5.3: Segregation coefficients k of the as-grown crystals.

	Tm^{3+}	Y^{3+}	Sc^{3+}
1st crystal	1.10	0.96	1.03
2nd crystal	1.11	0.97	1.02

Figure 5.9 shows the variation of Tm^{3+} concentration along the growth direction assuming a segregation coefficient of 1.1. Considering the fact that we never used more than $\sim 1/3$ of the starting materials for the growth due to the spiral formation, the actual Tm concentration only varies between 2.2 at.% and 2.1 at.%, 3.1 at.% and 3.0 at.% for the lower doped and higher doped sample, respectively as shown in Fig. 5.9. Because we only used the upper part of the crystal boule (less than 1 cm from the top) for the spectroscopy and laser experiments, hereafter we consistently denote the actual concentration as Tm(2.2 at.%):YScO$_3$ and Tm(3.1 at.%):YScO$_3$.
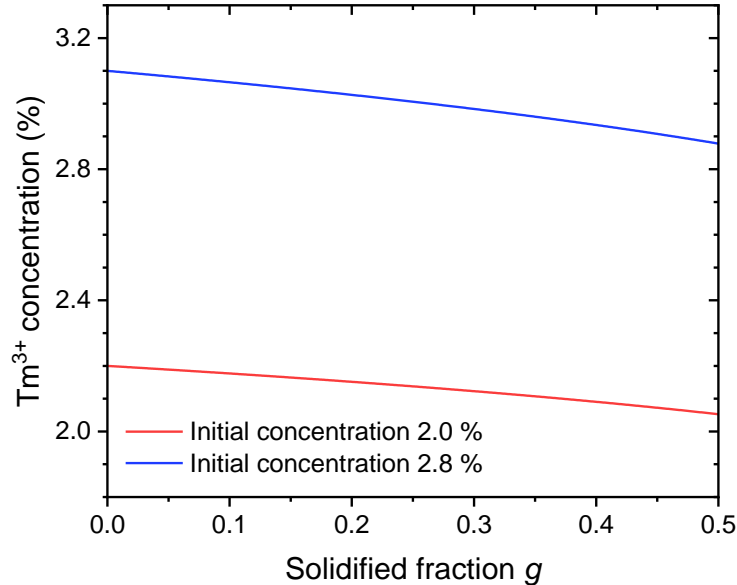
Figure 5.9: Variation of the Tm concentration over solidified fraction assuming the segregation coefficients shown in Table 5.3 and the initial concentration of 2.0 at.% (red) and 2.8 at.% (blue).

Raman spectra

The room temperature Raman spectrum of the as-grown crystal was measured by a laser Raman microscope (JASCO, NRS-3100). Cubic sesquioxides, which have space group of $Ia\bar{3}$ predicts the irreducible representations for the optical mode Γ_{op} and the acoustical mode Γ_{ac} for the group theory

as follows [168]:

$$\Gamma_{op} = 4A_g + 4E_g + 14F_g + 5A_{2u} + 5E_u + 16F_u, \tag{5.2}$$

$$\Gamma_{ac} = F_u. \tag{5.3}$$

Here, for the optical modes, 22 modes $(4A_g + 4E_g + 14F_g)$ are Raman-active, 16 modes $(16F_u)$ are IR-active, and the rest $(5A_{2u} + 5E_u)$ are silent.
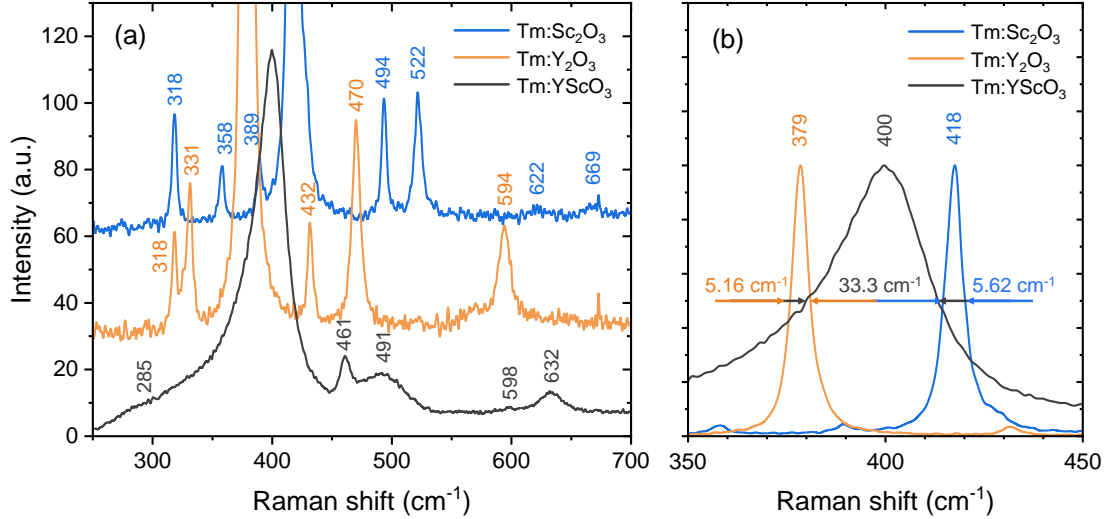
Figure 5.10: Unpolarized Raman spectra of Tm-doped $YScO_3$ and Sc_2O_3 crystals and non-doped Y_2O_3 ceramic (a) in the range between 200 - 700 cm^{-1} and (b) around the most intense peak.

Figure 5.10 shows the Raman spectra of the Tm-doped $YScO_3$ and Sc_2O_3 crystals and non-doped Y_2O_3 ceramic for comparison. For the Tm:Sc_2O_3 and the Y_2O_3, the overall shape and peak positions in the spectrum were consistent with the previously published reports [169, 170]. For the Tm:$YScO_3$, due to the mixed feature, each peak was significantly broadened (FWHM: ≈ 33.3 cm^{-1}) and the number of identified peaks reduce compared with the non-mixed sesquioxides. The most intense peaks at 379, 400, and 418 cm^{-1} for the Y_2O_3, the Tm:$YScO_3$ and the Tm:Sc_2O_3 were assigned to the F_g vibrations [169, 170] [cf. Fig. 5.10(b)]. The peaks corresponding to the maximum phonon energy (the F_g mode) were found at 594, 632, and 669 cm^{-1}, respectively.

5.3.2   Spectroscopy

Absorption cross sections

To evaluate the transparency and the GSA, a transmission spectrum was measured from UV to MIR range using a dual-beam UV/Vis/NIR spectrometer (Perkin Elmer, Lambda 1050) set to a resolution of 1 nm. Figure 5.11 shows the measured transmission spectrum of a 1.1 mm-thick Tm(2.2 at.%):$YScO_3$ which was annealed in reducing atmosphere. The background loss caused by the Fresnel reflection can be estimated to be $\approx 19\%$, indicating the refractive index ≈ 1.9. All peaks were identified to be the Tm^{3+} GSA lines. Among these GSA lines, 0.8 and 1.6 µm wavelength
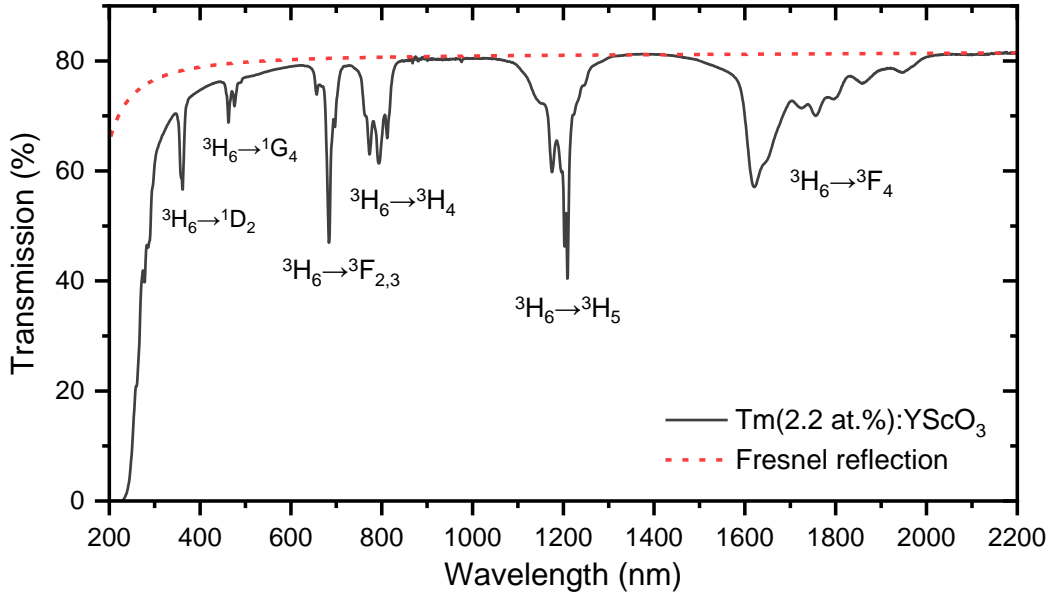
Figure 5.11: Transmission spectrum of the 1.1 mm-thick Tm(2.2 at.%):YScO$_3$ crystal.

range is interesting for efficient excitation to the $^3F_4$ manifold. Therefore, we measured temperature-dependent absorption spectra around the 0.8-μm and 1.6-μm bands. Transmission spectra of light emitted by a tungsten-halogen lamp through the crystal were measured at different temperatures. The wavelength selection of the transmitted light was performed with a monochromator (HORIBA, M1000) and the temperature of the sample was set by a closed-cycle helium cryostat (Advanced Research Systems, DE204). A photomultiplier tube (Hamamatsu, R5108) was used to measure the signal at wavelengths between 620 nm and 850 nm ($^3H_6 \rightarrow {}^3H_4$) and an InGaAs biased-detector (Thorlabs, DET10D2) was used for detection between 1450 nm and 2050 nm ($^3H_6 \rightarrow {}^3F_4$). From the transmission spectra, absorption spectra were calculated using the Beer-Lambert law:

$$I(\lambda, d) = I_0(\lambda)e^{-\alpha(\lambda)d}, \tag{5.4}$$

where I is the transmitted intensity, I_0 is the incident intensity, α and d are the absorption coefficient and the sample thickness, respectively. Thus, the absorption coefficient can be expressed as follows:

$$\alpha(\lambda) = \frac{1}{d} \cdot \ln \frac{I_0(\lambda)}{I(\lambda, d)}. \tag{5.5}$$

With the doping concentration N_{dop}, the absorption cross section can be determined as follows:

$$\sigma_{\text{abs}}(\lambda) = \frac{\alpha(\lambda)}{N_{\text{dop}}}. \tag{5.6}$$

Note that the cubic sesquioxides have 2 different cation sites and the C$_{3i}$ symmetry site is optically inactive (cf. Section 2.2.2). If Tm^{3+} ions were randomly distributed, 25% of the doped ions will not contribute to absorption and emission. However, in the mixed host material, the C$_{3i}$ inversion

symmetry could be partially broken by the disordered structure, and the transition will be partially allowed. In addition, the energy transfer rate between the C_2 and C_{3i} ions is not revealed. In this study, we calculated the absorption cross sections as an *effective* value for this doping level assuming that 100% Tm^{3+} ions contribute to optical transition, and emission cross section was calculated by Füchtbauer-Ladenburg equation (detailed in Section 5.3.2).

Figure 5.12 shows temperature-dependent absorption cross section of Tm(2.2 at.%):YScO$_3$. The absorption bands around 0.7 μm and 0.8 μm in Fig. 5.12(a) correspond to $^3H_6 \rightarrow {}^3F_{2,3}$ and $^3H_6 \rightarrow 3H_4$ transitions, respectively. Figure 5.12(b) shows $^3H_6 \rightarrow 3F_4$ transition. For all transitions, with decreasing temperature, the absorption cross section at longer wavelengths decreases owing to thermal depopulation of the upper Stark levels of the $^3H_6$ ground state manifold. On the other hand, the peak cross sections at shorter wavelengths increase and the bandwidth becomes narrower. The absorption spectra of $^3H_6 \rightarrow {}^3F_{2,3}$ transition have three prominent peaks at 300 K. With decreasing temperature, the peak around 695 nm decreases, on the contrary, the peak around 685 nm increases by a factor of 2. The 0.8 μm absorption band also has three prominent peaks at 300 K with peak cross sections of 2.5×10^{-21}, 2.8×10^{-21}, and 2.1×10^{-21} cm^2 at 773, 794, and 812 nm, respectively.
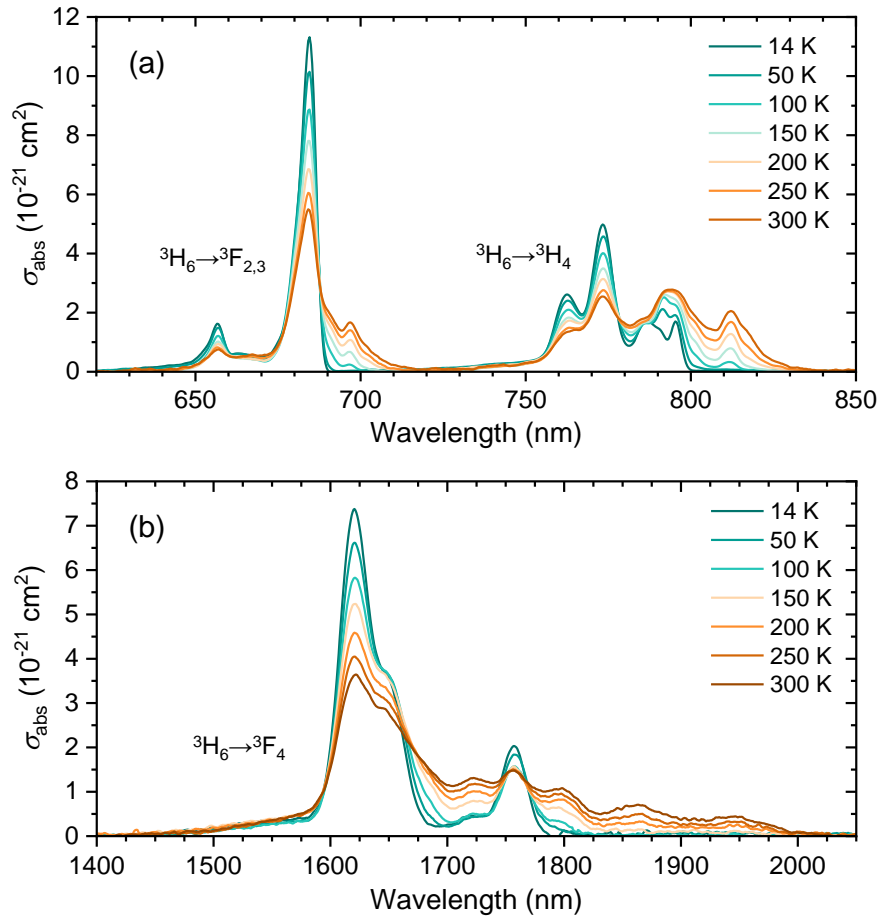
Figure 5.12: Temperature dependent absorption cross section of the Tm(2.2 at.%):YScO$_3$ crystal in (a) 800-nm (measured with a resolution of 1 nm) and (b) 1600-nm (measured with a resolution of 3 nm) ranges.

At lower temperatures, the peak at 812 nm decreases and completely disappeares at 14 K. The peak at 794 nm also decreases; however, it gradually splits into several peaks. The peak cross section at 773 nm increases by a factor of 2 and the shape becomes sharp at 14 K. For the absorption band around 1.6 μm seen in Fig. 5.12(b), the peak cross section amounts to 3.6×10^{-21} cm^2 at 300 K centered at 1620 nm. At 14 K, the peak cross section increases to 7.3×10^{-21} cm^2 while the spectral bandwidth reduces from ∼70 nm to ∼40 nm. The broad absorption bands even at 14 K evidence the inhomogeneous broadening caused by the disordered structure of the mixed sesquioxide host materials, as they are significantly broader than those of, e.g., Tm-doped Y_2O_3 at 40 K [171]. Although low-temperature spectroscopy is useful for the determination of energy levels, it is impossible to identify the peak positions corresponding to each Stark level in this case. Due to the inhomogeneous broadened nature, each energy level locates at a superposition of numerous energy levels corresponding to various crystal fields. Thus, the linewidth is broad even at 14 K and does not allow to identify individual Stark sublevels.

Figure 5.13 shows the room temperature absorption cross section of $Tm:YScO_3$ compared with that of $Tm:Y_2O_3$ and $Tm:Sc_2O_3$ [158]. The peak absorption wavelengths of $Tm:Y_2O_3$ and $Tm:Sc_2O_3$ are 1634 nm and 1611 nm, respectively. As expected, the peak absorption wavelength of $Tm:YScO_3$ is shifted between the values of $Tm:Y_2O_3$ and $Tm:Sc_2O_3$. The peak cross section is reduced by a factor of ∼2 compared with non-mixed sequioxides. These indicate *mixed* feature of these two host materials.
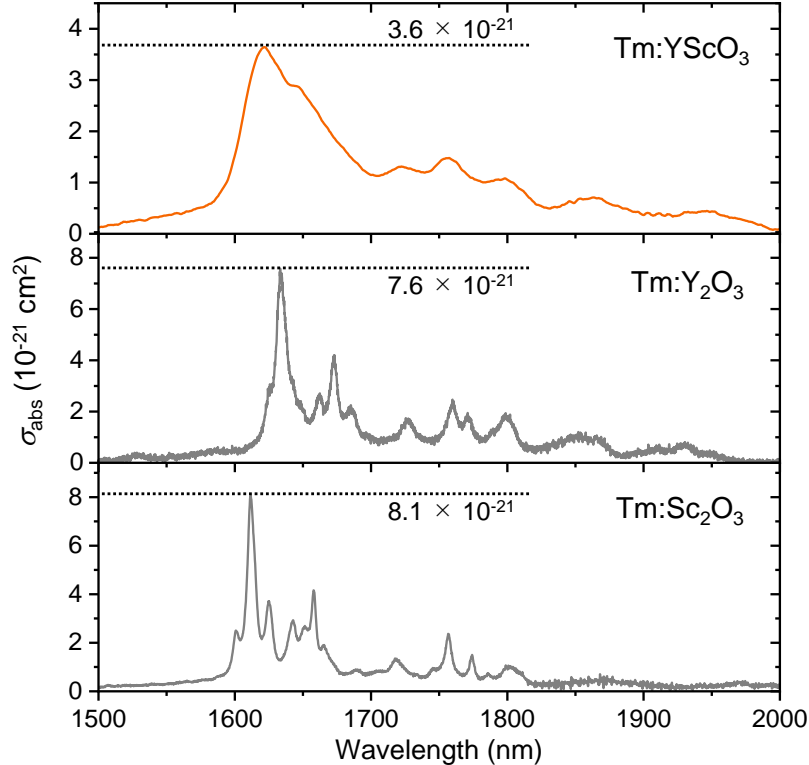
Figure 5.13: Absorption cross sections of $Tm:YScO_3$, $Tm:Y_2O_3$, and $Tm:Sc_2O_3$ [158] at room temperature.

Fluorescence lifetime

The temperature-dependent fluorescence lifetime of the $^3F_4$ manifold which contributes to 2 μm laser emission was measured. To measure the fluorescence lifetime precisely, the influence of radiation trapping needs to be reduced [172]. Radiation trapping due to the reabsorption resulting from the partial overlap of the emission and absorption spectra of Tm:YScO$_3$ at 2 μm [cf. Fig. 5.12(b) and 5.16]. We prepared a Tm(2.2 at.%):YScO$_3$ sample as thin as ≈270 μm for these measurements. The sample was excited by an optical parametric oscillator (OPO, GWU-Lasertechnik, versaScan) delivering 5-ns pulses at 10 Hz repetition rate. The excitation wavelength was chosen to be 1620 nm for in-band excitation to eliminate any influence of the population from further levels into the 2-μm emitting level. The fluorescence signal was detected by an InGaAs biased-detector and recorded by an oscilloscope. We measured the lifetimes at temperatures between 14 K and 300 K using the cryostat. In addition, to evaluate the residual influence of radiation trapping in the thin sample, the intrinsic lifetime was determined using the pinhole method [172, 173] at room temperature. For these measurements, a second sample thicker than 2.5 mm was prepared, and pinholes with different diameters between 0.8 mm and 2.5 mm were used to apply this method. Since the setup for the pinhole measurements is not compatible with the cryostat, we did not apply this method for the temperature-dependent lifetimes.
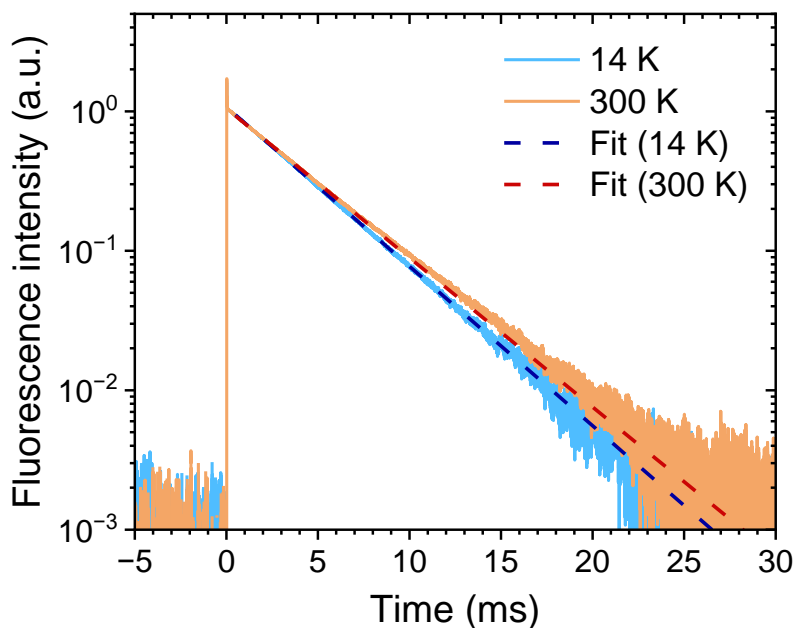
Figure 5.14: Fluorescence decay curve of the Tm(2.2 at.%):YScO$_3$ at 300 K (orange) and 14 K (blue) and fit curves for 300 K (red, dashed) and 14 K (dark blue, dashed).

Figure 5.14 shows the typical fluorescence decay curves on a semi-logarithmic scale measured using the thin sample at 14 K and 300 K. The narrow peak shortly after the excitation is caused by residual excitation light, which could not be completely blocked by a long-pass filter. The fluorescence lifetime was determined by fitting in the range between 0.5 ms to 5.0 ms after the excitation. A single-exponential decay curve was observed at 14 K. However, the decay curve at room temperature

slightly deviates from a single-exponential fit. This could be explained by the influence of activated energy migration between the optically active C_2 sites and the inversion symmetric and thus weakly optically active C_{3i} sites at higher temperatures [61]. Figure 5.15(a) shows the resulting temperature-dependent fluorescence lifetimes. The measured lifetime slightly decreased at lower temperatures.
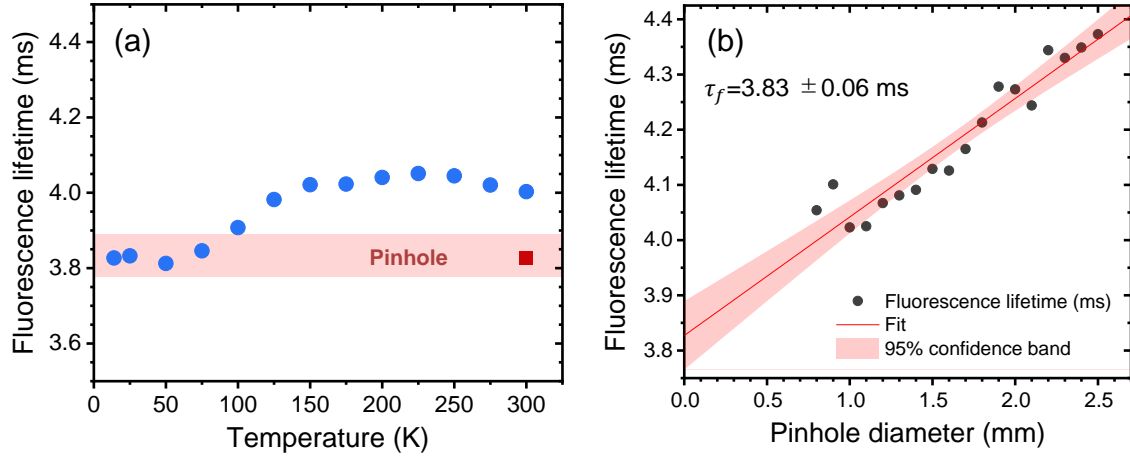
Figure 5.15: (a) Temperature-dependent fluorescence lifetime measured using the thin-sample (blue) and determined by the pinhole method (red). The red band indicates 95% confidence band of fit for the pinhole method. (b) Fluorescence lifetime measured using pinholes with different diameters.

In general, the fluorescence lifetime increases with decreasing temperature because thermally induced multiphonon fluorescence is suppressed at lower temperatures [174]. However, the measurements did not show this general trend. The fluorescence lifetime measured using the thin sample at room temperature amounts to 4.0 ms, which deviates only by $\approx 4\%$ from the room-temperature fluorescence lifetime of 3.83 ms determined by the pinhole method [cf. Fig. 5.15(b)]. While this indicates a fairly low influence of radiation trapping in the thin sample, the difference between the lifetimes at 300 K and 14 K found in Fig. 5.15(a) is on the same order as the influence of radiation trapping. Therefore, it was concluded that the variation with temperature is caused by the residual influence of radiation trapping, and there is no thermal quenching of the 2 µm emission at room temperature in Tm(2.2 at.%):YScO$_3$. This is explained by the sufficiently large energy gap between the $^3F_4$ manifold and the $^3H_6$ manifold estimated to be ≈ 4750 cm^{-1} from the longest-wavelength emission peak at 14 K (cf. Fig. 5.16): The comparably low maximum phonon energies of cubic sesquioxides (cf. YScO$_3$: ≈ 632 cm^{-1} (cf. Fig. 5.10), Y$_2$O$_3$: 592 cm^{-1}, Sc$_2$O$_3$: 669 cm^{-1} [169]) prohibit any significant non-radiative multi-phonon decay [39].

Emission and gain cross sections

The fluorescence spectra around 2000 nm corresponding to the $^3F_4 \rightarrow {}^3H_6$ transition of Tm^{3+} were measured using the monochromator, the InGaAs biased-detector, and the helium cryostat. The fluorescence spectra were measured in the wavelength range from 1600 to 2300 nm with a spectral resolution of 3 nm which was sufficient to resolve all spectral features. As an excitation source, a 780 nm LD with a spectral bandwidth of 1 nm (FWHM) was utilized. We used the ≈ 270 µm-thick

Tm(2.2%):YScO$_3$ sample to mitigate the influence of reabsorption on the fluorescence spectra. The stimulated emission cross sections σ_{em} can be calculated using the measured fluorescence spectra via the Füchtbauer-Ladenburg equation:

$$\sigma_{\mathrm{em}}(\lambda) = \frac{\lambda^5 I(\lambda)}{8\pi n^2 c \tau_{\mathrm{rad}} \int \lambda I(\lambda) d\lambda}, \tag{5.7}$$

where $I(\lambda)$ is the measured fluorescence intensity, n and τ_{rad} are the refractive index and the radiative lifetime, respectively. For n, we used the average refractive index of Y$_2$O$_3$ and Sc$_2$O$_3$. For τ_{rad}, we used the fluorescence lifetime of 3.83 ms which was derived above, assuming no temperature dependence and the non-radiative decay to be negligible on the ^{3}F$_4$→^{3}H$_4$ emission.
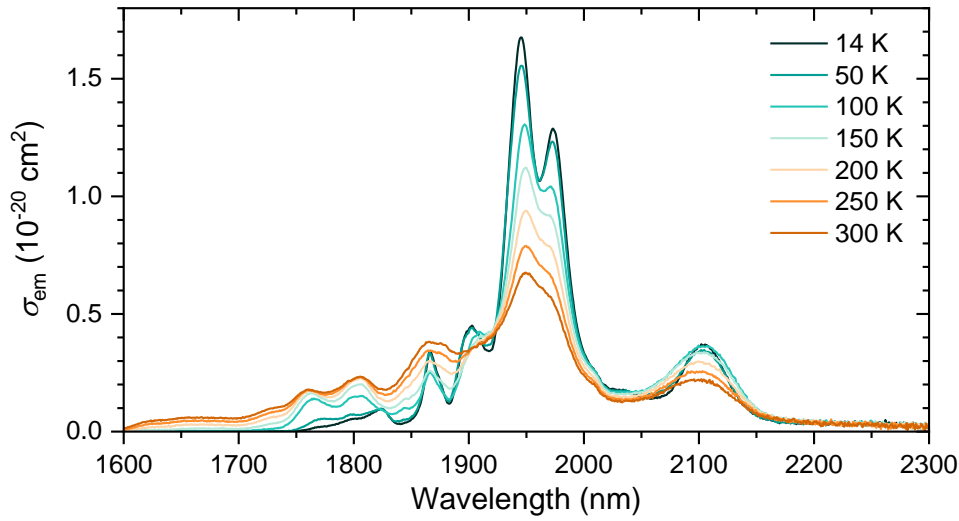
Figure 5.16: Temperature dependent emission cross section of the Tm(2.2 at.%):YScO$_3$ crystal.

Figure 5.16 shows the temperature-dependent emission cross sections. The emission peak values at 300 K are 6.8×10^{-21} cm^2 and 2.2×10^{-21} cm^2 at 1949 nm and 2099 nm, respectively. The corresponding spectral bandwidths of the peaks are 96 nm and 110 nm (FWHM). With decreasing temperature, the fluorescence peaks at shorter wavelengths decrease owing to the depopulation of the upper Stark levels of the ^{3}F$_4$ manifold. The peak emission cross sections increase to 1.7×10^{-20} cm^2 and 3.7×10^{-21} cm^2 at 1945 nm and 2103 nm, respectively, and the corresponding spectral bandwidths decrease to 54 nm and 52 nm at 14 K.

Figure 5.17 shows the room-temperature emission cross section compared with that of Tm:Y$_2$O$_3$ and Tm:Sc$_2$O$_3$. We can see that the emission peaks of Tm:YScO$_3$ are shifted to values in-between those of Tm:Y$_2$O$_3$ (1933 nm and 2048/2072 nm) and Tm:Sc$_2$O$_3$ (1972/1992 nm and 2115/2148 nm), again, indicating mixed feature. Here, compared with the pure sesquioxides, the spectra are less structured and the FWHM spectral bandwidth is broader even at low temperatures owing to inhomogeneous spectral broadening.
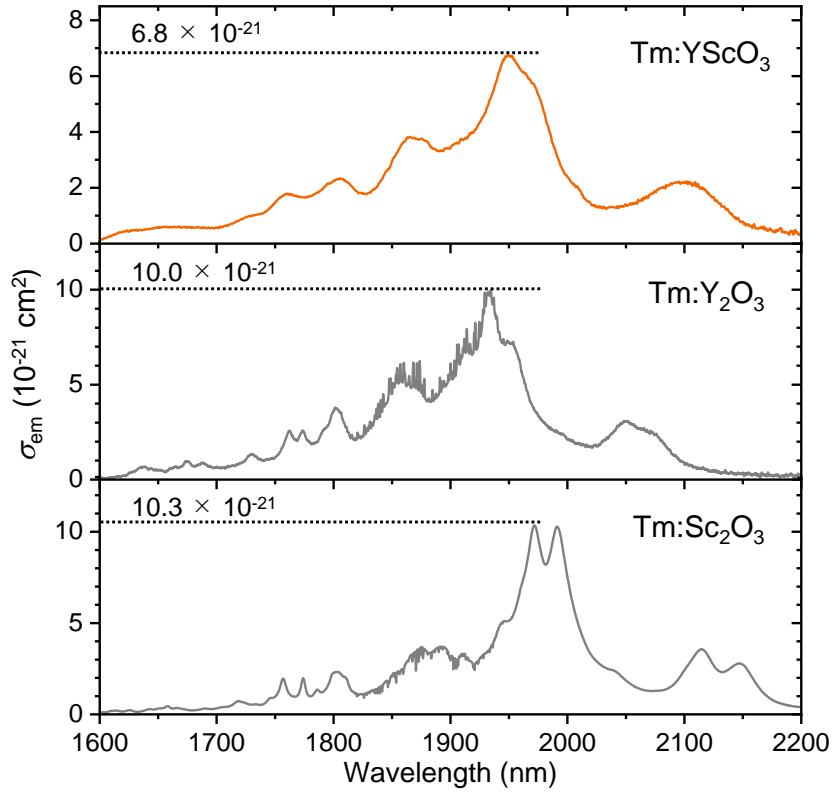
Figure 5.17: Emission cross sections of Tm:YScO$_3$, Tm:Y$_2$O$_3$, and Tm:Sc$_2$O$_3$ [158] at room temperature.

The gain cross sections σ_{gain} can be calculated using the following equation:

$$\sigma_{\text{gain}} = \beta\sigma_{\text{em}} - (1 - \beta)\sigma_{\text{abs}}. \tag{5.8}$$

Here, σ_{em} and σ_{abs} are the emission and absorption cross sections, and β is the inversion level which is the fraction of ions in the excited state:

$$\beta = \frac{N_2}{N_{\text{tot}}}, \tag{5.9}$$

determined with the density of excited ions N_2 and the total active ions N_{tot}. The calculated gain cross sections at 300 K for different inversion levels are shown in Fig. 5.18(a). The gain spectra exhibit a broad and flat profile. Particularly for low inversion levels, laser operation in the water-vapor-absorption-free range beyond 2000 nm is possible. This gain profile should enable broad wavelength tunability and support ultrashort pulse generation. Figure 5.18(c) shows the peak values of the gain cross sections with $\beta = 0.05$ at different temperatures. With decreasing temperature, the gain at the same inversion level is increased due to the higher emission cross sections. Moreover, the gain extends to wavelengths below 1850 nm owing to the reduced absorption in this range at lower temperatures [cf. Fig. 5.12], thus higher gain is found at shorter wavelengths. Figure 5.18(b) shows the gain cross sections at 100 K. Compared with the room temperature spectra, while the

gain increases, the spectra are still fairly broad and smooth. These features are interesting for ultrashort pulse amplification toward higher average and peak powers using the cryogenic amplifier technique. The cryogenically-cooled lasers and amplifiers benefit for increased thermal conductivity and higher gain cross sections [175]. However, ordered materials with homogeneous broadening exhibit the narrow gain bandwidth at lower temperatures, it does not support the amplification of fs-pulses because of the strong gain narrowing effect. Therefore, the inherent broad gain bandwidth of inhomogeneous broadened materials would work for cryogenically cooled ultrafast lasers and amplifiers.
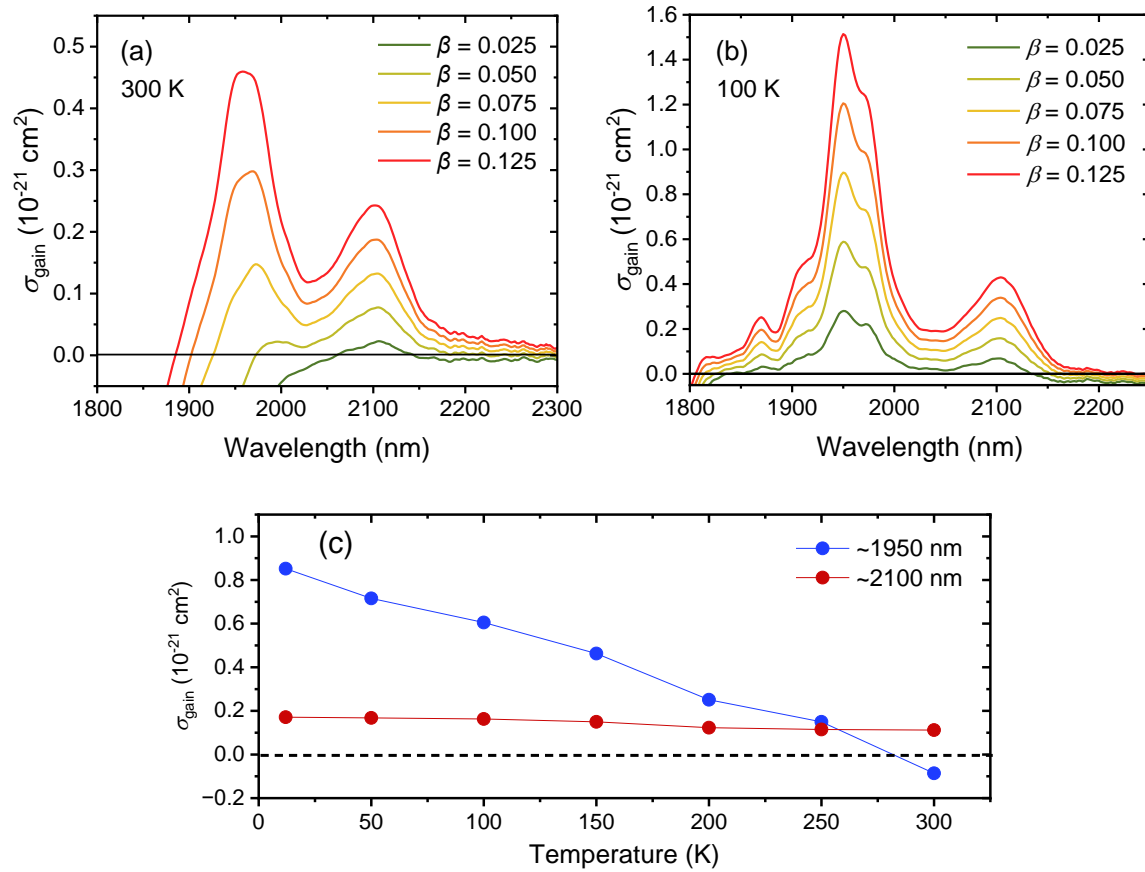
Figure 5.18: Gain cross sections of the Tm:YScO$_3$ at different inversion levels at (a) 300 K and (b) 100 K. (c) Peak value of the gain cross sections at different temperatures.

5.4   CW and wavelength tunable operation of Tm-doped mixed sesquioxide laser

5.4.1   780 nm LD pumped CW laser operation

Experimental setup

To explore the potential of Tm:YScO$_3$ for 2.1-µm laser operation, CW laser experiments were performed in a short laser resonator. The experimental setup is shown in Fig. 5.19. The linear cavity consists of a plane input coupler and a concave (R=50 mm) output coupler with a cavity length of 48 mm. As the gain media, a 6-mm thick Tm(2.2 at%):YScO$_3$ crystal and a 4-mm thick Tm(3.1 at.%):YScO$_3$ crystal, both remaining uncoated, were prepared. The crystals were mounted on water-cooled copper holders. We used a single-emitter C-mount LD with a maximum output power of 3 W at a operation wavelength around 780 nm (Roithner Lasertechnik GmbH, RLT785-4WC) as a pump source for two-for-one pumping. The LD has an emitter area of 200×1 µm^2 (sagittal×tangential), consequently, the beam quality factor M^2 is about 28 and 1 for the sagittal and tangential planes, respectively. The pump beam was shaped by a series of lenses and focused to 220×60 µm^2 on the gain medium. To characterize the laser performance, five different output couplers (OCs) with transmissions of 1.0%, 3.2%, 4.0%, 5.0%, and 8.7% were used.
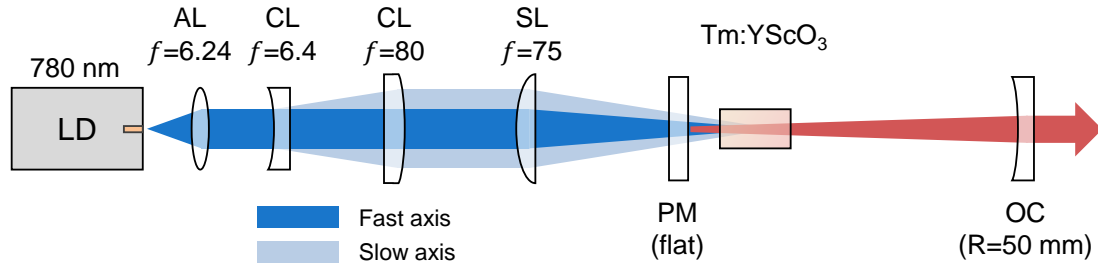
Figure 5.19: Experimental setup of the LD-pumped Tm:YScO$_3$ laser (LD: laser diode, AL: aspherical lens, CL: cylindrical lens, SL: spherical lens, PM: pump mirror, OC: output coupler).

The pump absorption varied depending on the incident pump power level because the operating wavelength of the LD changed from 775 nm to 777 nm with increasing power. Under lasing conditions, the corresponding pump absorption efficiency reduced from 63% to 57% for the 6-mm thick Tm(2.2 at.%):YScO$_3$ sample and from 60% to 53% for the 4-mm Tm(3.1 at.%):YScO$_3$ sample. The laser spectra were recorded using an upconversion spectrometer (NLIR, S2050-130-hr) with a spectral resolution of 4 cm^{-1}.

Results

Figure 5.20(a) shows the laser output power versus absorbed pump power of the Tm(2.2 at.%):YScO$_3$ laser with different OCs. Using the lowest OC transmission of 1.0%, laser operation was obtained at a threshold absorbed pump power of only 250 mW. With increasing OC transmission, the slope efficiency increased and the best value of 35% at a maximum output power of 500 mW was obtained using the 4.0% OC. For higher OC transmissions of 5.0% and 8.7%, the slope efficiency dropped. This trend of lower slope efficiencies with higher OCs is typical for solid-state lasers. That indicates the existence of inversion-dependent loss processes, however, the specific mechanism has not yet been revealed. Figure 5.20(b) shows the laser spectra of free running operations. For all OCs the laser wavelengths were centered around 2100 nm. The laser spectra exhibit distinct peaks in the emission range. However, not all of the peaks were resolved owing to the limited resolution of the spectrometer (resolution: 4cm^{-1}). This structured emission profile would be owed to etalon effects caused by the length of the plane-parallel crystal facets and their distance to the cavity components. In addition, this broad laser emission bandwidth is typical for lasers based on inhomogeneously broadened gain materials [90, 155]. The minor deviations are attributed to the particular coating of the OC mirrors used in these experiments. However, no shift of the emission wavelength to values below 2000 nm was observed, which indicates that the laser operated at moderate inversion levels below 7.5% in all experiments (cf. Fig. 5.18.)

Figure 5.20: (a) Laser characteristics and (b) free running laser spectra for different OCs of the Tm(2.2 at.%):YScO$_3$ laser under 780nm LD pumping.

Figures 5.21(a, b) show the output characteristics and the free running spectra of the Tm(3.1 at.%):YScO$_3$ laser. Using the lower transmission OCs, higher slope efficiencies were obtained compared with the Tm(2.2 at.%):YScO$_3$ laser. This is owed to a more pronounced cross relaxation induced by a closer average distance between the Tm^{3+} ions at the higher doping levels. The highest slope efficiency of 45% and the maximum output power of 422 mW were obtained using the 4.0% OC. The Stokes efficiency defined as the ratio of pump and laser photon energies was only

37%, hence the 45% slope efficiency evidences a quantum efficiency higher than unity enabled by the cross-relaxation process. However, in the higher doped crystal, the laser performance strongly degraded already with the 5.0% OC. Moreover, laser operation could not be obtained using the 8.7% OC. This may be explained by the closer average distance between excited ions also featuring detrimental energy transfer processes at high inversion levels. The center wavelengths were almost identical compared with the Tm(2.2 at.%):YScO$_3$ laser for each OC.

Figure 5.21: (a) Laser characteristics and (b) free running laser spectra for different OCs of the Tm(3.1 at.%):YScO$_3$ laser under 780nm LD pumping.

5.4.2 1650 nm LD pumped CW laser

To compare two-for-one pumping and in-band pumping scheme, 1650 nm LD pumped CW laser experiments were performed. We used the same cavity configuration as 780 nm LD pumped laser experiments [cf. Fig. 5.19]. As a gain medium, the 4-mm thick Tm(3.1 at.%):YScO$_3$ crystal was used. As a pump source, a single-emitter C-mount LD with a maximum output power of 3 W at an operation wavelength around 1650 nm (SemiNex, C-132) was utilized. The LD has an emitter area of 94×1 µm^2(sagittal×tangential), thus the beam quality is about 7.2 and 1 for the sagittal and tangential plane, respectively. The pump absorption efficiency under lasing conditions varied from 64% to 87% owing to the change of operating wavelength of the LD.

Figure 5.22 shows the laser output power versus absorbed pump power and free running laser spectra of the Tm(3.1 at.%):YScO$_3$ laser. In this experiment, because the output power of the 1650 nm LD fluctuated, the 2-µm laser output also fluctuated compared with 780 nm LD pumping. Using the 4.0% OC, the highest slope efficiency of 43% and a maximum output power of 771 mW were obtained. The laser wavelengths were almost identical to the previous results. Compared with 780 nm two-for-one pumping, a lower laser threshold was obtained due to better beam quality of the pump LD. Regarding the slope efficiency, Table 5.4 shows the comparison of the laser results between two-for-one and in-band pumping. Considering the stokes efficiency and maximum quantum

efficiency, the theoretical limit of laser efficiency for each pumping scheme is almost the same level and slope efficiencies experimentally obtained exhibit close values. This indicates sufficient cross relaxation was obtained in the two-for-one pumping scheme, and the laser performance seems to be mainly limited by the quality of the crystal, i.e. the strong internal stress in the crystal.
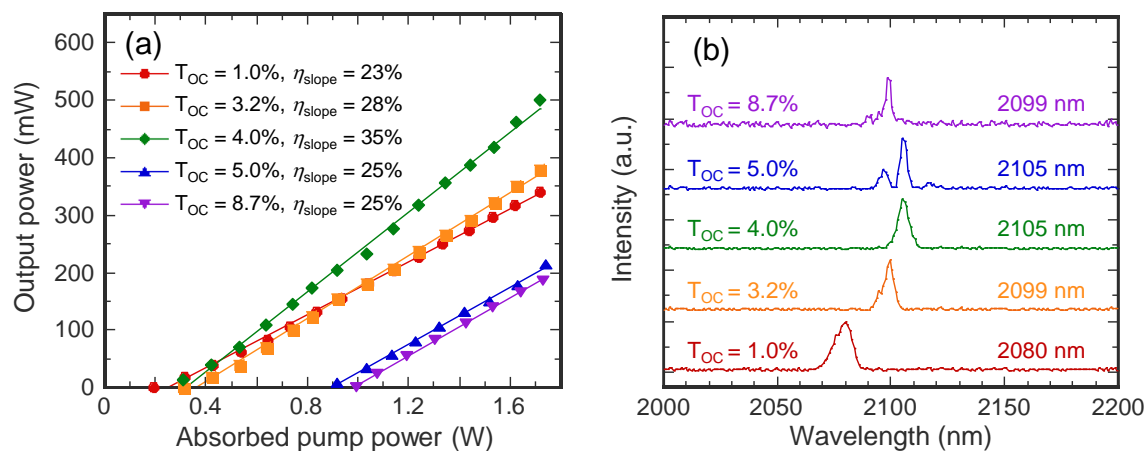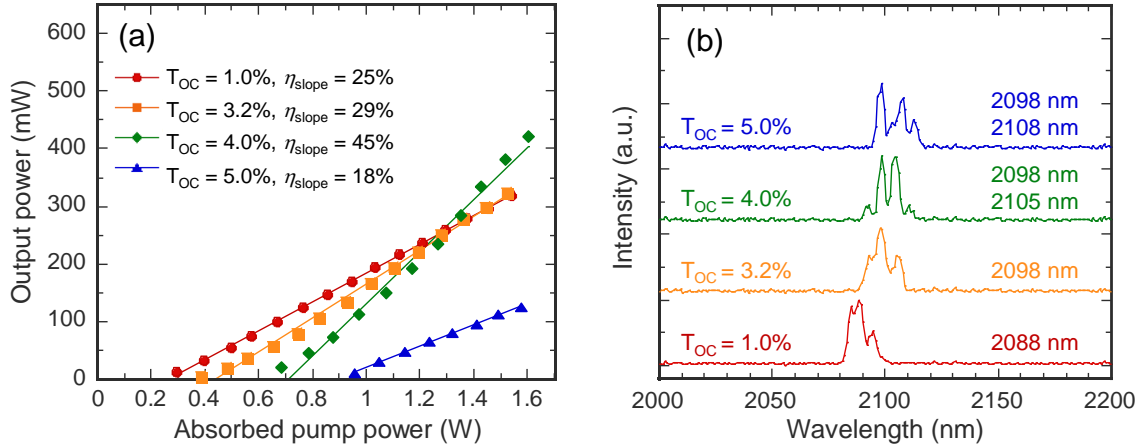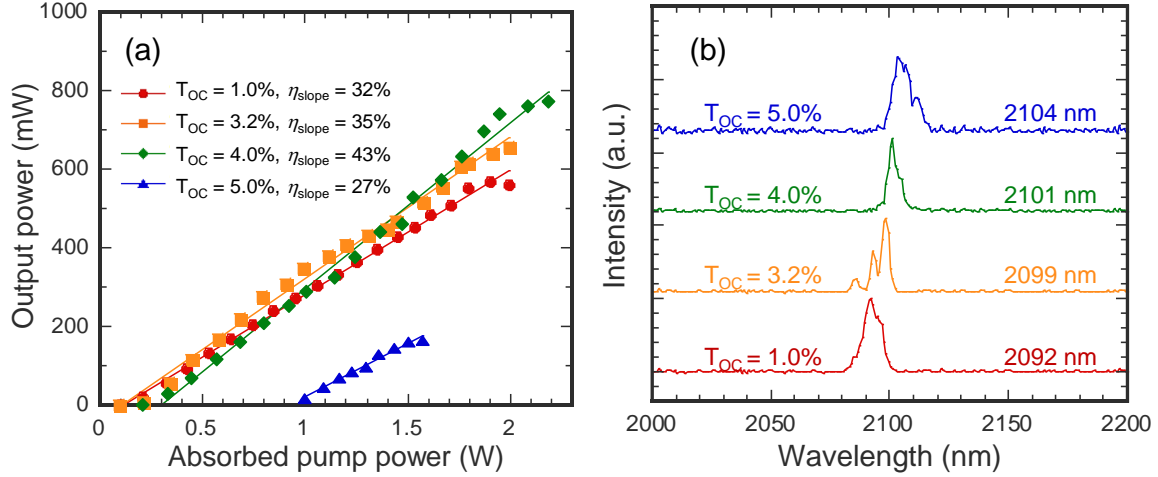

Figure 5.22: (a) Laser characteristics and (b) free running spectra for different OCs of the Tm(3.1 at.%):YScO$_3$ laser under 1650 nm LD pumping.

Table 5.4: Comparison of the laser efficiency between two-for-one and in-band pumping.

	η_{Stokes} (%)	η_{quantum}(max)	η_{limit} (%)	η_{slope} (max) (%)
two-for-one pumping	37	2	74	45
in-band pumping	78	1	78	43

5.4.3 790 nm high power LD pumped CW laser

To obtain higher laser output power, we demonstrate the laser experiments using high power LD emitting at 790 nm. The experimental setup is the same as previous experiments (cf. Fig. 5.19). As a pump source, a fiber-coupled LD with a maximum output power of 30 W at a wavelength of 790 nm (BWT, K793DA5RN-30.00W, core diameter: 105 μm, NA: 0.22) was utilized and the pump beam was focused on the gain medium using two lenses (f_1:f_2=30:50). As a gain medium, the 6mm-thick Tm(2.2 at.%):YScO$_3$ and the 4 mm-thick Tm(3.1 at.%):YScO$_3$ crystals were mounted on water-cooled (18 °C) copper holder. Using this configuration, lasing could be obtained, however, when the absorbed pump power increased above 4.5 W, the surface of the crystal was damaged for both crystals as shown in Fig. 5.23. This is owed to the poor thermal conductivity of this material [62]. Moreover, the thermal conductivity can be dramatically reduced depending on the quality of crystal, thus the above results imply that the quality of the as-grown crystals is still not perfect.
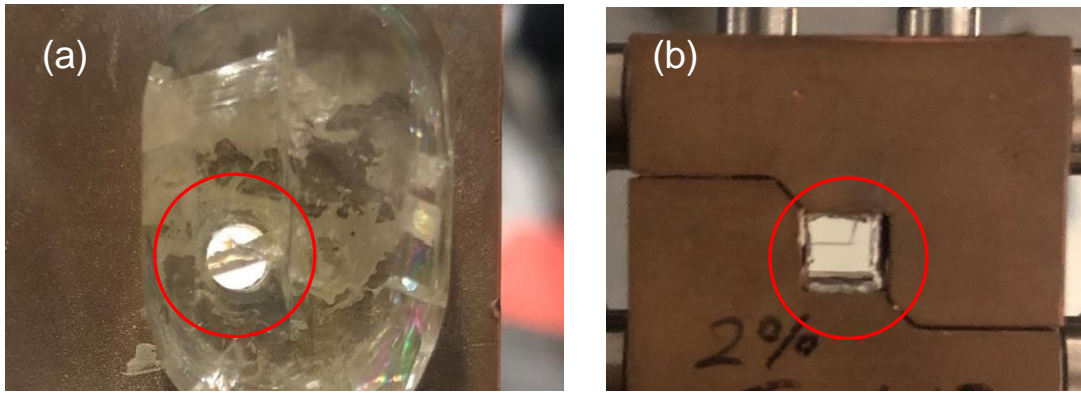
Figure 5.23: Damage on the surface of the Tm:YScO$_3$ crystals.

5.4.4   1611 nm Er:Yb pumped CW and wavelength tunable laser

Next, the CW laser experiments were performed using 1611 nm fiber laser with single-transverse mode output as a pump source. The experimental setup is shown in Fig. 5.24. As a gain medium, the 4-mm thick Tm(3.1 at.%):YScO$_3$ crystal was placed in the focus between two concave mirrors at Brewster's angle. In this configuration, polarization rotation in the crystal due to the strong internal stress causes losses at the gain medium and a prism because of Brewster's incident. By carefully adjusting the position of the crystal, lasing could be obtained.
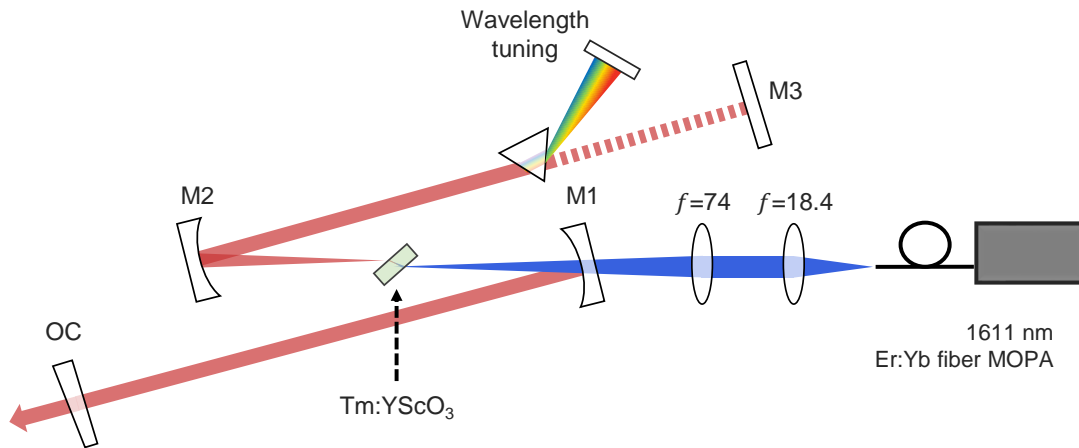
Figure 5.24: Experimental setup of the Tm:YScO$_3$ laser (M1,M2: curved mirrors (R=100 mm), M3: a flat high reflective mirror, OC: a wedged output coupler). For CW laser operation, dashed beam path was used.

Figure 5.25 shows the output characteristics of the CW laser operation. As increasing pumping power, the output power was linearly increased. However, due to thermal load, the output power was saturated at the absorbed pump power of above ≈1.2 W which corresponding to the region highlighted in Fig. 5.25(a). The slope efficiencies were derived by omitting the saturated region. A maximum output power of 568 mW was obtained using a 3.0% OC and a maximum slope efficiency of 51% was achieved using a 5.0% OC. A 9.0% OC was also tried, however, lasing could not be obtained.

The laser wavelengths shown in Fig. 5.25(b) were blue shifted as increasing output coupling, this is typical for quasi-three level lasers.

In this experiment, the good beam quality of the pump fiber laser enabled better mode matching between pump and laser mode in the gain medium, resulting in higher slope efficiencies compared with LD pumped experiments. The maximum output power was limited by thermal load owing to insufficient cooling efficiency. This problem can be solved by using the appropriate crystal holder.
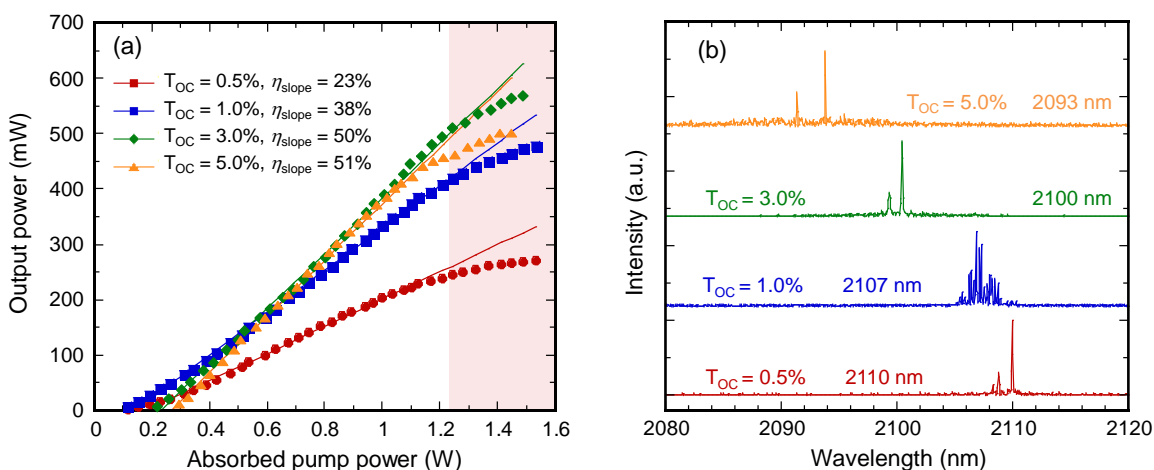
Figure 5.25: (a) Laser characteristics and (b) free running laser spectra of the 1611 nm Er:Yb fiber pumped Tm(3.1 at.%):YScO$_3$ laser using 1.0% OC.
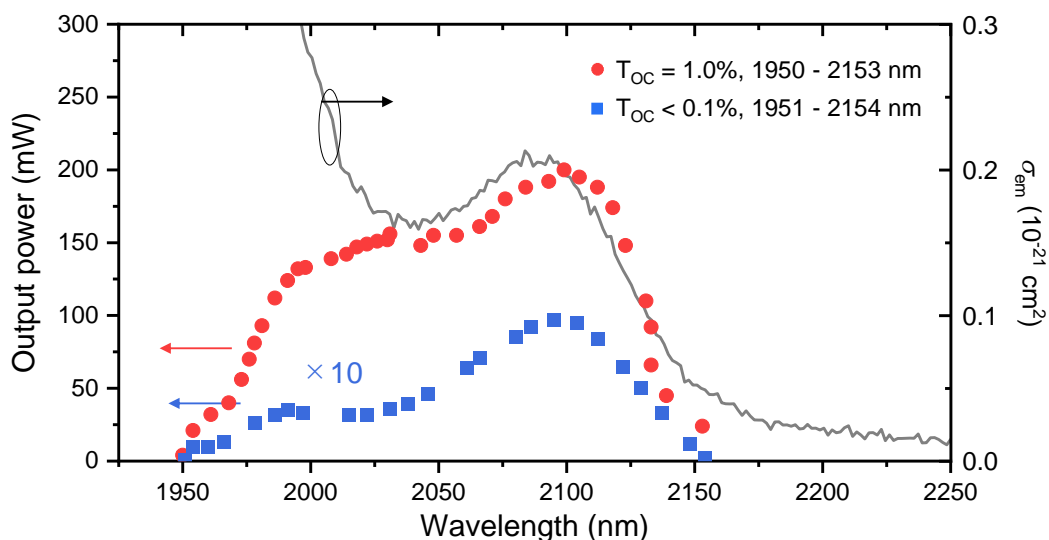
Figure 5.26: Wavelength tunability of the Tm:YScO$_3$ laser using the 1.0% OC and the high reflector as OC (R>99.9%). The grey curve shows the fluorescence spectrum of the Tm:YScO$_3$ on a semi-logarithmic scale.

Inserting a prism into the cavity arm, wavelength tunability was measured using 1.0% and <0.1% OCs. The wavelength tunnability is shown in Fig. 5.26. For both OC, the tuning range of 203 nm from 1950 to 2153 nm was obtained. Tuning to shorter wavelengths is limited by the specific coating of the cavity mirror. For the longer wavelengths, referring to the emission cross section spectrum of Tm:YScO$_3$ (5.26), we can see the fluorescence tail expanding to longer wavelengths, i.e. there is some gain at these wavelengths. Moreover, we confirmed the extended tuning range with low transmittance OC in the combined gain laser (cf. Section 4.2). However, we could not reach longer wavelengths using the Tm:YScO$_3$. Here, it seems to be limited by the losses in the crystal.

5.5   Kerr-lens mode-locked Tm:YScO$_3$ laser

KLM experiments were performed using the Tm(3.1 at.%):YScO$_3$ crystal and the same cavity configuration as the in-band pumped CW laser experiment using E:Yb fiber MOPA (cf. Fig. 5.24). The total cavity dispersion amounted to $\sim$-1315 fs^2, resulting from -975 fs^2 due to chirped mirrors and $\sim$-340 fs^2 in the Tm:YScO$_3$ crystal. Using a 1.0% OC, KLM operation was initiated by moving the M2 mirror in Fig. 5.24. Figure 5.27 (a) shows the average output power as a function of absorbed pump power. When KLM operation started, the average output power was significantly increased, and a maximum average output power of 112 mW was obtained at an absorbed pump power of 0.6 W. Figure 5.27 (b) shows the optical spectrum of the mode-locked pulses. The sech^2-shaped spectrum exhibits a spectral bandwidth of 64 nm at the center wavelength of 2130 nm. The output pulses were compressed by 1-mm thick Si (GDD$\sim$+770 fs^2), and the pulse duration was measured to be 73 fs by SHG intensity autocorrelation [Fig. 5.27 (c)]. A repetition rate was 96.9 MHz, thus the corresponding pulse energy and peak power were 1.2 nJ and 15.4 kW, respectively.
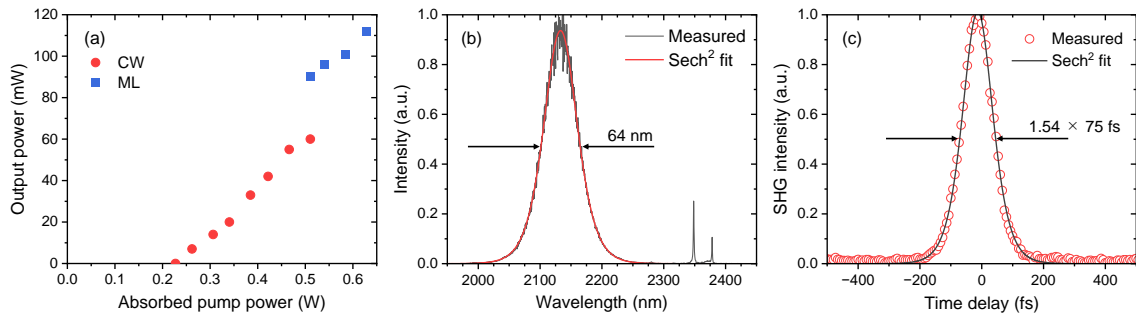
Figure 5.27: (a) Average output power and (b) optical spectrum of the KLM Tm(3.1 at.%):YScO$_3$ laser using the 1.0% OC. (c) SHG intensity autocorrelation trace after compression.

Next, we replaced the OC with 0.5% one remaining the cavity GDD. KLM operation was obtained with a maximum output power of 100 mW at an absorbed pump power of 0.58 W (Fig. 5.28). The center wavelength is 2130 nm with a spectral bandwidth of 85 nm. Here, the additional spectral components were observed from 2250 to 2350 nm. These components should be caused by intracavity SRS process (cf. Section 4.3) since the intracavity peak power increased from 1.54 MW to 3.57 MW compared with the prior experiment using the 1.0% OC. While the calculated transform-limited pulse duration is 39 fs, the SHG intensity autocorrelation indicates the pulse duration of 58 fs assuming

sech^2 pulses as shown in Fig. 5.28 (c). For a more accurate evaluation, FROG measurement is needed to check the phase of optical pulses with such a highly structured spectrum.
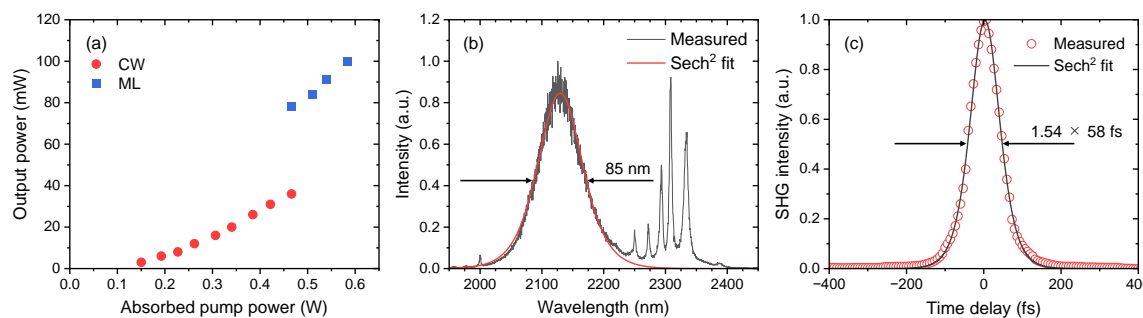
Figure 5.28: (a) Average output power and (b) optical spectrum of the KLM Tm(3.1 at.%):YScO$_3$ laser using the 0.5% OC. (c) SHG intensity autocorrelation trace after compression.

To confirm the stability, we measured RF spectra as shown in Fig. 5.29. A high S/N ratio of more than 60 dBc was observed at the fundamental repetition rate of 96.7 MHz, indicating stable single-pulse mode-locked operation.
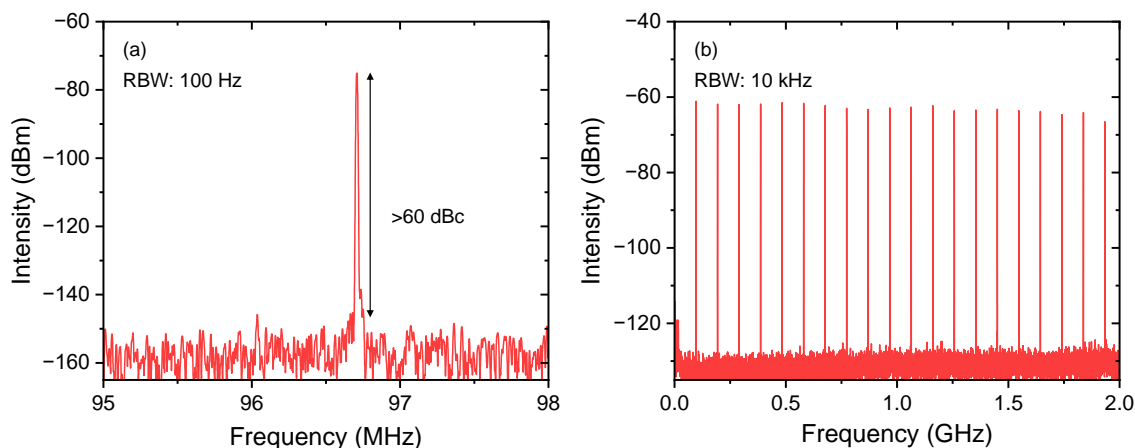
Figure 5.29: RF spectra in (a) 3 MHZ and (b) 2 GHz span range.

5.6 Discussion

5.6.1 Limiting factor of laser performance

The presented laser efficiencies are higher than those obtained with any Tm-doped mixed sesquioxide ceramic lasers [176, 158], but they fall behind the slope efficiencies of 55% and 59% obtained with Tm:LuScO$_3$ and Tm:Lu$_2$O$_3$ crystals, respectively. We attribute this to the strong internal stress in the crystal. In addition, high-power laser operation is limited in the 30 W-LD pumping and Er:Yb fiber MOPA pumped laser experiments due to high thermal load. This is owed to the poor thermal conductivity of this material and it was even aggravated due to the imperfect quality of the crystal. To improve the quality of the as-grown crystal, there is still room for improvement for growth setups

and parameters such as rotation speed, pulling rate, cooling time, and so on. In addition, there may be the influence of the existence of perovskite phase at lower temperatures. Generally, such an influence is negligible because the phase transition temperature is more than $400°C$ lower than the melting point [177]. However, the transition temperature of $\sim 1700°C$ is sufficiently high compared with the melting temperature of other oxide materials, thus it may allow the solid-state reaction to occur. Therefore, during cooling after the growth, if atoms in the crystal have activation energy to try to change the phase of the crystal, it may introduce stress to the crystal.

5.7 Summary

In this chapter, we demonstrated the crystal growth of the novel Tm-doped mixed sesquioxide $YScO_3$ and investigations of the spectroscopic properties and the laser characteristics. Cubic centimeter-scale laser-quality crystals were grown by the Cz method from Ir crucibles for the first time. In temperature-dependent spectroscopic investigations, we confirmed the absence of non-radiative relaxation processes from the upper laser level in a $Tm(2.2\%)$-doped $YScO_3$ crystal. The disordered nature of the mixed sesquioxide host matrix features broadening of the absorption, which facilitates diode pumping. The corresponding broad and flat emission spectrum extending above 2 µm is promising for the ultrashort pulse generation in mode-locked laser operation. In addition, due to the inhomogeneous broadening mechanism, the spectral bandwidth remains broad even at cryogenic temperatures. This indicates that $Tm:YScO_3$ is a suitable host material for the generation of ultrashort pulses with high average and/or peak power using cryogenic amplifier technology. Finally, we demonstrated the first $Tm:YScO_3$ laser operations. Slope efficiencies of up to 51% were achieved using a $Tm(3.1 \text{ at.}\%):YScO_3$ crystal under 1611 nm Er:Yb fiber MOPA pumping. In KLM experiments, pulses as short as 58 fs were obtained at the center wavelength of 2130 nm. The laser experiments show that Tm-doped mixed sesquioxide crystals have a huge potential for highly efficient and ultrafast lasers in the water-vapor-absorption free 2.1-µm wavelength range. The possibility to grow these materials by the Czochralski method is an important step toward the future commercial availability of mixed sesquioxides.

Chapter 6

Conclusion and outlook

6.1 Conclusion

In this thesis, to achieve high-power ultrashort pulse generation overcoming the conventional gain bandwidth limitation, the novel gain configurations for the 2 µm Tm laser system were proposed. The use of combined gain media makes the effective gain spectrum broader as the linear combination of both gain bands enables a broad gain spectrum as well as a flat profile. Mixed gain material consists of a mixture of different host materials, resulting in a broad and flat gain spectrum caused by inhomogeneous spectral broadening effect owing to the influence of various crystal field. The basic idea is common for both methods to obtain broad and smooth gain profiles using different materials simultaneously.

In the first experiment, we performed the combined gain CW and KLM lasers using the Tm:Lu$_2$O$_3$ ceramic and Tm:Sc$_2$O$_3$ single crystal. We revealed that the effective gain profile changes depending on the combination of each gain medium and its contributions. Interestingly, gain saturation in the combined gain media will occur inhomogeneously depending on the laser wavelength, thus the saturation intensity is an important parameter for the selection of gain materials. In the CW laser experiments, wavelength tuning from 1962 nm to 2252 nm resulted in 353 nm tuning range. In the KLM experiments, high average power operation was achieved using a 3.0% OC with the highest average output power of 316 mW at a pulse duration of 73 fs. For further shorter pulse generation, I constructed a high-Q-factor cavity using a 0.5% OC, and the shortest pulse duration of 41 fs corresponding to 5.9 optical cycles was achieved. This result represents the shortest pulse duration reported for any Tm-based mode-locked lasers in the 2 µm wavelength range. This is owed to the broadband gain and the flat gain profile adjusted by the proper combinations of gain materials with the suitable doping concentration and the pumping condition. Moreover, the broadened spectrum exceeding the gain bandwidth limitation assisted by intracavity SRS would contribute to further pulse shortening. The large modulation depth of KLM enabled to sustain mode-locked operation with anomalous spectral broadening using intracavity nonlinear effect.

In the second experiment, the Cz growth of Tm-doped mixed sesquioxide crystal was demonstrated for the first time. Spectroscopic investigations revealed the inhomogeneously broadened spectra which indicate suitability for ultrafast laser applications. Moreover, we achieved highly effi-

cient laser operation and KLM laser operation using as-grown single crystals. These results indicate the huge potential of mixed sesquioxide for highly efficient ultrafast lasers and the future commercial availability of this material.

6.2 Comparison between combined gain and mixed material

In this section, I discuss the features and advantages of the combined gain Tm-doped sesquioxides and Tm-mixed sesquioxides. Table 6.1 summarizes the characteristics of the combined gain media and mixed sesquioxides. In conclusion, combined gain media is superior to mixed materials in terms of the feasibility of broad gain bandwidth and excellent thermo-mechanical properties for ultimate laser performance. Considering the emission cross section spectra, the effective gain of combined gain media is a linear combination of two gain spectra, while the mixed material shows the intermediate characteristics of two host materials due to an "averaging" effect. In the Tm-doped cubic sesquiox-ides, $Tm:Sc_2O_3$ exhibits a gain band at further longer wavelengths from $Tm:Y_2O_3$ and $Tm:Lu_2O_3$ owing to the strongest crystal field among these materials. Thus the use of Sc_2O_3 benefits both methods to broaden the gain band since the gain at longer wavelengths is desirable to avoid strong water-vapor-absorption in the shorter wavelength range in Tm emission wavelengths. While the effective gain of mixed sesquioxide somewhat sacrifices the gain at longer wavelengths because of the "averaging" effect, the combined gain media do not suffer. In addition, the mixed materials and other single-gain media have defined spectral profiles, however, the combined gain media enables us to actively control the effective gain profile by adjusting pump intensity, the balance of doping concentration, the thickness of gain media, and so on. Moreover, inhomogeneous gain saturation in the combined gain media can support spectral broadening in the mode-locked laser oscillator, while the mixed materials exhibit (almost) homogeneous gain saturation as the homogeneous width of the transition line of each site is sufficiently broad. The design of the gain profile is also attractive for the power amplifiers. Generally, in laser amplifiers, the gain narrowing effect is the bottleneck for the achievable pulse duration. As a measure against the gain narrowing, the spectral filter has been generally used [178, 179], i.e. gain profile is controlled by the additional loss. On the contrary, combined gain media can manage it without any additional losses. In addition, combined gain media can utilize high thermal conductivity, which is also ideal for high-power lasers and amplifiers. The poor thermo-mechanical properties of mixed materials are actually not suitable for high-power laser applications lat the tens-hundreds W level.

Considering the cryogenic laser technology, improved thermo-mechanical properties and increased gain cross section would be useful for high-power laser operation. Since combined gain media consist of homogeneous broadened materials, it cannot sustain short pulse duration at low temperatures because of narrow gain bandwidth at cryo-temperatures. However, inhomogeneous spectral broad-ening in the mixed materials should support short pulse duration even at cryo-temperatures. At room-temperature, mixed materials show reduced thermal conductivities, however, it is improved at low temperatures [62]. Therefore, mixed material may be useful for cryogenic ultrafast lasers.

Combined gain media should have a problem regarding the preparation of high-quality laser materials. As the laser performance is strongly influenced by the quality of the gain material, high-quality sesquioxides are required to realize the best performance with combined gain media.

However, extremely high melting temperatures of sesquioxides make high-quality large-size crystal growth significantly challenging. Of cause, ceramics are a good choice as the host material, but the laser efficiencies fall somewhat behind compared with single crystal lasers. On the other hand, the mixed sesquioxides can be grown by the conventional Cz growth from iridium crucibles and they exhibit desirable spectroscopic properties for mode-locked lasers. Although the mixed sesquioxides grown in this study are still prototypes, but by improving the crystal growth, mixed sesquioxide would be commercially available host material like YAG or YLF, especially suitable for ultrafast laser oscillators.

Table 6.1: Comparison between combined Tm-doped sesquioxides and Tm-doped mixed sesquioxides.

	Combined gain	Mixed sesquioxides
Gain bandwidth	broad	broad
Type of broadening	homogeneous	inhomogeneous
Gain saturation	inhomogeneous	(almost) homogeneous
Gain profile	controllable	flat
Cross sections	remain	reduced
Gain spectra at lower temperatures	narrow, highly structured	broad, less-structured
Thermal conductivity	high	low
Melting temperature	>2350°C	~2100-2450°C
Laser materials	HEM-grown crystal ceramic	Cz-grown crystal ceramic

6.3   Outlook

The interest of two methods proposed in this thesis is to enable the design of the gain profile of laser materials. In conventional laser materials, optical properties are inherently defined by the dopant ions and host materials. However, combined gain media enables broadening the gain bandwidth and designing the shape of effective gain, and mixed sesquioxides enable tuning the peak emission wavelength by changing the compositions. Therefore, combining or mixing different materials enable variable parameter to optimize effective spectra as needed.

Combined gain media is a universal method as it is applicable for other wavelengths and any type of laser configuration such as the bulk configuration, thin-disk, and monolithic lasers. Since combined gain media exhibits broad gain bandwidth as well as superior thermo-mechanical properties, thin-disk laser configuration is a very reasonable choice for high-power ultrafast lasers. For another scheme, using composite technology, combined gain monolithic laser enables broad gain bandwidth and a high repetition rate. Since the intracavity spectral combining in the combined gain oscillator does not need spatial combining of both materials, there is flexibility for cavity configuration. For example, it is possible to independently pump gain materials using different pumping sources, which makes further flexibility for effective gain control by choosing the pump wavelength and/or balance of pump intensity.

Mixed sesquioxides are superior materials especially for mode-locked laser oscillators due to their broad and flat gain profile. Besides, owing to their reduced melting temperatures, the growth of large-size high-quality crystals by Cz-growth can be available. Currently, the improvement of crystal growth is the most important subject. The strong internal stress affects the losses in the lasers and aggravates the thermal property. In addition, the observed spiral formation should be an obstacle to size scaling. To improve this, understanding the growth dynamics of mixed-sesquioxides is very important to find a way to mitigate the stress as well as growth instabilities. Therefore, $YScO_3$ is a promising candidate for future commercially available laser host material in terms of cost, and excellent optical properties for ultrafast lasers.

These techniques to realize broad and flat gain profiles are essential to achieve high-average power and shorter pulse durations. I believe that the combined gain media and mixed materials would be innovative technologies to achieve tens of W-scale sub-100-fs pulse generation in the 2 μm laser oscillators.

Appendix A

References for Table 2.2

Table A.1: List of references for table 2.2.

	Lu_2O_3	Sc_2O_3	Y_2O_3	$LuScO_3$	$LuYO_3$	$YScO_3$	$Y_3Al_5O_{12}$
Acronym	-	-	-	-	-	-	-
Lattice structure	[180]	[180]	[180]	[181]	[155]	[148]	[182]
Space group	[180]	[180]	[180]	[181]			[182]
Site symmetry	[180]	[180]	[180]				[183]
Cation radius (Å)	[183]	[183]	[183]	average	average	average	[183]
Lattice constant (Å)	[184]	[184]	[184]	[61]		this work	[185]
Cation density $(10^{22}$ cm$^{-3})$	[184]	[184]	[184]	average	average	average	[185]
Density (g cm^{-3})	[184]	[184]	[184]	average	average	average	[186]
Melting point (°C)	[46]	[46]	[46]	[63]	[62]	[62]	[187]
Refractive index at 2 μm	[46]	[46]	[46]				[188]
Transparency range (μm)	[189]	[79]	[79]	[189]			[186]
Thermal conductivity (W m^{-1}K^{-1})	[61]	[189]	[189]	[63]		[161]	[190]
Thermo-optic coeff. $\frac{dn}{dT}$ $(10^{-6}$K)	[191]	[192]	[193]			[161]	[190]
Thermal expansion coeff. $\frac{1}{L}\frac{dL}{dT}$ $(10^{-6}$K)	[184]	[184]	[194]				[190]
Max. phonon energy (cm^{-1})	[169]	[169]	[169]		[99]	this work	[195]

Appendix B

Excited state absorption of Tm:YScO$_3$

To identify the transition channel from the excited state in Tm:YScO$_3$, we measured excited state absorption (ESA) in the near-infrared range from 930 nm to 1550 nm. Since ESA is absorption from the metastable excited state, the measurement was performed using the pump-probe technique with a double modulation scheme following Ref.[196]. As a sample, a Tm(2.2 at.%):YScO$_3$ was used. The pump sources were the 790 nm, and 1650 nm LDs to excite ions into the ^{3}H$_4$ and ^{3}F$_4$ manifold, respectively.
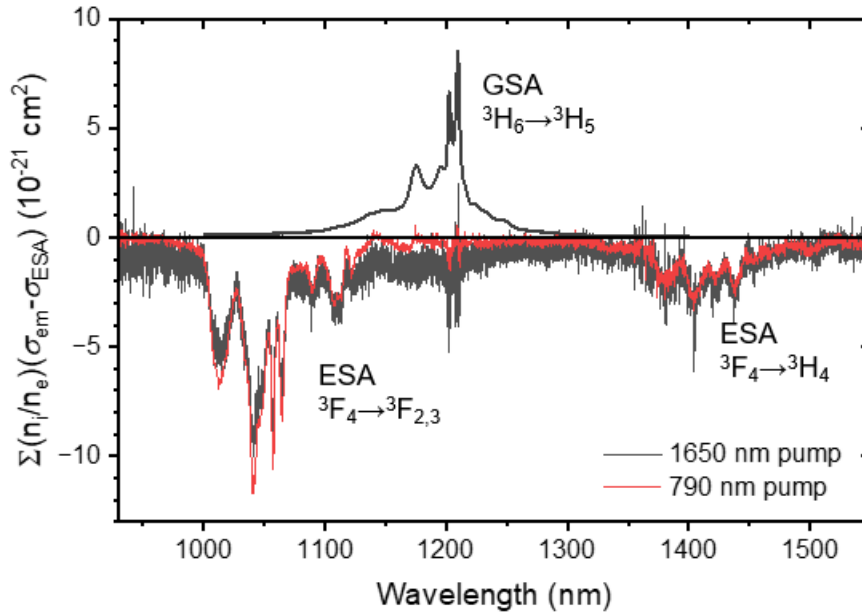
Figure B.1: ESA spectra of Tm:YScO$_3$ under 790 nm(red) and 1650 nm(black) pumping.

Figure B.1 shows the ESA and GSA spectra of Tm:YScO$_3$. The cross section was calculated according to Ref.[196]. ESA transitions corresponding to ^{3}F$_4$→^{3}H$_4$ and ^{3}F$_4$→^{3}F$_{2,3}$ were obseved.

The peak cross sections were $\approx 11 \times 10^{-21}$ and $\approx 3 \times 10^{-21}$ cm^2 at 1040 nm and 1404 nm, respectively. In this wavelength range, the ESA transition ^{3}H$_4 \rightarrow$^{1}G$_4$ ($\sim$1100 nm) would be observed under 790 nm pumping. However, in the measurement, it was not observed (cf. Fig. B.1). This is owed to efficient cross relaxation process that depopulated the ^{3}H$_4$ and populated to the ^{3}F$_4$ at this doping level. This should evidence the nearly identical ESA spectra observed under 790 nm and 1650 nm pumping. This is consistent with the absence of fluorescence from the ^{3}H$_4$ manifold under 780 nm pumping (cf. 5.16).

References

[1] K. van Dalfsen, S. Aravazhi, C. Grivas, S. M. García-Blanco, and M. Pollnau. "Thulium channel waveguide laser with 1.6 W of output power and 80% slope efficiency". *Opt. Lett.*, 39:4380–4383, 2014.

[2] Thomas Ehrenreich, Ryan Leveille, Imtiaz Majid, and Kanishka Tankala. "1 kW, all-glass Tm:fiber laser". *SPIE Photonics West 2010:LASE, Fibre Lasers VII: Technology, Systems and Applications*, 7850, 2010.

[3] Stuart D. Jackson. "Towards high-power mid-infrared emission from a fibre laser". *Nat. photonics*, 6:423–431, 2012.

[4] Yefei Mao, Yuan Gao, and Lei Wang. "254W laser-diode dual-end-pumped Tm:YAP InnoSlab laser". *Appl. Opt.*, 59:8224–8227, 2020.

[5] Julian Schneider, Patrick Forster, Clément Romano, Marc Eichhorn, and Christelle Kieleck. "Investigation of the pulse energy limits of actively Q-switched polarization-maintaining Tm^{3+}-doped fiber lasers". *OSA Continuum*, 4:1577–1586, 2021.

[6] Masaki Yumoto, Norihito Saito, Yoshiharu Urata, and Satoshi Wada. "128 mj/pulse, laser-diode-pumped, Q-switched Tm:YAG laser". *IEEE J. Sel. Top.Quantum Electron.*, 21:364–368, 2015.

[7] Bujin Guo, Y. Wang, C. Peng, H. L. Zhang, G. P. Luo, H. Q. Le, C. Gmachl, D. L. Sivco, M. L. Peabody, and A.Y. Cho. "Laser-based mid-infrared reflectance imaging of biological tissues". *Opt. Express*, 12:208–219, 2004.

[8] Christian Rosenberg Petersen, Nikola Prtljaga, Mark Farries, Jon Ward, Bruce Napier, Gavin Rhys Lloyd, Jayakrupakar Nallala, Nick Stone, and Ole Bang. "Mid-infrared multispectral tissue imaging using a chalcogenide fiber supercontinuum source". *Opt. Lett.*, 43:999–1002, 2018.

[9] Delong Zhang, Chen Li, Chi Zhang, Mikhail N. Slipchenko, Gregory Eakins, and Ji-Xin Cheng. "Depth-resolved mid-infrared photothermal imaging of living cells and organisms with submicrometer spatial resolution". *Science Advances*, 2:e1600521, 2016.

[10] Daniel Popa and Florin Udrea. "Towards integrated mid-infrared gas sensors". *Sensors*, 19:2076, 2019.

[11] D. Richter, D. G. Lancaster, R. F. Curl, W. Neu, and F. K. Tittel. "Compact mid-infrared trace gas sensor based on difference-frequency generation of two diode lasers in periodically poled LiNbO$_3$". *Applied Physics B*, 67:347–350, 1998.

[12] Matthew R McCurdy, Yury Bakhirkin, Gerard Wysocki, Rafal Lewicki, and Frank K Tittel. "Recent advances of laser-spectroscopy-based techniques for applications in breath analysis". *Journal of Breath Research*, 1:014001, 2007.

[13] Ramya Selvaraj, Nilesh J. Vasa, S. M. Shiva Nagendra, and Boris Mizaikoff. "Advances in mid-infrared spectroscopy-based sensing techniques for exhaled breath diagnostics". *Molecules*, 25, 2020.

[14] Clément Frayssinous, Vincent Fortin, Jean-Philippe Bérubé, Alex Fraser, and Réal Vallée. "Resonant polymer ablation using a compact 3.44 µm fiber laser". *Journal of Materials Processing Technology*, 252:813–820, 2018.

[15] Ilya Mingareev, Fabian Weirauch, Alexander Olowinsky, Lawrence Shah, Pankaj Kadwani, and Martin Richardson. "Welding of polymers using a 2 µm thulium fiber laser". *Optics Laser Technology*, 44:2095–2099, 2012.

[16] Valentin Petrov. "Frequency down-conversion of solid-state laser sources to the mid-infrared spectral range using non-oxide nonlinear crystals". *Progress in Quantum Electronics*, 42:1–106, 2015.

[17] D Brida, C Manzoni, G Cirmi, M Marangoni, S Bonora, P Villoresi, S De Silvestri, and G Cerullo. "Few-optical-cycle pulses tunable from the visible to the mid-infrared by optical parametric amplifiers". *Journal of Optics*, 12:013001, 2009.

[18] David G. Lancaster. "Efficient Nd:YAG pumped mid-IR laser based on cascaded KTP and ZGP optical parametric oscillators and a ZGP parametric amplifier". *Optics Communications*, 282:272–275, 2009.

[19] Poh Boon Phua, Kin Seng Lai, Rui Fen Wu, and Tow Chong Chong. "High-efficiency mid-infrared ZnGeP$_2$ optical parametric oscillator in a multimode-pumped tandem optical parametric oscillator". *Appl. Opt.*, 38:563–565, 1999.

[20] Antoine Godard. "Infrared (2–12 µm) solid-state laser sources: a review". *Comptes Rendus Physique*, 8:1100–1128, 2007. Optical parametric sources for the infrared.

[21] Sergey Vasilyev, Igor Moskalev, Viktor Smolski, Jeremy Peppers, Mike Mirov, Yury Barnakov, Vladimir Fedorov, Dmitry Martyshkin, Sergey Mirov, and Valentin Gapontsev. "Kerr-lens mode-locked Cr:ZnS oscillator reaches the spectral span of an optical octave". *Opt. Express*, 29:2458–2465, 2021.

[22] Sergei Tomilov, Martin Hoffmann, Yicheng Wang, and Clara J Saraceno. "Moving towards high-power thin-disk lasers in the 2 µm wavelength range". *Journal of Physics: Photonics*, 3:022002, 2021.

[23] Maria Pawliszewska, Tadeusz Martynkien, Aleksandra Przewłoka, and Jarosław Sotor. "Dispersion-managed Ho-doped fiber laser mode-locked with a graphene saturable absorber". *Opt. Lett.*, 43:38–41, 2018.

[24] Yicheng Wang, Weidong Chen, Mark Mero, Lizhen Zhang, Haifeng Lin, Zhoubin Lin, Ge Zhang, Fabian Rotermund, Young Jun Cho, Pavel Loiko, Xavier Mateos, Uwe Griebner, and Valentin Petrov. "Sub-100 fs Tm:MgWO$_4$ laser at 2017 nm mode locked by a graphene saturable absorber". *Opt. Lett.*, 42:3076–3079, 2017.

[25] Zhongben Pan, Yicheng Wang, Yongguang Zhao, Hualei Yuan, Xiaojun Dai, Huaqiang Cai, Ji Eun Bae, Sun Young Choi, Fabian Rotermund, Xavier Mateos, Josep Maria Serres, Pavel Loiko, Uwe Griebner, and Valentin Petrov. "Generation of 84-fs pulses from a mode-locked Tm:CNNGG disordered garnet crystal laser". *Photon. Res.*, 6:800–804, 2018.

[26] Yicheng Wang, Yongguang Zhao, Zhongben Pan, Ji Eun Bae, Sun Young Choi, Fabian Rotermund, Pavel Loiko, Josep Maria Serres, Xavier Mateos, Haohai Yu, Huaijin Zhang, Mark Mero, Uwe Griebner, and Valentin Petrov. "78 fs SWCNT-SA mode-locked Tm:CLNGG disordered garnet crystal laser at 2017 nm". *Opt. Lett.*, 43:4268–4271, 2018.

[27] Li Wang, Weidong Chen, Zhongben Pan, Pavel Loiko, Ji Eun Bae, Fabian Rotermund, Xavier Mateos, Uwe Griebner, and Valentin Petrov. "Sub-100 fs mode-locked Tm:CLTGG laser". *Opt. Express*, 29:31137–31144, 2021.

[28] Yicheng Wang, Wei Jing, Pavel Loiko, Yongguang Zhao, Hui Huang, Xavier Mateos, Soile Suomalainen, Antti Härkönen, Mircea Guina, Uwe Griebner, and Valentin Petrov. "Sub-10 optical-cycle passively mode-locked Tm:(Lu$_{2/3}$Sc$_{1/3}$)$_2$O$_3$ ceramic laser at 2 µm". *Opt. Express*, 26:10299–10304, 2018.

[29] Yongguang Zhao, Li Wang, Weidong Chen, Zhongben Pan, Yicheng Wang, Peng Liu, Xiaodong Xu, Ying Liu, Deyuan Shen, Jian Zhang, Mircea Guina, Xavier Mateos, Pavel Loiko, Zhengping Wang, Xingguang Xu, Jun Xu, Mark Mero, Uwe Griebner, and Valentin Petrov. "SESAM mode-locked Tm:LuYO$_3$ ceramic laser generating 54-fs pulses at 2048nm". *Appl. Opt.*, 59:10493–10497, 2020.

[30] Yongguang Zhao, Li Wang, Yicheng Wang, Jian Zhang, Peng Liu, Xiaodong Xu, Ying Liu, Deyuan Shen, Ji Eun Bae, Tae Gwan Park, Fabian Rotermund, Xavier Mateos, Pavel Loiko, Zhengping Wang, Xingguang Xu, Jun Xu, Mark Mero, Uwe Griebner, Valentin Petrov, and Weidong Chen. "SWCNT-SA mode-locked Tm:LuYO$_3$ ceramic laser delivering 8-optical-cycle pulses at 2.05µm". *Opt. Lett.*, 45:459–462, 2020.

[31] Yongguang Zhao, Li Wang, Weidong Chen, Pavel Loiko, Yicheng Wang, Zhongben Pan, Hanlin Yang, Wei Jing, Hui Huang, Jiachen Liu, Xavier Mateos, Zhengping Wang, Xinguang Xu, Uwe Griebner, and Valentin Petrov. "Kerr-lens mode-locked Tm-doped sesquioxide ceramic laser". *Opt. Lett.*, 46:3428–3431, 2021.

[32] J. Garcia, L. E. Bausá, and D. Jaque. *"Optical spectroscopy of inorganic solids"*. Johm Wiley ad Sons, Ltd, 2005.

[33] Hiroki Tanaka, Sascha Kalusniak, Moritz Badtke, Maxim Demesh, Nikolai V. Kuleshov, Fumihiko Kannari, and Christian Kränkel. "Visible solid-state lasers based on Pr^{3+} and Tb^{3+}". *Progress in Quantum Electronics*, 84:100411, 2022.

[34] Christian Kränkel, Daniel-Timo Marzahl, Francesca Moglia, Günter Huber, and Philip Werner Metz. "Out of the blue: semiconductor laser pumped visible rare-earth doped lasers". *Laser Photonics Review*, 10, 2016.

[35] R. I. Woodward, M. R. Majewski, G. Bharathan, D. D. Hudson, A. Fuerbach, and S. D. Jackson. "Watt-level dysprosium fiber laser at 3.15 µm with 73% slope efficiency". *Opt. Lett.*, 43:1471–1474, Apr 2018.

[36] Alphan Sennaroglu and Yagiz Morova. "Divalent (Cr^{2+}), trivalent (Cr^{3+}), and tetravalent (Cr^{4+}) chromium ion-doped tunable solid-state lasers operating in the near and mid-infrared spectral regions". *Appl. Phys. B*, 128, 2022.

[37] 桜井 弘. "元素118の新知識". 株式会社　講談社, 2017.

[38] Richard P. Leavitt, Jhon B. Gruber, N. C. Chang, and Clyde A. Morrison. "Optical spectra, energy levels, and crystal-ield analysis of tripositive rare-earth ions in y_2o_3. ii. non-kramers ions in c_2 sites". *J. Chem. Phys.*, 76:4775, 1982.

[39] R. Moncorgé, Y. Guyot, C. Kränkel, K. Lebbou, and A. Yoshikawa. "Mid-infrared emission properties of the Tm^{3+}-doped sesquioxide crystals Y_2O_3, Lu_2O_3, Sc_2O_3 and mixed compounds $(Y,Lu,Sc)_2O_3$ around 1.5-, 2- and 2.3-µm". *J. Lumin.*, 241:118537, 2022.

[40] Wei Zheng, Haomiao Zhu, Renfu Li, Datao Tu, Yongsheng Liu, Wenqin Luo, and Xueyuan Chen. "Visible-to-infrared quantum cutting by phonon-assisted energy transfer in YPO_4:Tm^{3+} Yb^{3+} phosphors". *Phys. Chem. Chem. Phys.*, 14:6974–6980, 2012.

[41] Till Walbaum, Matthias Heinzig, Thomas Schreiber, Ramona Eberhardt, and Andreas Tünnermann. "Monolithic thulium fiber laser with 567 W output power at 1970 nm". *Opt. Lett.*, 41:2632–2635, 2016.

[42] Eisuke Fujita, Yutaka Mashiko, Seira Asaya, Mitsuru Musha, and Masaki Tokurakawa. "High power narrow-linewidth linearly-polarized 1610 nm Er:Yb all-fiber MOPA". *Opt. Express*, 24:26255–26260, 2016.

[43] Yang Zhang, Jiaxin Song, Jun Ye, Jiangming Xu, Tianfu Yao, and Pu Zhou. "Tunable random Raman fiber laser at 1.7 µm region with high spectral purity". *Opt. Express*, 27:28800–28807, 2019.

[44] Ning Zhang, Zhanxin Wang, Shande Liu, Wei Jing, Hui Huang, Zixuan Huang, Kangzhen Tian, Zhiyong Yang, Yongguang Zhao, Uwe Griebner, Valentin Petrov, and Weidong Chen. "Watt-level femtosecond Tm-doped "mixed" sesquioxide ceramic laser in-band pumped by a Raman fiber laser at 1627 nm". *Opt. Express*, 30:23978–23985, 2022.

[45] Kenichi Ueda. "波長可変固体レーザーの物理". *Japanese Journal of Optics*, 25:498–504, 1996.

[46] Livio Fornasiero. *"Nd^{3+}- und Tm^{3+}-dotierte Sesquioxide"*. Phd thesis, University of Hamburg, 1999.

[47] Cesar Jauregui, Jens Limpert, and Andreas Tünnermann. "High-power fibre lasers". *Nature photonics*, 7:861–867, 2013.

[48] Y. F. Chen. "High-power diode-pumped actively Q-switched Nd:YVO$_4$ self-Raman laser:influence of dopant concentration". *Opt. Lett.*, 29:1915–1917, 2004.

[49] A.A. Kaminskii, M. Bettinelli, J. Dong, D. Jaque, and K. Ueda. "Nanosecond Nd^{3+}:LuVO$_4$ self-Raman laser". *Laser Physics Letters*, 6:374–379, 2009.

[50] Sergey Vasilyev, Igor Moskalev, Mike Mirov, Viktor Smolski, Sergey Mirov, and Valentin Gapontsev. "Ultrafast middle-IR lasers and amplifiers based on polycrystalline Cr:ZnS and Cr:ZnSe". *Opt. Mater. Express*, 7:2636–2650, 2017.

[51] C. Kränkel. "Rare-earth-doped sesquioxides for diode-pumped high-power lasers in the 1-, 2-, and 3-µm spectral range". *IEEE J. Sel. Top. Quant. Electron.*, 21:250–262, 2015.

[52] David E. Zelmon, Jessica M. Northridge, Nicholas D. Haynes, Dan Perlov, and Klaus Petermann. "Temperature-dependent Sellmeier equations for rare-earth sesquioxides". *Appl. Opt.*, 52:3824–3828, 2013.

[53] Adelbert Owyoung, R. W. Hellwarth, and Nicholas George. "Intensity-induced changes in optical polarizations in glasses". *Phys. Rev. B*, 5:628–633, 1972.

[54] W. L. Smith, J. H. Bechtel, and N. Bloembergen. "Dielectric-breakdown threshold and nonlinear-refractive-index measurements with picosecond laser pulses". *Phys. Rev. B*, 12:706–714, 1975.

[55] Robert Adair, L. L. Chase, and Stephen A. Payne. "Nonlinear refractive index of optical crystals". *Phys. Rev. B*, 39:3337–3350, Feb 1989.

[56] M. Sheik-bahae, A. A. Said, and E. W. Van Stryland. "High-sensitivity, single-beam n$_2$ measurements". *Opt. Lett.*, 14:955–957, 1989.

[57] Yu Senatsky, A Shirakawa, Y Sato, J Hagiwara, J Lu, K Ueda, H Yagi, and T Yanagitani. "Nonlinear refractive index of ceramic laser media and perspectives of their usage in a high-power laser-driver". *Laser Physics Letters*, 1:500–506, 2004.

[58] Alexander A. Lagatsky, Oleg L. Antipov, and Wilson Sibbett. "Broadly tunable femtosecond Tm:Lu$_2$O$_3$ ceramic laser operating around 2070 nm". *Opt. Express*, 20:19349–19354, 2012.

[59] Charles Kittel. *"Introduction to solid state physics, 8th Edition"*. WILEY, 2004.

[60] Tso Yee Fan, Daniel J. Ripin, Roshan L. Aggarwal, Juan R. Ochoa, Bien Chann, Michael Tilleman, and Joshua Spitzberg. "Cryogenic Yb^{3+}-doped solid-state lasers". *IEEE J. Sel. Top. Quant. Electron.*, 13:448–459, 2007.

[61] Philipp Koopmann. *"Thulium- and Holmium-Doped Sesquioxides for 2 µm Lasers"*. Phd thesis, University of Hamburg, 2012.

[62] Christian Kränkel, Anastasia Uvarova, Émile Haurat, Lena Hülshoff, Mario Brützam, Christo Guguschev, Sascha Kalusniak, and Detlef Klimm. "Czochralski growth of mixed cubic sesquioxide crystals in the ternary system Lu_2O_3–Sc_2O_3–Y_2O_3". *Act. Cryst. B*, 77:550–558, 2021.

[63] R. Peters, C. Kränkel, S.T. Fredrich-Thornton, K. Beil, K. Petermann, G. Huber, O.H. Heckl, C.R.E. Baer, C.J. Saraceno, T. Südmeyer, and U. Keller. "Thermal analysis and efficient high power continuous-wave and mode-locked thin disk laser operation of Yb-doped sesquioxides". *Appl. Phys. B*, 102:509–514, 2011.

[64] W.Zhu, G. Zheng, S. Cao, and H. He. "Thermal conductivity of amorphous SiO_2 thin film: A molecular dynamics study". *Sci. Rep.*, 8:10537, 2018.

[65] I. V. Mochalov. "Laser and nonlinear properties of the potassium gadolinium tungstate laser crystal $KGd(WO_4)_2$:Nd^{3+}-(KGW:Nd)". *Opt. Eng.*, 36:6, 1997.

[66] W. Koechner. *"Solid State Laser"*. Engineering6th ed. (Springer Science+Business Media Inc., 2006.

[67] 宮澤　信太郎. *"メルト成長のダイナミクス"*. 共立出版株式会社, 2002.

[68] C. Bárta, F. Petrů, and B. Hájek. "Über die darstellung des einkristalls von scandiumoxyd". *Die Naturwiss.*, 45:36, 1958.

[69] A. Uvarova, C. Guguschev, and C. Kränkel. "Growth and characterization of high-melting sesquioxides for 3 µm lasers". In *2019 Conference on Lasers and Electro-Optics Europe and European Quantum Electronics Conference*, pages ca–10–2. Optica Publishing Group, 2019.

[70] G. Chen, S. Li, L. Zhang, X. Tan, W. Deng, M. He, M. Xu, Y. Yang, S. Zhang, and Y. Hang. "Growth and spectra of Tm^{3+} doped $LuYO_3$ single crystal for 2 µm lasers". *Infrared Phys. Technol.*, 109:103431, 2020.

[71] D.B.Gasson and B.Cockayne. "Oxide crystal growth using gas lasers". *J. Mater. Sci.*, 5:100–104, 1970.

[72] Jake J. Prentice, James A. Grant-Jacob, David P. Shepherd, Robert W. Eason, and Jacob I. Mackenzie. "Yb-doped mixed-sesquioxide films grown by pulsed laser deposition". *J. Cryst.*, 491:51–56, 2018.

[73] V. Peters, A. Bolz, K. Petermann, and G. Huber. "Growth of high-melting sesquioxides by the heat exchanger method". *J. Cryst.*, 237-239:879–883, 2002.

[74] Rigo Peters, Christian Kränkel, Klaus Petermann, and Günter Huber. "Crystal growth by the heat exchanger method, spectroscopic characterization and laser operation of high-purity Yb:Lu$_2$O$_3$". *Journal of Crystal Growth*, 310:1934–1938, 2008.

[75] P. Koopmann, R. Peters, K. Petermann, and G. Huber. "Crystal growth, spectroscopy, and highly efficient laser operation of thulium-doped Lu$_2$O$_3$ around 2 μm". *Appl. Phys. B*, 102:19–24, 2011.

[76] Fabian Reichert, Matthias Fechner, Philipp Koopmann, Christian Brandt, Klaus Petermann, and Guenter Huber. "Spectroscopy and laser action of the nd-doped mixed sesquioxide Lu$_{2-x}$Sc$_x$O$_3$". In *Advances in Optical Materials*, page AMB19. Optica Publishing Group, 2011.

[77] Reinhard Uecker. "The historical development of the Czochralski method". *J. Cryst. Growth*, 401:7–24, 2014.

[78] L Fornasiero, E Mix, V Peters, K Petermann, and G Huber. "Czochralski growth and laser parameters of RE^{3+}-doped Y$_2$O$_3$ and Sc$_2$O$_3$". *Ceram. Int.*, 26:589–592, 2000.

[79] E.Mix. *"Spektroskopie und Lasereigenschaften Yb-dotierter Sesquioxide"*. Phd thesis, University of Hamburg, 1999.

[80] Y.P. Varshni. "Temperature dependence of the energy gap in semiconductors". *Physica*, 34:149–154, 1967.

[81] Colin D. McMillen and Joseph W. Kolis. "Hydrothermal single crystal growth of Sc$_2$O$_3$ and lanthanide-doped Sc$_2$O$_3$". *J. Cryst.*, 310:1939–1942, 2008. the Proceedings of the 15th International Conference on Crystal Growth (ICCG-15) in conjunction with the International Conference on Vapor Growth and Epitaxy and the US Biennial Workshop on Organometallic Vapor Phase Epitaxy.

[82] Matias Velázquez, Philippe Veber, Gabriel Buşe, Yannick Petit, Philippe Goldner, Véronique Jubera, Daniel Rytz, Anaël Jaffres, Mark Peltz, Volker Wesemann, Patrick Aschehough, and Gérard Aka. "Spectroscopic properties of newly flux grown and highly Yb^{3+}-doped cubic RE$_2$O$_3$ (RE=Y, Gd, Lu) laser crystals". *Opt. Mater.*, 39:258–264, 2015.

[83] Jianren Lu, Kazunori Takaichi, Tomohiro Uematsu, Akira Shirakawa, Mitsuru Musha, Ken ichi Ueda, Hideki Yagi, Takagimi Yanagitani, and Alexander A. Kaminskii. "Yb^{3+}:Y$_2$O$_3$ ceramics – a novel solid-state laser material". *Jpn. J. Appl. Phys.*, 41:L1373–L1375, 2002.

[84] Hideki Yagi. *"Development of Polycrystalline laser ceramics"*. Phd thesis, University of Electro-communications, 2006.

[85] Hideki Yagi, Takagimi Yanagitani, Kazunori Takaichi, Ken ichi Ueda, and Alexander A. Kaminskii. "Characterizations and laser performances of highly transparent Nd^{3+}:Y$_3$Al$_5$O$_{12}$ laser ceramics". *Opt. Mater.*, 29:1258–1262, 2007. Proceedings of the 1st International Laser Ceramic Symposium.

[86] K.Takaichi, H.Yagi, K.Ueda, S.Hosokawa, and A.A.Kaminskii. "Lu$_2$O$_3$:Yb^{3+} ceramics – a novel gain material for high-power solid-state lasers". *Phys. Stat. Sol.*, 202:R1–R3, 2005.

[87] Jianren Lu, Junhua Lu, Tomoyo Murai, Kazunori Takaichi, Tomohiro Uematsu, Ken ichi Ueda, Hideki Yagi, Takagimi Yanagitani, and Alexander A. Kaminskii. "Nd^{3+}:Y$_2$O$_3$ ceramic laser". *Jpn. J. Appl. Phys.*, 40:L1277–L1279, 2001.

[88] M. Chaika, S. Balabanov, and D. Permin. "Optical spectra and gain properties of Er^{3+}:Lu$_2$O$_3$ ceramics for eye-safe 1.5-μm lasers". *Opt. Mater.*, 112:110785, 2021.

[89] Z.M. Seeley, J.D. Kuntz, N.J. Cherepy, and S.A. Payne. "Transparent Lu$_2$O$_3$:Eu ceramics by sinter and HIP optimization". *Optical Materials*, 33:1721–1726, 2011.

[90] Wei Jing, Pavel Loiko, Josep Maria Serres, Yicheng Wang, Elena Vilejshikova, Magdalena Aguiló, Francesc Díaz, Uwe Griebner, Hui Huang, Valentin Petrov, and Xavier Mateos. "Synthesis, spectroscopy, and efficient laser operation of "mixed" sesquioxide Tm:(Lu,Sc)$_2$O$_3$ transparent ceramics". *Opt. Mater. Express*, 7:4192–4202, 2017.

[91] R. Boulesteix, R. Epherre, S. Noyau, M. Vandenhende, A. Maître, C. Sallé, G. Alombert-Goget, Y. Guyot, and A. Brenier. "Highly transparent Nd:Lu$_2$O$_3$ ceramics obtained by coupling slip-casting and spark plasma sintering". *Scr. Mater.*, 75:54–57, 2014.

[92] Liqiong An, Akihiko Ito, Jian Zhang, Dingyuan Tang, and Takashi Goto. "Highly transparent Nd^{3+}:Lu$_2$O$_3$ produced by spark plasma sintering and its laser oscillation". *Opt. Mater. Express*, 4:1420–1426, 2014.

[93] Dongyue Yan, Xiaodong Xu, Hao Lu, Yuwei Wang, Peng Liu, and Jian Zhang. "Fabrication and properties of Y$_2$O$_3$ transparent ceramic by sintering aid combinations". *Ceram. Int.*, 42:16640–16643, 2016.

[94] Stanislav Balabanov, Dmitry Permin, Timofey Evstropov, Pavel Andreev, Liza Basyrova, Patrice Camy, Mikhail Baranov, Xavier Mateos, and Pavel Loiko. "Hot pressing of Yb:Y$_2$O$_3$ laser ceramics with LiF sintering aid". *Opt. Mater.*, 119:111349, 2021.

[95] Jun Akiyama, Yoichi Sato, and Takunori Taira. "Laser ceramics with rare-earth-doped anisotropic materials". *Opt. Lett.*, 35:3598–3600, 2010.

[96] Yoichi Sato, Jun Akiyama, and Takunori Taira. "Orientation control of micro-domains in anisotropic laser ceramics". *Opt. Mater. Express*, 3:829–841, 2013.

[97] E. H. Penilla, L. F. Devia-Cruz, M. A. Duarte, Y. Kodera, and J. E. Garay. "Leveraging length scales to create a new class of high-energy, short pulse, tunable laser materials". *Light Sci. Appl.*, 7:33, 2018.

[98] H. Furuse, N. Horiuchi, and B. N. Kim. "Transparent non-cubic laser ceramics with fine microstructure". *Sci. Rep.*, 9:10300, 2019.

[99] Kirill Eremeev, Pavel Loiko, Alain Braud, Patrice Camy, Jian Zhang, Xiaodong Xu, Yongguang Zhao, Peng Liu, Stanislav Balabanov, Elena Dunina, Alexey Kornienko, Liudmila Fomicheva, Xavier Mateos, Uwe Griebner, Valentin Petrov, Li Wang, and Weidong Chen. "Spectroscopy of solid-solution transparent sesquioxide laser ceramic $Tm:LuYO_3$". *Opt. Mater. Express*, 12:3749–3762, 2022.

[100] Z.Liu, G.Toci, A.Pirri, B.Patrizi, Y.Feng, J.Wei, Z.Yang, M.Vannini, and J.Li. "Fabrication, microstructures, and optical properties of $Yb:Lu_2O_3$ laser ceramics from co-precipitated nano-powders". *J. Adv. Ceram.*, 9:674–682, 2020.

[101] A.Shirakawa, K.Takaichi, H.Yagi, M.Tanisho, J.-F.Bisson, J.Lu, K.Ueda, T.Yanagitani, and A.A.Kaminskii. "First mode-locked ceramic laser: Femtosecond $Yb:Y_2O_3$ ceramic laser". *Laser Phys.*, 14:1375–1381, 2004.

[102] Wei Zhou, Haitao Huang, Xiang Chen, Jingru Wang, Rui Xu, Haotian Wang, Yongguang Zhao, Dingyuan Tang, Yishan Wang, and Deyuan Shen. "2 µm vector mode-locked pulses from $Tm:Y_2O_3$ ceramics laser". *Laser Phys.*, 29:04–301, 2019.

[103] O.L.Antipov, A.A.Nivikov, N.G.Zakharov, A.P.Zinoviev, H.Yagi, N.V.Sakharov, M.V. Kruglova, M.O.Marychev, and A.A.Lagatskii. "Efficient 2.1-µm lasers based on $Tm^{3+}:Lu_2O_3$ ceramics pumped by 800–nm laser diodes". *Phys. Status Solidi C*, 10:969–973, 2013.

[104] T.Ishikawa, A.A.Eilanlou, Y.Nabekawa, Y.Fujihira, T.Imahoko, T.Sumiyoshi, F.Kannari, M.Kuwata-Gonokami, and K.Midorikawa. "Kerr lens mode-locked $Yb:Lu_2O_3$ bulk ceramic oscillator pumped by a multimode laser diode". *Jpn. J. Appl. Phys.*, 54:072703, 2015.

[105] M.Tokurakawa, K.Takaichi, A.Shirakawa, and K.Ueda. "Diode-pumped 188 fs mode-locked $Yb^{3+}:Y_2O_3$ ceramic laser". *Appl. Phys. Lett.*, 90:071101, 2007.

[106] Takunori Taira, William M. Tulloch, and Robert L. Byer. "Modeling of quasi-three-level lasers and operation of cw Yb:YAG lasers". *Appl. Opt.*, 36:1867–1874, 1997.

[107] G. Rustad and K. Stenersen. "Modeling of laser-pumped Tm and Ho lasers accounting for upconversion and ground-state depletion". *IEEE J. Quant. Electron.*, 32:1645–1656, 1996.

[108] J.A. Caird, S.A. Payne, P.R. Staber, A.J. Ramponi, L.L. Chase, and W.F. Krupke. "Quantum electronic properties of the $N_3Ga_2Li_3F_{12}/:Cr^{3+}$ laser". *IEEE Journal of Quantum Electronics*, 24:1077–1099, 1988.

[109] M. Schellhorn, S. Ngcobo, and C. Boling. "High-power diode-pumped Tm:YLF slab laser". *Appl. Phys. B*, 94:195–198, 2009.

[110] Pavel Loiko, Jakub Bogusławski, Josep Maria Serres, Esrom Kifle, Maciej Kowalczyk, Xavier Mateos, Jarosław Sotor, Rafał Zybała, Krzysztof Mars, Andrzej Mikuła, Kamil Kaszyca, Magdalena Aguiló, Francesc Díaz, Uwe Griebner, and Valentin Petrov. "Sb_2Te_3 thin film for the passive Q-switching of a $Tm:GdVO_4$ laser". *Opt. Mater. Express*, 8:1723–1732, 2018.

[111] S. V. Kurilchik, J. J. Prentice, R. W. Eason, and J. I. Mackenzie. "Characterisation and laser performance of a Yb:LuAG double-clad planar waveguide grown by pulsed laser deposition". *Appl. Phys. B*, 125:201, 2019.

[112] Weichao Yao, Hiyori Uehara, Shigeki Tokita, Hengjun Chen, Daisuke Konishi, Masanao Murakami, and Ryo Yasuhara. "LD-pumped 2.8 µm Er:Lu$_2$O$_3$ ceramic laser with 6.7 W output power and >30% slope efficiency". *Appl. Phys. Express*, 14:012001, 2020.

[113] Weichao Yao, Hiyori Uehara, Hiroki Kawase, Hengjun Chen, and Ryo Yasuhara. "Highly efficient Er:YAP laser with 6.9 W of output power at 2920 nm". *Opt. Express*, 28:19000–19007, 2020.

[114] Pavel Loiko, Josep Maria Serres, Xavier Mateos, Xiaodong Xu, Jun Xu, Venkatesan Jambunathan, Petr Navratil, Antonio Lucianetti, Tomas Mocek, Xuzhao Zhang, Uwe Griebner, Valentin Petrov, Magdalena Aguiló, Francesc Díaz, and Arkady Major. "Microchip Yb:CaLnAlO$_4$ lasers with up to 91% slope efficiency". *Opt. Lett.*, 42:2431–2434, 2017.

[115] Huang-Jun Zeng, Zhang-Lang Lin, Wen-Ze Xue, Ge Zhang, Zhongben Pan, Haifeng Lin, Pavel Loiko, Xavier Mateos, Valentin Petrov, Li Wang, and Weidong Chen. "SESAM mode-locked Yb:Ca$_3$Gd$_2$(BO$_3$)$_4$ femtosecond laser". *Applied Sciences*, 11, 2021.

[116] Amnon Yariv and Pochi Yeh. "*Photonics optical electronics in modern communications 6th Edition*". Oxford University Press, 2006.

[117] Jie Ma, Zhipeng Qin, Guoqiang Xie, Liejia Qian, and Dingyuan Tang. "Review of mid-infrared mode-locked laser sources in the 2.0 µm–3.5 µm spectral region". *Appl. Phys. Rev.*, 6:0.21317, 2019.

[118] P.V. Mamyshev. "All-optical data regeneration based on self-phase modulation effect". In *24th European Conference on Optical Communication. ECOC '98 (IEEE Cat. No.98TH8398)*, volume 1, pages 475–476, 1998.

[119] Kestutis Regelskis, Julijanas Želudevičius, Karolis Viskontas, and Gediminas Račiukaitis. "Ytterbium-doped fiber ultrashort pulse generator based on self-phase modulation and alternating spectral filtering". *Opt. Lett.*, 40:5255–5258, 2015.

[120] Masaki Tokurakawa, Eisuke Fujita, and Christian Kränkel. "Kerr-lens mode-locked Tm^{3+}:Sc$_2$O$_3$ single-crystal laser in-band pumped by an Er:Yb fiber MOPA at 1611 nm". *Opt. Lett.*, 42:3185–3188, 2017.

[121] Ferda Canbaz, Ismail Yorulmaz, and Alphan Sennaroglu. "Kerr-lens mode-locked 2.3-µm Tm^{3+}:YLF laser as a source of femtosecond pulses in the mid-infrared". *Opt. Lett.*, 42:3964–3967, 2017.

[122] R. Ell, U. Morgner, F. X. Kärtner, J. G. Fujimoto, E. P. Ippen, V. Scheuer, G. Angelow, T. Tschudi, M. J. Lederer, A. Boiko, and B. Luther-Davies. "Generation of 5-fs pulses and octave-spanning spectra directly from a Ti:sapphire laser". *Opt. Lett.*, 26:373–375, 2001.

[123] Yiran Wang, Xiancui Su, Yiyan Xie, Feilong Gao, Santosh Kumar, Qinglin Wang, Cailong Liu, Bingyuan Zhang, Baitao Zhang, and Jingliang He. "17.8 fs broadband Kerr-lens mode-locked Yb:CALGO oscillator". *Opt. Lett.*, 46:1892–1895, 2021.

[124] Meiping Zhu, Kui Yi, Dawei Li, Hongji Qi, Yuanan Zhao, Jie Liu, Xiaofeng Liu, Guohang Hu, and Jianda Shao. "Study on the laser-induced damage performance of HfO_2, Sc_2O_3, Y_2O_3, Al_2O_3 and SiO_2 monolayer coatings". *Proc. SPIE 8885, Laser-Induced Damage in Optical Materials*, 8885:888508, 2013.

[125] H. Haus. "Parameter ranges for CW passive mode locking". *IEEE J. Quant. Electron.*, 12:169–176, 1976.

[126] F. X. Kaertner, L. R. Brovelli, D. Kopf, M. Kamp, I. G. Calasso, , and U. Keller. "Control of solid state laser dynamics by semiconductor devices". *Opt. Eng.*, 34:2024, 1995.

[127] C. Hönninger, R. Paschotta, F. Morier-Genoud, M. Moser, and U. Keller. "Q-switching stability limits of continuous-wave passive mode locking". *J. Opt. Soc. Am. B*, 16:46–56, 1999.

[128] S. Kimura, S. Tani, and Y. Kobayashi. "Q-switching stability limits of Kerr-lens mode locking". *Phys. Rev. A*, 102:043505, 2020.

[129] V.L. Kalashnikov, E. Sorokin, and I.T. Sorokina. "Multipulse operation and limits of the Kerr-lens mode-locking stability". *IEEE J. Quant. Electron.*, 39:323–336, 2003.

[130] M. Becker, D. Kuizenga, and A. Siegman. "Harmonic mode locking of the Nd:YAG laser". *IEEE J. Quant. Electron.*, 8:687–693, 1972.

[131] Masaki Tokurakawa and Akira Shirakawa. "Numerical analysis of fast saturable absorber mode-locked Yb^{3+} lasers under large modulation depth". *Opt. Express*, 23:26288–26298, 2015.

[132] Nathalie Nagl, Sebastian Gröbmeyer, Vladimir Pervak, Ferenc Krausz, Oleg Pronin, and Ka Fai Mak. "Directly diode-pumped, Kerr-lens mode-locked, few-cycle Cr:ZnSe oscillator". *Opt. Express*, 27:24445–24454, 2019.

[133] Anna Suzuki, Christin Kränkel, and Masaki Tokurakawa. "Ultrashort pulse generation from Kerr-lens mode-locked Tm-doped sesquioxide lasers at 2.1 μm". In *Laser Congress 2021 (ASSL,LAC)*, page ATu3A.4. Optica Publishing Group, 2021.

[134] Shota Kimura, Shuntaro Tani, and Yohei Kobayashi. "Raman-assisted broadband mode-locked laser". *Scientific reports*, 9:3738, 2019.

[135] Anna Suzuki, Christian Kränkel, and Masaki Tokurakawa. "High quality-factor kerr-lens mode-locked $Tm:Sc_2O_3$ single crystal laser with anomalous spectral broadening". *Appl. Phys. Express*, 13:052007, 2020.

[136] Takumi Yatsuda and Masaki Tokurakawa. "Few ns Q-dwitched tm fiber laser". In *ALPS2021*, pages ALPS–Poster–10, 2021.

[137] H. Kogelnik, E. Ippen, A. Dienes, and C. Shank. "Astigmatically compensated cavities for CW dye lasers". *IEEE J. Quant. Electron.*, 8:373–379, 1972.

[138] Shai Yefet and Avi Pe039;er. "A review of cavity design for Kerr lens mode-locked solid-state lasers". *Appl. Sci.*, 3:694–724, 2013.

[139] Masaki Tokurakawa. *"Kerr-lens mode locked lasers based on Yb^{3+}-doped materials"*. Phd thesis, University of Electro-Communications, 2010.

[140] A. A. Kaminskii. "Laser with combined active medium". *Sov. Phys.*, 13:413–416, 1968.

[141] Masaki Tokurakawa, Akira Shirakawa, Ken ichi Ueda, Hideki Yagi, Meichin Noriyuki, Takagimi Yanagitani, and Alexander A. Kaminskii. "Diode-pumped ultrashort-pulse generation based on Yb^{3+}:Sc_2O_3 and Yb^{3+}:Y_2O_3 ceramic multi-gain-media oscillator". *Opt. Express*, 17:3353–3361, 2009.

[142] Masaki Yumoto, Norihito Saito, and Satoshi Wada. "Extension of mid-IR lasing spectral region using Cr:ZnSe and Cr:CdSe combined active medium. In *2019 Conference on Lasers and Electro-Optics Europe and European Quantum Electronics Conference*, pages ca–p–14. Optica Publishing Group, 2019.

[143] P. Loiko, X. Mateos, S. Y. Choi, F. Rotermund, J. M. Serres, M. Aguiló, F. Díaz, K. Yumashev, U. Griebner, and V. Petrov. "Vibronic thulium laser at 2131 nm Q-switched by single-walled carbon nanotubes". *J. Opt. Soc. Am. B*, 33:D19–D27, 2016.

[144] F. Liang, C. He, D. Lu, Q. Fang, Y. Fu, H. Yu, H. Zhang, and Y. Chen. "Multiphonon-assisted lasing beyond the fluorescence spectrum". *Nat. Phys.*, 8:1312–1316, 2022.

[145] M.L. Dennis and I.N. Duling. "Experimental study of sideband generation in femtosecond fiber lasers". *IEEE J. Quant. Electron.*, 30:1469–1477, 1994.

[146] P. F. Curley, Ch. Spielmann, T. Brabec, F. Krausz, E. Wintner, and A. J. Schmidt. "Operation of a femtosecond Ti:sapphire solitary laser in the vicinity of zero group-delay dispersion". *Opt. Lett.*, 18:54–56, 1993.

[147] Cinia Schriber, Florian Emaury, Andreas Diebold, Sandro Link, Matthias Golling, Kolja Beil, Christian Kränkel, Clara J. Saraceno, Thomas Südmeyer, and Ursula Keller. "Dual-gain SESAM modelocked thin disk laser based on Yb:Lu_2O_3 and Yb:Sc_2O_3. *Opt. Express*, 22:18979–18986, 2014.

[148] K. S. Bagdasarov, A. A. Kaminskii, A. M. Kevorkov, L. Li, A. M. Prokhorov, T. A. Tevosyan, and S. E. Sarkisov. "Investigation of stimulated radiation of cubic-crystals of $YScO_3$ with Nd^{3+} ions". *Dokl. Akad. Nauk SSSR*, 224:798–801, 1975.

[149] Cyrill R. E. Baer, Christian Kränkel, Oliver H. Heckl, Matthias Golling, Thomas Südmeyer, Rigo Peters, Klaus Petermann, Günter Huber, and Ursula Keller. "227-fs pulses from a mode-locked Yb:$LuScO_3$ thin disk laser". *Opt. Express*, 17:10725–10730, 2009.

[150] Clara J. Saraceno, Oliver H. Heckl, Cyrill R. E. Baer, Matthias Golling, Thomas Südmeyer, Kolja Beil, Christian Kränkel, Klaus Petermann, Günter Huber, and Ursula Keller. "SESAMs for high-power femtosecond modelocking: power scaling of an Yb:LuScO$_3$ thin disk laser to 23 W and 235 fs". *Opt. Express*, 19:20288–20300, 2011.

[151] T. Südmeyer, C. Kränkel, C.R.E. Baer, O.H. Heckl, C.J. Saraceno, M. Golling, R. Peters, K. Petermann, G. Huber, and U. Keller. "High-power ultrafast thin disk laser oscillators and their potential for sub-100-femtosecond pulse generation". *Appl. Phys. B*, 97:281–295, 2009.

[152] Andreas Schmidt, Valentin Petrov, Uwe Griebner, Rigo Peters, Klaus Petermann, Günter Huber, Christian Fiebig, Katrin Paschke, and Götz Erbert. "Diode-pumped mode-locked Yb:LuScO$_3$ single crystal laser with 74 fs pulse duration". *Opt. Lett.*, 35:511–513, 2010.

[153] P. Koopmann, S. Lamrini, K. Scholle, P. Fuhrberg, K. Petermann, and G. Huber. "Laser operation and spectroscopic investigations of Tm:LuScO$_3$". In *CLEO/Europe and EQEC 2011 Conference Digest*, pages CA1–4. Optica Publishing Group, 2011.

[154] H. Wu, G.H. Pan, Z. Hao, L. Zhang, X. Zhang, L. Zhang, H. Zao, and J. Zhang. "Laser-quality, Tm:(Lu$_{0.8}$Sc$_{0.2}$)$_2$O$_3$ mixed sesquioxide ceramics shaped by gelcasting of well-dispersed nanopowders". *J. Am. Ceram. Soc.*, 102:4919–4928, 2019.

[155] D. Li, L. Kong, X. Xu, P. Liu, G. Xie, J. Zhang, and J. Xu. "Spectroscopy and mode-locked laser operation of Tm:LuYO$_3$ mixed sesquioxide ceramic". *Opt. Express*, 17:24416–24425, 2019.

[156] Zhiyong Zhou, Xiaofeng Guan, Xiaoxu Huang, Bin Xu, Huiying Xu, Zhiping Cai, Xiaodong Xu, Peng Liu, Dongzhen Li, Jian Zhang, and Jun Xu. "Tm^{3+}-doped LuYO$_3$ mixed sesquioxide ceramic laser: effective 2.05 μm source operating in continuous-wave and passive Q-switching regimes". *Opt. Lett.*, 42:3781–3784, 2017.

[157] Xiaodong Xu, Zongwen Hu, Dongzhen Li, Peng Liu, Jian Zhang, Bin Xu, and Jun Xu. "First laser oscillation of diode-pumped Tm^{3+}-doped LuScO$_3$ mixed sesquioxide ceramic". *Opt. Express*, 25:15322–15329, 2017.

[158] Christian Kränkel, Anastasia Uvarova, Christo Guguschev, Sascha Kalusniak, Lena Hülshoff, Hiroki Tanaka, and Detlef Klimm. "Rare-earth doped mixed sesquioxides for ultrafast lasers [Invited]". *Opt. Mater. Express*, 12:1074–1091, 2022.

[159] Lena Hülshoff, Anastasia Uvarova, Christo Guguschev, Sascha Kalusniak, Hiroki Tanaka, Detlef Klimm, and Christian Kränkel. "Czochralski growth and laser operation of Er- and Yb-doped mixed sesquioxide crystals". In *Laser Congress 2021 (ASSL,LAC)*, page ATh1A.2. Optica Publishing Group, 2021.

[160] Angela Pirri, Roman N. Maksimov, Vladislav A. Shitov, Vladimir V. Osipov, Elisa Sani, Barbara Patrizi, Matteo Vannini, and Guido Toci. "Continuously tuned (Tm$_{0.05}$Sc$_{0.252}$Y$_{0.698}$)$_2$O$_3$ ceramic laser with emission peak at 2076 nm". *J. Alloys Compd.*, 889:161585, 2021.

[161] Changliang Yang, Jiquan Huang, Qiufeng Huang, Zhonghua Deng, Yun Wang, Xiaoyun Li, Zehua Zhou, Jian Chen, Zhuguang Liu, and Wang Guo. Optical, thermal, and mechanical properties of $(Y_{1x}Sc_x)_2O_3$ transparent ceramics. *J. Adv. Ceram.*, 11:901–911, 2022.

[162] Angela Pirri, Barbara Patrizi, Roman N. Maksimov, Vladislav A. Shitov, Vladimir V. Osipov, Matteo Vannini, and Guido Toci. "Spectroscopic investigation and laser behaviour of Yb-doped laser ceramics based on mixed crystalline structure $(Sc_xY_{1-x})_2O_3$". *Ceram. Int.*, 47:29483–29489, 2021.

[163] Vladislav Shitov, Liza Basyrova, Pavel Loiko, Roman Maksimov, Oleg Samatov, Danil Vasin, Jean-Louis Doualan, Alain Braud, and Patrice Camy. "Mid-infrared emission properties of transparent Er: $YScO_3$ laser ceramic". In *2022 International Conference Laser Optics (ICLO)*, pages 1–1, 2022.

[164] J.B. Clark, P.W. Richter, and L.Du Toit. "High-pressure synthesis of $YScO_3$, $HoScO_3$, $ErScO_3$, and $TmScO_3$, and a reevaluation of the lattice constants of the rare earth scandates". *Journal of Solid State Chemistry*, 23:129–134, 1978.

[165] Yuhei Shimizu and Kazushige Ueda. "Phase formation and UV luminescence of Gd^{3+} doped perovskite-type $YScO_3$". *J. Solid State Chem.*, 242:170–174, 2016.

[166] Ruiqi Guo, Dapeng Huang, Dazhi Lu, Fei Liang, Qingli Zhang, Haohai Yu, and Huaijin Zhang. "Spectral broadening mechanism of Yb^{3+}-doped cubic $Lu_xSc_{2-x}O_3$ sesquioxide crystals for ultrafast lasers". *Opt. Mater. Express*, 12:1963–1976, 2022.

[167] L. Fornasiero, E. Mix, V. Peters, K. Petermann, and G. Huber. "Czochralski growth and laser parameters of RE^{3+}-doped Y_2O_3 and Sc_2O_3. *Ceram. Int.*, 26:589–592, 2000.

[168] Y. Repelin, C. Proust, E. Husson, and J.M. Beny. "Vibrational spectroscopy of the C-form of yttrium sesquioxide". *Journal of Solid State Chemistry*, 118:163–169, 1995.

[169] M. V. Abrashev, N. D. Todorov, and J. Geshev. "Raman spectra of R_2O_3 (R—rare earth) sesquioxides with C-type bixbyite crystal structure: A comparative study". *J. Appl. Phys.*, 116:103508, 2014.

[170] N. D. Todorov, M. V. Abrashev, V. Marinova, M. Kadiyski, L. Dimowa, and E. Faulques. "Raman spectroscopy and lattice dynamical calculations of Sc_2O_3 single crystals". *Phys. Rev. B*, 87:104301, 2013.

[171] F. Yue, V. Jambunathan, S. P. David, X. Mateos, M. Aguiló, F.Díaz, J. Šulc, A. Lucianetti, and T. Mocek. "Spectroscopy and diode-pumped continuous-wave laser operation of Tm:Y_2O_3 transparent ceramic at cryogenic temperatures". *Appl. Phys. B*, 126:44, 2020.

[172] Henning Kühn, Susanne T. Fredrich-Thornton, Christian Kränkel, Rigo Peters, and Klaus Petermann. "Model for the calculation of radiation trapping and description of the pinhole method". *Opt. Lett.*, 32:1908–1910, 2007.

[173] C. Kränkel, D. Fagundes-Peters, S. T. Fredrich, J. Johannsen, M. Mond, M. Bernhagen, and R. Uecker. "Continuous wave laser operation of $Yb^{3+}:YVO_4$". *Appl. Phys. B*, 79:543–546, 2004.

[174] G. Turri, V. Sudesh, M. Richardson, M. Bass, A. Toncelli, and M. Tonelli. "Temperature-dependent spectroscopic properties of Tm^{3+} in germanate, silica, and phosphate glasses: A comparative study". *J. Appl. Phys.*, 103:093104, 2008.

[175] F. Yue, V. Jambunathan, S. P. David, X. Mateos, J. Šulc, M. Smrž, and T. Mocek. "Diode-pumped master oscillator power amplifier system based on cryogenically cooled $Tm:Y_2O_3$ transparent ceramics". *Opt. Mater. Express*, 11:1489–1496, 2021.

[176] A. Pirri, R. N. Maksimov, J. Li, M. Vannini, and G. Toci. "Achievements and future perspectives of the trivalent thulium-ion-doped mixed-sesquioxide ceramics for laser applications". *Materials*, 15:2084, 2022.

[177] J.M. Badie. "Phases et transitions de phases à haute tempèrature dans les sytèmes Sc_2O_3-Ln_2O_3 (Ln = lanthanide et yttrium)". *Rev. Int. Hautes Temp.*, 15:183–199, 1985.

[178] C. P. J. Barty, G. Korn, F. Raksi, C. Rose-Petruck, J. Squier, A.-C. Tien, K. R. Wilson, V. V. Yakovlev, and K. Yamakawa. "Regenerative pulse shaping and amplification of ultrabroadband optical pulses". *Opt. Lett.*, 21:219–221, 1996.

[179] M. Hentschel, Z. Cheng, F. Krausz, and Ch. Spielmann. "Generation of 0.1-TW optical pulses with a single-stage Ti:sapphire amplifier at a 1-kHz repetition rate". *Appl. Phys. B (Suppl 1)*, pages S161–S164, 2004.

[180] Linus Pauling and M. D. Shappell. "8. The crystal structure of bixbyite and the C-modification of the sesquioxides". *Zeitschrift für Kristallographie - Crystalline Materials*, 75:128–142, 1930.

[181] T. Heeg. "*Epitaktische Seltenerd-Scandatschichten für die Mikroelektronik.*". Phd thesis, University of Cologne, 2007.

[182] F. Euler and J. A. Bruce. "Oxygen coordinates of compounds with garnet structure". *Act. Cryst.*, 19:971–978, 1965.

[183] A. A. Kaminskii. "*Laser crystals*". Springer, 1981.

[184] L. Gmelin. "*Handbook of inorganic chemistry*". Springer-Verlag, 1981.

[185] L. Dobrzycki, E. Bulska, D. A. Pawlak, Z. Frukacz, and K. Wozniak. "Structure of YAG crystals doped/substituted with erbium and ytterbium". *Inorg. Chem.*, 43:7656, 2004.

[186] M. J. Weber. "*Handbook of optical materials*". Boca Rotan, 2002.

[187] J. L. Caslavsky and D. J. Viechnicki. "Melting behaviour and metastability of yttrium aluminium garnet (YAG) and $YAlO_3$ determined by optical differential thermal analysis". *J. Mat. Sci.*, 15:1709–1718, 1980.

[188] David E. Zelmon, David L. Small, and Ralph Page. Refractive-index measurements of undoped yttrium aluminum garnet from 0.4 to 5.0 μm. *Appl. Opt.*, 37:4933–4935, 1998.

[189] R. Peters. *"Ytterbium-dotierte Sesquioxide als hocheffiziente Lasermaterialien"*. Phd thesis, University of Hamburg, 2009.

[190] R. L. Aggarwal, D. J. Ripin, J. R. Ochoa, , and T. Y. Fan. "Measurement of thermo-optic properties of $Y_3Al_5O_{12}$, $Lu_3Al_5O_{12}$, $YAiO_3$, $LiYF_4$, $LiLuF_4$, BaY_2F_8, $KGd(WO_4)_2$, and $KY(WO_4)_2$ laser crystals in the 80–300K temperature range". *J. Appl. Phys.*, 98:103514, 2005.

[191] David C. Brown, Sten Tornegård, Joseph Kolis, Colin McMillen, Cheryl Moore, Liurukara Sanjeewa, and Christopher Hancock. "The application of cryogenic laser physics to the development of high average power ultra-short pulse lasers". *Appl. Sci.*, 6, 2016.

[192] Darren Rand, Daniel Miller, Daniel J. Ripin, and Tso Yee Fan. "Cryogenic Yb3+-doped materials for pulsed solid-state laser applications [invited]". *Opt. Mater. Express*, 1:434–450, 2011.

[193] Tso Yee Fan, Daniel J. Ripin, Roshan L. Aggarwal, Juan R. Ochoa, Bien Chann, Michael Tilleman, and Joshua Spitzberg. "Cryogenic Yb^{3+}-doped solid-state lasers". *IEEE J. Sel. Top. Quant. Electron.*, 13:448–459, 2007.

[194] V. Cardinali, E. Marmois, B. Le Garrec, and G. Bourdet. "Determination of the thermo-optic coefficient dn/dT of ytterbium doped ceramics (Sc_2O_3, Y_2O_3, Lu_2O_3, YAG), crystals (YAG, CaF_2) and neodymium doped phosphate glass at cryogenic temperature". *Optical Materials*, 34:990–994, 2012.

[195] T.T. Basiev, Yu.V. Orlovskii, K.K. Pukhov, V.B. Sigachev, M.E. Doroshenko, and I.N. Vorob'ev. "Multiphonon relaxation rates measurements and theoretical calculations in the frame of non-linear and non-Coulomb model of a rare-earth ion-ligand interaction". *J. Lumin.*, 68:241–253, 1996.

[196] J. Koetke and G. Huber. "Infrared excited-state absorption and stimulated-emission cross sections of Er^{3+}-doped crystals". *Appl. Phys. B*, 61:151 – 158, 1995.

List of Publications

Scientific journal articles

1. <u>Anna Suzuki</u>, Christian Kränkel, Masaki Tokurakawa, "High quality-factor Kerr-lens mode-locked $Tm:Sc_2O_3$ single crystal laser with anomalous spectral broadening," Applied Physics Express 13, 052007 (2020)."

2. <u>Anna Suzuki</u>, Christian Kränkel, and Masaki Tokurakawa, "Sub-6 optical-cycle Kerr-lens mode-locked $Tm:Lu_2O_3$ and $Tm:Sc_2O_3$ combined gain media laser at 2.1 μm," Optics Express 29, 19465-19471 (2021).

3. <u>Anna Suzuki</u>, Sascha Kalusniak, Hiroki Tanaka, Mario Brützam, Steffen Ganschow, Masaki Tokurakawa, and Christian Kränkel, "Spectroscopy and 2.1 μm laser operation of Czochralski-grown $Tm^{3+}:YScO_3$ crystals," Optics Express 30, 42762-42771 (2022).

International conference

Oral presentation

1. <u>Anna Suzuki</u>, Christian Kränkel, M. Tokurakawa, "High Quality-Factor Kerr-lens Mode-locked $Tm:Sc_2O_3$ Laser with anomalous spectral broadening," The 8th Advanced Lasers and Photon Sources(ALPS), ALPS15-05, Yokohama Japan, Apr. 2019

2. <u>Anna Suzuki</u>, Masaki Tokurakawa, Christian Kränkel, "High Quality-Factor Kerr-lens Mode-locked $Tm:Sc_2O_3$ Laser Beyond the Gain Bandwidth Limitation," CLEO/Europe-EQEC 2019, CA-6.3, Munich, Germany, Jun. 2019

3. <u>Anna Suzuki</u>, Masaki Tokurakawa, Christian Kränkel, "Kerr-lens mode-locked $Tm^{3}+:RE_2O_3$ (RE=Lu, Sc) lasers" The 9th Advanced Lasers and Photon Sources(ALPS), ALPS3-03, online, Apr. 2020

4. <u>Anna Suzuki</u>, Christian Kränkel, and Masaki Tokurakawa, "Combined Gain Media 60 fs Kerr-Lens Mode-Locked Laser Based on $Tm:Lu_2O_3$ and $Tm:Sc_2O_3$," CLEO 2021, SF2M.6, online, May 2021

5. <u>Anna Suzuki</u>, Christian Kränkel, and Masaki Tokurakawa, "Sub-9 Optical-cycle Kerr-lens Mode-locked Combined Gain Media Laser Based on Tm-doped Sesquioxide," CLEO/Europe-EQEC, CA-5.2, online, Jun. 2021

6. <u>Anna Suzuki</u>, Christian Kränkel, and Masaki Tokurakawa, "Ultrashort Pulse Generation from Kerr-lens Mode-locked Tm-doped Sesquioxide Lasers at 2.1 μm," ASSL, ATu3A.4, online, Oct. 2021

7. <u>Anna Suzuki</u>, Sascha Kalusniak, Hiroki Tanaka, Mario Brützam, Steffen Ganshow, Masaki Tokurakawa, Christian Kränkel, "Growth, spectroscopy, and laser operation of Tm^{3+}:$YScO_3$ mixed sesquioxide crystal," The 11th Advanced Lasers and Photon Sources(ALPS), ALPS3-03, Yokohama, Japan, Apr. 2020

8. <u>Anna Suzuki</u>, Sascha Kalusniak, Hiroki Tanaka, Mario Brützam, Steffen Ganshow, Masaki Tokurakawa, Christian Kränkel, "Spectroscopy and continuous wave laser operation of Tm^{3+}-doped $YScO_3$ mixed sesquioxide crystal," 10TH EPS-QEOD EUROPHOTON CONFERENC, THU-SSL-5.7, Hannover, Germany, Sep. 2022

9. <u>Anna Suzuki</u>, Sascha Kalusniak, Hiroki Tanaka, Mario Bruetzam, Steffen Ganshow, Masaki Tokurakawa, Christian Kränkel, "Laser Operation of Czochralski-grown Tm^{3+}-doped Mixed Sesquioxides at 2.1 μm," ASSL, ATu3A.4, Barcelona, Spain, Dec. 2022

Poster presentation

1. <u>Anna Suzuki</u>, Eisuke Fujita, Masaki Tokurakawa, "Off-peak Raman fiber laser at the wavelength of 1629 nm," The 7th Advanced Lasers and Photon Sources(ALPS), ALPSp-23, Yokohama, Japan, Apr. 2018

Domestic conference

Oral presentation

1. <u>鈴木 杏奈</u>, 戸倉川 正樹, "波長1629 nm ラマンファイバーレーザー励起によるTm:Lu_2O_3レーザーの開発," 第79回応用物理学会秋季学術講演会, 19a-431B-4 名古屋国際会議場, 2018年9月

2. <u>鈴木 杏奈</u>, Christian Kränkel, 戸倉川 正樹, "分散補償鏡を用いたカーレンズモード同期Tm:Sc_2O_3レーザーの開発," 第66回応用物理学会春季学術講演会, 10p-W834-2, 東京工業大学, 2019年3月

3. <u>鈴木 杏奈</u>, Christian Kränkel, 戸倉川 正樹, "共振内スペクトル広帯域化を伴うモード同期Tm:Sc_2O_3 laser レーザー," 第80回応用物理学会秋季学術講演会, 19p-E205-2, 北海道大学, 2019年9月

4. <u>鈴木 杏奈</u>, 戸倉川 正樹, "カーレンズモード同期Tm^{3+}:Lu_2O_3セラミックレーザーの開発," 第67回応用物理学会春季学術講演会, 2020年3月

5. 鈴木 杏奈, Christian Kränkel, 戸倉川 正樹, "Tm添加媒質を用いた複合利得発振器," レーザー学会学術講演会第41回年次大会, オンライン, B05-19p-II-05, 2021年1月

6. 鈴木 杏奈, Christian Kränkel, 戸倉川 正樹, "Tm:RE$_2$O$_3$(RE=Lu, Sc)複合利得媒質を用いたカーレンズモード同期レーザーによるサブ9サイクルパルス発生," 第68回応用物理学会 春季学術講演会, 19a-Z06-2, オンライン, 2021年3月

7. 鈴木 杏奈, Christian Kränkel, 戸倉川 正樹, "Tm添加sesquioxide媒質を用いたカーレンズモード同期レーザー," 第82回応用物理学会秋季学術講演会, 11p-S202-3, オンライン, 2021年9月

8. 鈴木 杏奈, Christian Kränkel, 戸倉川 正樹, "Tm添加sesquioxide媒質を用いたモード同期レーザーの超短パルス化 [invited]," 第69回応用物理学会春季学術講演会, 25a-D215-1, オンライン, 2022年3月

9. 鈴木 杏奈, Sascha Kalusniak, 田中 裕樹, Mario Brützam, Steffen Ganschow, 戸倉川 正樹, Christian Kränkel, "Czochralski法によるTm添加混晶sesquioxide結晶の育成及び特性評価," 第83回応用物理学会秋季学術講演会, 東北大学, 22a-A402-7, 2022年9月

10. 鈴木 杏奈, Sascha Kalusniak, 田中 裕樹, Steffen Ganschow, Christian Kränkel, 戸倉川 正樹, "複合利得媒質および混晶利得媒質を用いた波長2 μm帯レーザーの超短パルス化 [invited]," レーザー学会学術講演会第43回年次大会, ウインクあいち, B10-20p-VI-01, 2023年1月

11. 鈴木 杏奈, Sascha Kalusniak, 田中 裕樹, Steffen Ganschow, Christian Kränkel, 戸倉川 正樹, "Tm添加YScO$_3$結晶の分光及びレーザー特性," 第70回応用物理学会春季学術講演会, 上智大学, 15p-A305-2, 2023年3月

12. 戸倉川 正樹, 鈴木 杏奈, Christian Kränkel, "波長2 μm帯超短パルスTm添加固体レーザーの開発 [invited]," レーザー学会第39回年次大会, 東海大学, 2019年1月

13. 戸倉川 正樹, 鈴木 杏奈, 佐藤 匠, 内園 裕也, 菊地 音, 矢津田 匠海, Christian Kränkel, "波長2μm帯ナノ-フェムト秒パルスTmレーザーの開発 [invited]," レーザー学会第41回年次大会 シンポジウム最新レーザー応用への高度新型レーザー光源, オンライン, 2021年1年

14. 戸倉川 正樹, 鈴木 杏奈, 矢津田 匠海, "波長 2 μm帯短パルスTmレーザ光源の開発と加工応用 [invited]," レーザー加工学会, 2022年5月

Poster presentation

1. 鈴木 杏奈, 戸倉川 正樹 "Tm:Lu$_2$O$_3$レーザー励起用波長1629 nm ラマンファイバーレーザーの開発」第18回レーザー学会東京支部研究会 電気学会 光・量子デバイス技術研究会, 東海大学, 2018年3月

2. 鈴木 杏奈, Christian Kränkel, 戸倉川 正樹, "High Quality factor Tm:Sc$_2$O$_3$カーレンズモード同期レーザーの開発," 第19回レーザー学会東京支部研究会/電気学会 光・量子デバイス技術研究会, P15, 東海大学, 東京, 2019年3月8日

3. 鈴木 杏奈, Christian Kränkel, 戸倉川 正樹," Tm添加複合利得媒質を用いたカーレンズモード同期レーザー," 第5回超高速光エレクトロニクス研究会, 2020年12月

Awards

1. 鈴木 杏奈, 学生優秀発表賞, 第5回超高速光エレクトロニクス研究会, 2020年12月

2. 鈴木 杏奈, 論文発表奨励賞, レーザー学会第41回年次大会, 2021年1月

3. 鈴木 杏奈, 論文奨励賞, 第82回応用物理学会秋季学術講演会, 2021年9月

4. Anna Suzuki, "The Best Student Oral Paper Award", The 11th Advanced Lasers and Photon Sources(ALPS), Yokohama, Japan, Apr. 2022.

Acknowledgement

I would like to acknowledge all members of Tokurakawa laboratory. Thanks to their cheerful and friendly nature, I was able to fully enjoy my lab life. Especially in my PhD, I greatly benefited from numerous discussions with Ryohei Mitsui even late at night.

I would like to express my gratitude to the professors at ILS, as well as the administrative staff.

I would like to express my appreciation to the Japan Society for the Promotion of Science for its financial support.

I am grateful to my parents for allowing me to continue my student life and for their support throughout my whole life.

Lastly, I would like to express my deep gratitude to my husband, Taisuke, for his unwavering support and encouragement all the time.